

NASA/CR—2014-216672



Gravity and Heater Size Effects on Pool Boiling Heat Transfer

Jungho Kim and Rishi Raj
University of Maryland, College Park, Maryland

NASA STI Program . . . in Profile

Since its founding, NASA has been dedicated to the advancement of aeronautics and space science. The NASA Scientific and Technical Information (STI) program plays a key part in helping NASA maintain this important role.

The NASA STI Program operates under the auspices of the Agency Chief Information Officer. It collects, organizes, provides for archiving, and disseminates NASA's STI. The NASA STI program provides access to the NASA Aeronautics and Space Database and its public interface, the NASA Technical Reports Server, thus providing one of the largest collections of aeronautical and space science STI in the world. Results are published in both non-NASA channels and by NASA in the NASA STI Report Series, which includes the following report types:

- **TECHNICAL PUBLICATION.** Reports of completed research or a major significant phase of research that present the results of NASA programs and include extensive data or theoretical analysis. Includes compilations of significant scientific and technical data and information deemed to be of continuing reference value. NASA counterpart of peer-reviewed formal professional papers but has less stringent limitations on manuscript length and extent of graphic presentations.
- **TECHNICAL MEMORANDUM.** Scientific and technical findings that are preliminary or of specialized interest, e.g., quick release reports, working papers, and bibliographies that contain minimal annotation. Does not contain extensive analysis.
- **CONTRACTOR REPORT.** Scientific and technical findings by NASA-sponsored contractors and grantees.

- **CONFERENCE PUBLICATION.** Collected papers from scientific and technical conferences, symposia, seminars, or other meetings sponsored or cosponsored by NASA.
- **SPECIAL PUBLICATION.** Scientific, technical, or historical information from NASA programs, projects, and missions, often concerned with subjects having substantial public interest.
- **TECHNICAL TRANSLATION.** English-language translations of foreign scientific and technical material pertinent to NASA's mission.

Specialized services also include creating custom thesauri, building customized databases, organizing and publishing research results.

For more information about the NASA STI program, see the following:

- Access the NASA STI program home page at <http://www.sti.nasa.gov>
- E-mail your question to help@sti.nasa.gov
- Fax your question to the NASA STI Information Desk at 443-757-5803
- Phone the NASA STI Information Desk at 443-757-5802
- Write to:
STI Information Desk
NASA Center for AeroSpace Information
7115 Standard Drive
Hanover, MD 21076-1320

NASA/CR—2014-216672



Gravity and Heater Size Effects on Pool Boiling Heat Transfer

Jungho Kim and Rishi Raj
University of Maryland, College Park, Maryland

Prepared under Grant NNX11AK25A

National Aeronautics and
Space Administration

Glenn Research Center
Cleveland, Ohio 44135

May 2014

Acknowledgments

This work was supported by the Space Life and Physical Sciences Research and Applications Division in the Human Exploration and Operations Mission Directorate. The authors would also like to thank ZIN Technologies for their support in designing, constructing, and testing the MABE/BXF apparatus. The ISS and Human Health Office at NASA Glenn Research Center in Cleveland, Ohio provided support during operations onboard the International Space Station. The European Space Agency also provided multiple flight opportunities on the Novespace A300 low-g aircraft.

Trade names and trademarks are used in this report for identification only. Their usage does not constitute an official endorsement, either expressed or implied, by the National Aeronautics and Space Administration.

Level of Review: This material has been technically reviewed by NASA technical management OR expert reviewer(s).

Available from

NASA Center for Aerospace Information
7115 Standard Drive
Hanover, MD 21076-1320

National Technical Information Service
5301 Shawnee Road
Alexandria, VA 22312

Available electronically at <http://www.sti.nasa.gov>

Contents

Abstract.....	1
1.0 Introduction	1
1.1 Introduction to Pool Boiling Heat Transfer	2
1.2 Earth Gravity Based Pool Boiling Correlations and Their Extension to Low-g.....	5
1.3 Review of Low Gravity Pool Boiling Research.....	6
2.0 Recent Advances Using Low-g Aircraft	10
2.1 Microheater Array.....	10
2.2 Variable Gravity Experiments and Quasisteady Boiling	10
2.3 Boiling Regimes.....	18
2.4 Gravity Scaling Parameter for the BDB Regime	24
2.5 Gravity Scaling Parameter for SDB Regime	25
2.6 Summary of Ground-Based Work	31
3.0 MABE/BXF Apparatus	33
3.1 MABE Science Heaters	33
3.2 Test Fluid	36
3.3 Boiling Chamber.....	37
3.4 Flow System.....	38
3.5 Cooling Chamber	39
3.6 Embedded Control Circuitry	39
4.0 Test Matrix, Data Acquisition and Reduction, and Uncertainty Analysis	41
4.1 Test Matrix.....	41
4.2 Data Acquisition	41
4.3 Data Reduction.....	42
4.4 Uncertainty Analysis.....	47
5.0 Results of the MABE Experiment on the ISS	53
5.1 Onset of Nucleate Boiling.....	53
5.2 Effect of Subcooling and Pressure	53
5.3 Effect of Gravity and Heater Size	55
5.4 Modified Gravity Scaling Parameter	55
5.5 Comparison with Other Microgravity Heat Transfer Data	57
6.0 Summary and Conclusions	63
References.....	64

List of Tables

Table 1.—Power law coefficient m for gravity during nucleate boiling and CHF	6
Table 2.—Summary of Low-g Experimental Work	9
Table 3.—Test matrix for the variable gravity experiments	12
Table 4.—List of test cases used to validate the scaling parameter for SDB	28
Table 5.—RMS error in prediction using the available correlations	30
Table 6.—Different microgravity environments and the corresponding parameters.....	32
Table 7.—Microheater array parameters	35
Table 8.—Test matrix for Earth gravity experiments	41
Table 9.—Conservative estimate of uncertainties in the value of measured parameters.....	50
Table 10.—Conservative estimate of uncertainties in heat flux at 1g	52
Table 11.—Conservative estimate of uncertainties in heat flux at $10^{-6}g$	52
Table 12.—Thermo-physical properties of CFC-113, pentane and water	59
Table 13.—1g CHF data for spheres (Ref. 63).....	62

List of Figures

Figure 1.—(a) A typical pool boiling curve and (b) schematic representations of heat transfer regimes under Earth gravity conditions (Adapted from: Carey, Liquid-Vapor Phase-Change Phenomena, 1992). 3

Figure 2.—Ebullition cycle as observed under normal Earth gravity conditions. 5

Figure 3.—Schematic representation of boiling under low-g conditions. 5

Figure 4.—Schematic of the trajectory of the parabolic flight with corresponding acceleration levels (ESA’s Zero-G aircraft in the background)..... 11

Figure 5.—Heat flux versus acceleration during transition for a typical case with (a) $\Delta T_w = 9\text{ }^\circ\text{C}$ and (b) $\Delta T_w = 44\text{ }^\circ\text{C}$ 11

Figure 6.—Heat flux versus acceleration during transition along with steady state data for 1g, 1.3g, and 1.6g. 12

Figure 7.—Plot of heat flux versus acceleration for high gas ($c_g \sim 1216\text{ ppm}$) and high subcooling ($\Delta T_{sub} = 26\text{ }^\circ\text{C}$) case, at $\Delta T_w = 44\text{ }^\circ\text{C}$ and $\Delta T_{sub} = 26\text{ }^\circ\text{C}$, with superimposed bottom view images at 0.01g, 0.3g, 0.85g and 1.68g. 13

Figure 8.—Plot of heat flux versus acceleration for the high gas ($c_g \sim 1216\text{ ppm}$) and high subcooling ($\Delta T_{sub} = 26\text{ }^\circ\text{C}$) case for (a) $\Delta T_w = 24\text{ }^\circ\text{C}$, (b) $\Delta T_w = 29\text{ }^\circ\text{C}$, (c) $\Delta T_w = 34\text{ }^\circ\text{C}$, and (d) $\Delta T_w = 39\text{ }^\circ\text{C}$ 14

Figure 9.—Boiling curve at different gravity levels for high gas ($c_g \sim 1216\text{ ppm}$) and high subcooling ($\Delta T_{sub} = 26\text{ }^\circ\text{C}$) with superimposed bottom view images for 1.7g and 0.1g at different temperatures. Solid symbols indicate data in the BDB regime, open symbols indicate data in the SDB regime. 15

Figure 10.—Plot of heat flux versus acceleration for low gas ($c_g \sim 220\text{ ppm}$) and high subcooling case ($\Delta T_{sub} = 26\text{ }^\circ\text{C}$), at $\Delta T_w = 44\text{ }^\circ\text{C}$, with superimposed bottom view images at 0.01g, 0.28g, 0.74g and 1.71g. 16

Figure 11.—Plot of heat flux versus acceleration for the low gas ($c_g \sim 220\text{ ppm}$) and high subcooling case ($\Delta T_{sub} = 26\text{ }^\circ\text{C}$), full heater (96 elements) for (a) $\Delta T_w = 24\text{ }^\circ\text{C}$, (b) $\Delta T_w = 29\text{ }^\circ\text{C}$, (c) $\Delta T_w = 34\text{ }^\circ\text{C}$, and (d) $\Delta T_w = 39\text{ }^\circ\text{C}$ 16

Figure 12.—(a) Boiling curve at three accelerations for low and high gas, (b) heat flux versus acceleration in at $\Delta T_w = 29\text{ }^\circ\text{C}$, for two dissolved gas concentrations, and high subcooling ($\Delta T_{sub} = 26\text{ }^\circ\text{C}$). 17

Figure 13.—A schematic of the bubble size and apparent contact angle for the two gas concentrations in the low-g regime. 18

Figure 14.—Plot of the heat flux versus acceleration at three superheats and subcoolings ($L_h = 7\text{ mm}$), low gas ($c_g < 123\text{ ppm}$). 19

Figure 15.—Boiling curves at different subcoolings and low gas in the BDB (1.0g) and SDB (0.01g) regime. 19

Figure 16.—High gravity boiling curves for three heater sizes with a 2.7 mm microheater array. 21

Figure 17.—Boiling curve for three different heater sizes using n-perfluorohexane, high gas ($c_g \sim 1216\text{ ppm}$) at (a) 1.7g and (b) 1g, (c) 0.3g, and (d) 0.05g. 22

Figure 18.—Boiling curve for different heater sizes using FC-72, $\Delta T_{sub} = 16.6\text{ }^\circ\text{C}$, $P = 1\text{ atm}$, and 2.7 mm microheater array..... 22

Figure 19.—Pool boiling regime map..... 23

Figure 20.—Plot of the power law coefficient m versus T^* in the BDB regime (60 data points, $\text{RMS}_{\text{error}} = 13\text{ percent}$, $11\text{ }^\circ\text{C} \leq \Delta T_{sub} \leq 27\text{ }^\circ\text{C}$, $123\text{ ppm} \leq c_g \leq 1216\text{ ppm}$, and $2.1\text{ mm} \leq L_h \leq 7\text{ mm}$). 25

Figure 21.—Comparison of measured and predicted heat flux values using the gravity scaling parameter for BDB regime (240 data points).	25
Figure 22.—A schematic of heat flux versus acceleration for different subcooling and dissolved gas concentrations.	26
Figure 23.—Comparison between bubble sizes at a gravity level in the BDB regime just before transition (left), and the stable bubble in equilibrium at a gravity level just after transition into the SDB regime (right) for two subcoolings ($L_h = 2.1$ mm, $T_{wall} = 90$ °C).	26
Figure 24.—Plot of the power law coefficient m versus T^* in the SDB regime.....	27
Figure 25.—Comparison of experimental and predicted heat flux value at 0.01g for the high subcooling and low gas cases ($RMS_{error} = 12$ percent).	29
Figure 26.—(a) K_{Jump} at transition versus subcooling, and the (b) comparison of experimental and predicted heat flux values at 0.01g ($RMS_{error} = 20$ percent).	30
Figure 27.—Sensitivity of (a) microgravity acceleration, and (b) low gravity power law coefficient m on heat flux.	31
Figure 28.—BXF mounted in MSG with transparent CV. (Inset: view inside the boiling chamber housing the two microheater arrays.)	34
Figure 29.—Images of the two microheater arrays.....	34
Figure 30.—The MABE feedback circuit.....	36
Figure 31.—A picture BXF hardware with the containment vessel removed.	37
Figure 32.—BXF flow schematic	38
Figure 33.—BXF control system block diagram.	40
Figure 34.—Simplified resistance network model for the major heat transfer paths associated with an element in the microheater array (Δx and Δy are dimension vertical and lateral dimensions respectively).	43
Figure 35.—The schematic of the heat transfer contributions under different gravity conditions.	43
Figure 36.—Heat flux evolution for a single heater (no. 32, top) and 96 heater average (bottom) during a sample Earth gravity experiment (Test no. 2, Run no. 5).....	45
Figure 37.—Natural convection heat flux maps at different stages of data reduction.....	46
Figure 38.—Boiling heat flux maps at different stages of data reduction	47
Figure 39.—Bulk fluid thermistor uncertainty results.	48
Figure 40.—Pressure uncertainty results.	48
Figure 41.—An example of calibration results for eight microheaters in the 2.7 mm array.	49
Figure 42.—Experimental Earth gravity and microgravity pool boiling curves along with the microgravity predictions assuming $m_{SDB} = 0$ (Tests nos. 10, 11, 13, and 14 in Table 8)	54
Figure 43.—Experimental Earth gravity and microgravity pool boiling curves along with the microgravity predictions assuming $m_{SDB} = 0$ (Tests nos. 15, 17, and 18 in Table 8)	55
Figure 44.—Comparison of the experimental data and predicted heat flux values in the SDB regime using (a) Equation (18), and (b) Equation (18) with $m_{SDB} = 0$	56
Figure 45.—Comparison of the numerical simulation (Ref. 60) and the current scaling law in predicting microgravity heat transfer of Qui et al. (Ref. 61).....	58
Figure 46.—Normalized CHF versus acceleration for different fluids and microgravity levels (Refs. 47 and 62)	59
Figure 47.—CHF for finite bodies (a) Lienhard and Dhir (Ref. 45), (b) Ded and Lienhard (Ref. 63), and (c) the current study.....	60

Gravity and Heater Size Effects on Pool Boiling Heat Transfer

Jungho Kim and Rishi Raj
University of Maryland
College Park, Maryland 20742

Abstract

Virtually all data to date regarding parametric effects of gravity on pool boiling have been inferred from experiments performed at discrete gravity levels, namely low gravity ($\sim 0g$), Earth gravity ($1g$), and hypergravity ($>1.5g$) under the assumption that correlations based on measurements in Earth gravity could be extended to other gravity levels. In contrast, the current work is based on observations of boiling heat transfer over a *continuous range* of gravity levels between $0g$ to $1.8g$ and varying heater sizes with a fluorinert as the test liquid (FC-72/n-perfluorohexane). Variable gravity pool boiling heat transfer measurements over a wide range of gravity levels were made during the parabolic flight campaigns organized by NASA and the European Space Agency (ESA) as well as onboard the International Space Station. For large heaters and/or higher gravity conditions, buoyancy dominated boiling and heat transfer results were heater size independent. The power law coefficient for gravity in the heat transfer equation was found to be a function of wall temperature under these conditions. Under low gravity conditions and/or for smaller heaters, surface tension forces dominated and heat transfer results were heater size dependent. A pool boiling regime map differentiating buoyancy and surface tension dominated regimes was developed along with a unified framework that allowed for scaling of pool boiling over a wide range of gravity levels and heater sizes. The prediction errors were significantly smaller than those from correlations currently available in the literature. The scaling laws developed in this study are expected to allow performance quantification of phase change based technologies under variable gravity environments eventually leading to their implementation in space based applications.

1.0 Introduction

Increases in the size and power requirements of space platforms will require increasingly efficient solutions for waste heat rejection to the cold of space. With the exception of heat pipes, spacecraft thermal control has been accomplished through pumped single-phase liquid loop systems. These systems, termed Active Thermal Control Systems (ATCS), have been used on Mercury, Gemini, Apollo, and MIR space station, and are currently used on the Russian Soyuz spacecraft, U.S. Space Shuttle fleet and the International Space Station (ISS). Heat removal is generally performed via a thermal bus, a loop in which a fluid transports heat from the utilities to external radiators. The thermal bus provides a stable thermal environment for a given number of attached modules and to compensate for variations in spacecraft thermal load. Since thermal buses generally pump single phase fluids, the heat removal capability is limited by the relatively small sensible heat capacity of the fluid, resulting in bulky heat rejection units. The size and weight of space-based cold plates can be significantly reduced if the latent heat of the fluid is exploited via boiling to remove large amounts of heat over a relatively narrow temperature ranges. Reductions in flow rates and pumping power may also be possible.

Thermal management (and phase change heat transfer in particular) for advanced life support and propulsion were highlighted as one of the technologies critical for successful deployment of long duration missions by NASA's Workshop on Critical Issues in Microgravity Fluids, Transport, and Reaction Processes in Advanced Human Support Technology, 2004 (Ref. 1):

“Future missions for exploration of the solar system will require enabling technologies for efficient and reliable energy generation, storage and transfer. Integration of several different engineering subsystems and strategies are envisioned. For example, energy generation may be provided by a combination of nuclear, chemical, or solar sources. Energy storage may be accomplished by rechargeable batteries, regenerative fuel cells, flywheels, or latent heat phase change processes, and energy transfer issues might range from large scale, as in cabin thermal control, to small scale, as in space suit temperature regulation. In most of these cases, design of the thermal subsystems becomes an important consideration.

Currently, most of the subsystems involve single-phase fluid and thermal processes; only a small number involve multiphase fluid and thermal processes. But the need for improved energy-to-mass ratios suggests replacing some of the single-phase operations in favor of two-phase systems. Thus, the future design of important thermal subsystems for space applications as in boilers, condensers, evaporators, heat exchangers, normal and cryogenic fluid storage units, fuel cells, radiators, and heat pipes will all involve complex multiphase fluid flow and transport issues.

Fluid flow, heat and mass transfer, and phase separation are all affected by gravity. Unfortunately, there is a scarcity of reliable and pertinent reduced-gravity two-phase flow data. Therefore, a full understanding of both single and multiphase transport phenomena associated with the operation of the thermal and phase change subsystems in microgravity are needed for both the design of the units and their safe and efficient operation in space.”

Based on a critical review of the issues associated with multiphase systems, the report recommended research into the following areas:

- a. Attainment of phenomenological understanding and accumulation of empirical data for boiling in microgravity.
- b. Development of empirical correlations, theoretical models, and scaling laws for boiling process.

Although much research into boiling has been performed over the last 50 years, the mechanisms by which heat is removed from surfaces in low-g environments are still unclear and reliable prediction tools for pool boiling heat transfer are not available. The overall objective of this work is to determine how boiling changes as the gravity and/or heater size are changed. In this report, existing boiling data in low-gravity environments are reviewed and available prediction models are evaluated. Recent advances in variable gravity pool boiling research using a microheater array are discussed. Data taken by the authors over a large range of gravity levels ($10^{-6}g$ to $1.8g$), including results from the Microheater Array Boiling Experiment (MABE) on the International Space Station, are then described and used to develop an understanding of how boiling is altered as the gravity level or heater size changes. A model to predict the effects of gravity and heater size is developed and used to explain some of the contradictory trends in the literature.

1.1 Introduction to Pool Boiling Heat Transfer

Boiling occurs when a liquid is heated to the saturation temperature corresponding to the ambient pressure such that the vapor pressure of the liquid is equal to the ambient/system pressure. *Pool boiling* occurs when the heater is in contact with a pool of liquid with zero bulk velocity, while *flow boiling* occurs when the liquid is under motion. Boiling can also be subdivided into *saturated boiling* (bulk liquid temperature at the saturation temperature) and *subcooled boiling* (bulk liquid temperature below the saturation temperature).

Nukiyama in 1934 (Ref. 2) identified various boiling regimes by electrically heating a horizontal nichrome wire in saturated water and using the current and voltage drop to determine the heat flux and

wire temperature. He presented the results in terms of a *boiling curve*, a plot of heat flux q'' versus wall superheat ΔT_w . A typical boiling curve under Earth gravity conditions is shown on Figure 1(a). When the heat flux is the independent variable (i.e., heat flux controlled heating where temperature T of the wire is the dependent variable), the boiling curve shown by solid arrows (path $a-b-c-d-e-g$) is obtained as the heat flux is increased from point a . If the heat flux is decreased starting from point g , the curve represented by the dashed arrows was observed (path $g-f-c-b-a$). Nukiyama suggested that this hysteresis in the boiling curve would not be observed if the wall temperature was the independent variable. This conjecture was subsequently confirmed by Drew and Muller in 1937 (Ref. 3).

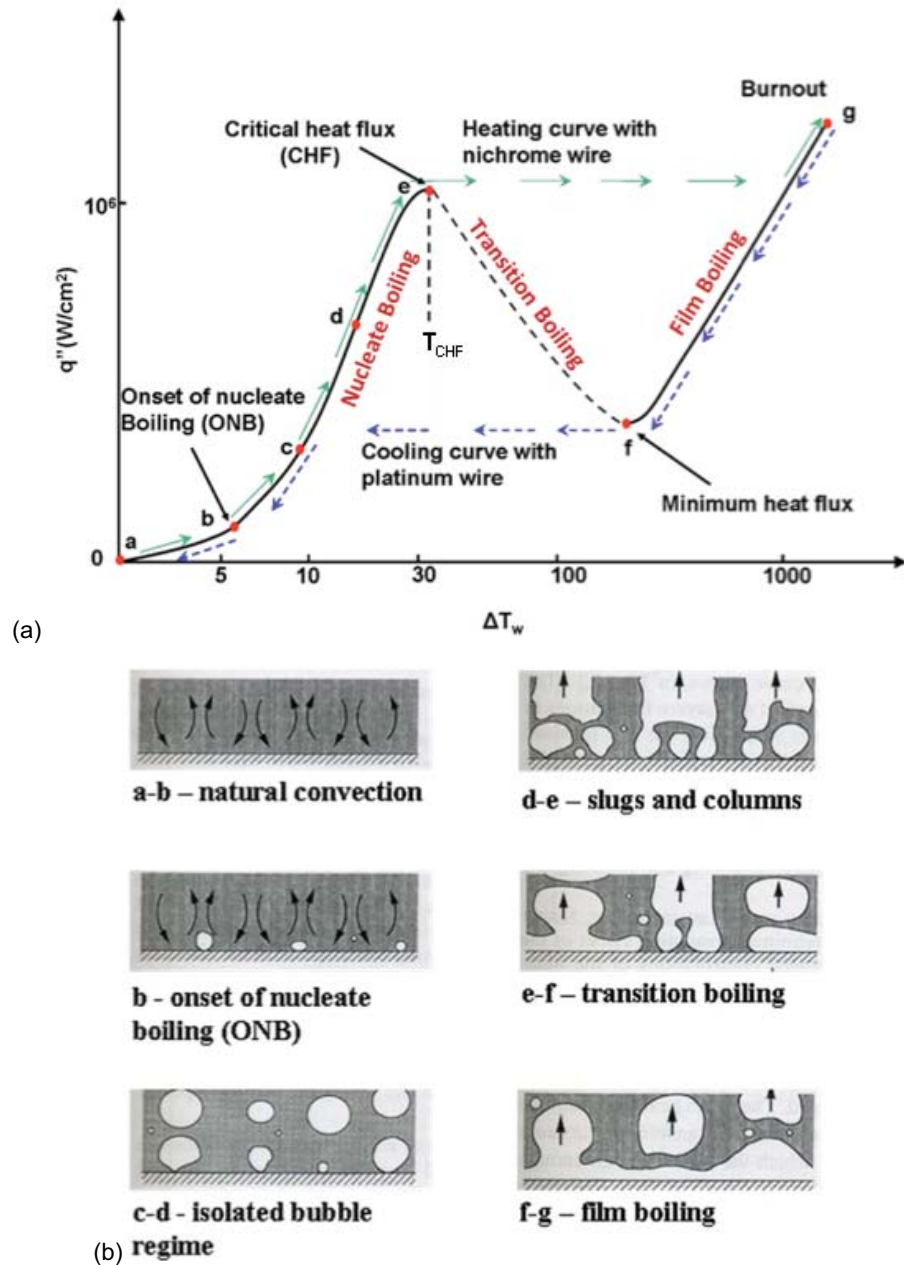


Figure 1.—(a) A typical pool boiling curve and (b) schematic representations of heat transfer regimes under Earth gravity conditions (Adapted from: Carey, Liquid-Vapor Phase-Change Phenomena, 1992).

A schematic representation of the various regimes during pool boiling curve is shown in Figure 1(b). In the natural convection regime (region *a-b*), heat transfer occurs primarily due to buoyancy effects without bubble nucleation. Further increases in the wall temperature initiate the growth of vapor bubbles at preferred nucleation sites and boiling commences (point *b*, Onset of Nucleate Boiling-ONB). Region *b-c-d-e* represents the nucleate boiling regime. Strong disturbance of the superheated liquid near the wall coupled with liquid circulation induced by the motion of the departing vapor bubbles leads to a very steep rise in the heat flux from the heated surface with relatively small increases in the wall temperature. As the heat flux approaches point *e*, bubbles generated at the surface coalesce and the liquid supply to the surface becomes limited. The peak heat flux (point *e*), usually referred to as the Critical Heat Flux (CHF), is the maximum heat flux from the surface that the system can provide in a nonfilm boiling mode at a given pressure. Further increases in heat flux beyond CHF result in transition to the film boiling regime (point *g*). If the wall temperature is the independent variable, the heat flux decreases as the temperature is raised above T_{CHF} and the transition boiling regime is entered. The location of minimum heat flux (point *f*), commonly known as the Leidenfrost point, is characterized by the formation of a stable vapor film between the bulk liquid and the surface. In the film boiling regime (region *f-g*), heat transfer occurs through convection, conduction, and radiation across the vapor film.

Heat is transferred in pool boiling through complicated nonlinear processes operating over a large range of length and time scales. Boiling for large heaters and/or higher gravity conditions is dominated by buoyancy and heat transfer occurs through a combination of natural convection, liquid-vapor phase change, and transient conduction. The ebullition cycle (Figure 2) associated with nucleation, bubble growth, departure and rewetting dominates the contribution to heat transfer. The presence of more than one phase, little understanding of the nucleation process, and a strong dependence on the fluid properties have hindered researchers from developing a completely deterministic model for heat transfer in pool boiling. Many analytical models have been developed that predict boiling behavior, but details of the mechanisms by which heat is removed from the surface and the effect of parameters such as gravity, subcooling, wall superheat, fluid properties, heater surface geometry, and structure are still unclear.

How this ebullition cycle is altered as gravity changes is the focus of this report. Although models developed based on terrestrial data can sometimes yield good estimates of the heat transfer in Earth gravity, they fail to account for boiling behavior across gravitational environments and at smaller length scales since the heat transfer mechanisms associated with buoyancy become less significant and surface tension forces become important as gravity and length scales are reduced. Mechanisms that are unimportant or masked in Earth gravity (e.g., thermocapillary effects) can become significant in the absence of gravity. Examples of surface tension dominated boiling are shown on Figure 3. A large, nondeparting coalesced bubble has been observed to cover the heater (Figure 3(a)) during pool boiling experiments performed in the low-*g* environments produced by parabolic flight ($10^{-2}g$). This coalesced bubble remains attached to the heater with a large dry area and significantly smaller heat transfer. Lee and Merte (Ref. 4) observed a slightly different boiling pattern during the pool boiling experiments on three Space Shuttle flights ($10^{-4}g$) (Figure 3(b)). A large bubble hovered over the heater or remained attached to it depending on the bubble growth rate. This bubble served as a vapor sink for smaller nucleating bubbles generated on the heater allowing liquid to rewet the heater, resulting in high heat transfer. The size of this bubble remained fairly constant, indicating a balance between condensation along the bubble cap and vapor addition by the smaller nucleating bubbles at the base.

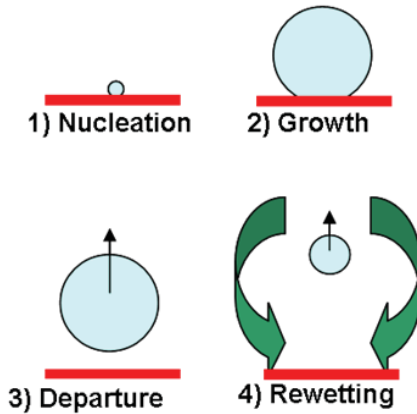


Figure 2.—Ebullition cycle as observed under normal Earth gravity conditions.

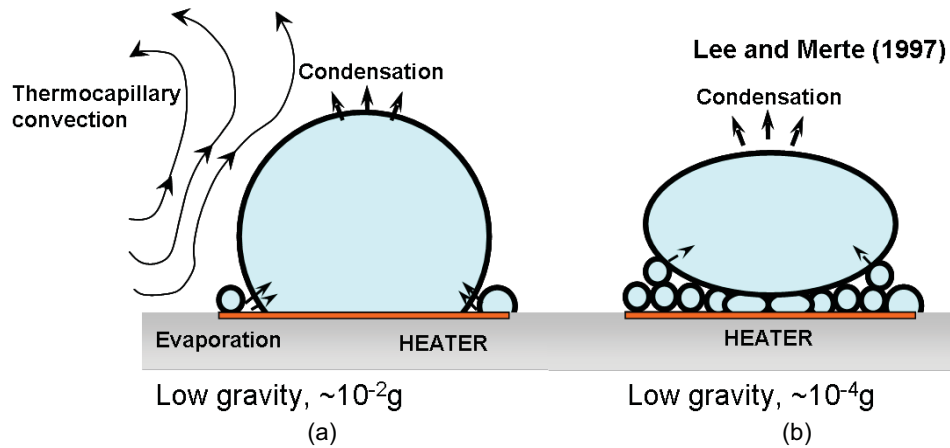


Figure 3.—Schematic representation of boiling under low-g conditions.

1.2 Earth Gravity Based Pool Boiling Correlations and Their Extension to Low-g

Pool boiling correlations in the literature generally include the effects of fluid properties, subcooling, pressure, wall superheat (Eq. (1)). Gravity is included in some correlations, usually in the form of a constant power law coefficient, m (Refs. 5 to 9).

$$q'' = f(c_g, c_p, h_{lv}, p, \alpha, \mu, \rho_l, \rho_v, \sigma, \Delta T_{sub}) * \Delta T_w'' (a/g)^m \quad (1)$$

If all other parameters are held constant, the dependence on gravity can be expressed as:

$$\frac{q''}{q''_g} = \left(\frac{a}{g} \right)^m \quad (2)$$

where the subscript g represents the reference Earth gravity conditions. A summary of some of the more common pool boiling and CHF correlations along with the value of m that accounts for the effect of gravity are summarized in Table 1.

Experiments have shown that commonly used correlations do not properly account for the effect of gravity on the boiling process. For example, the nucleate boiling correlation suggested by Rohsenow (Ref. 5):

$$\frac{q''}{(T_W - T_{sat})^3} C_{sf}^3 = \frac{\mu c_p^3}{h_{fg}^2 Pr^{3r}} \sqrt{\frac{g(\rho_l - \rho_v)}{\sigma}} \quad (3)$$

assumes $m = 0.5$ and predicts that the heat flux goes to zero in the absence of gravity, but the data indicate this to be erroneous. Zhang and Chao (Ref. 10) suggested that the Rohsenow correlation for microgravity may be appropriate if the actual bubble departure diameter was used in place of the Laplace length.

Another commonly used correlation for nucleate pool boiling is given by Cooper (Ref. 6)

$$\frac{h}{\dot{q}^{0.67}} = 55 p_r^{0.12} (-\log_{10} p_r)^{-0.55} M^{-0.5} \quad (4)$$

where p_r = reduced pressure, and M = molecular weight. This correlation does not have any dependence on gravity ($m = 0$), which is also inconsistent with experiments.

Stephan and Abdelsalam (Ref. 7) used regression analysis to obtain correlations for various classes of fluids based on a large body of data, but the data were limited to fully-developed nucleate boiling on horizontal surfaces under the influence of gravity. The role of gravity was accounted for in their correlation through the bubble departure diameter given by

$$D_b = 0.146\theta \left[\frac{2\sigma}{g(\rho_l - \rho_v)} \right]^{0.5} \quad (5)$$

The dependence on g varies (-0.033 to 0.48) depending on which of their correlations is used.

Another commonly used correlation is that of Stephan and Preusser in the VDI Heat Atlas (Ref. 11). The acceleration term appears through the capillarity length, resulting in $m = -0.033$ for a given heat flux. There have also been attempts to correlate microgravity and Earth gravity data (interpolation schemes) to arrive at a power law coefficient m that minimizes the error in the value of heat flux (Refs. 8 and 9).

While a consensus on the value of m in the nucleate boiling regime is absent, there does appear to be widespread agreement that $m = 0.25$ (Table 1) for CHF (Refs. 12 to 16). There is very little data available to verify this, however.

1.3 Review of Low Gravity Pool Boiling Research

Low gravity facilities.—Low-gravity environments are produced by placing the experimental apparatus into a free-fall trajectory where with respect to the apparatus, the weight is balanced by inertia forces. Two aspects to be considered are the residual gravity level which may range from 10^{-2} to 10^{-6} g depending on the platform, and the g-jitter, i.e., the fluctuating oscillations in gravity around the steady state value.

TABLE 1.—POWER LAW COEFFICIENT m FOR GRAVITY DURING NUCLEATE BOILING AND CHF

Nucleate boiling		CHF	
Study	m	Study	m
Rohsenow 1962 (Ref. 5)	0.5	Kutateladze 1948 (Ref. 12)	0.25
Cooper 1984 (Ref. 6)	0	Chang 1957 (Ref. 13)	0.25
Stephan and Abdelsalam 1980 (Ref. 7)	-0.033 to 0.48	Zuber 1959 (Ref. 14)	0.25
Straub 2001 (Ref. 8)	0.13	Kirishenko et al. 1973 (Ref. 15)	0.25
Kannengeiser 2009 (Ref. 9)	0.17	Kandlikar 2001 (Ref. 16)	0.25

Low gravity environments have been produced using drop towers, aircraft, sounding rockets, and through orbiting platforms (satellites, Space Shuttle, and the ISS). Drop towers are the lowest cost method of producing high quality low-g environments for limited duration. Numerous drop towers are available for use throughout the world. The Zero Gravity Research Facility at NASA Glenn Research Center currently provides the longest free fall distance (132 m, 5.18 s) after the closure of the 10 s JAMIC drop-shaft in Hokkaido, Japan. The MGLAB 4.5 s drop tower directed by the Science and Technology Agency in Japan has been available since the mid-1990s. The Bremen Drop Tower in Europe provides 4.76 s of microgravity (10^{-5} g) up to three times per day, but this time can be doubled to 9.3 s through use of a catapult at the bottom of the tower resulting in the longest drop tower test duration.

Aircraft flying parabolic trajectories also provide low-g environments for 20 to 25 s 30 to 40 times per flight, but with a relatively high g-jitter on the order of $\sim 10^{-2}$ g unless the test package is free-floated during the parabola. Low-g aircraft platforms are available for use through Diamond Air Service in Japan (Mitsubishi MU-300), ESA in Europe (Airbus A300), and NASA in the United States (McDonnell Douglas C-9B, Boeing KC-135 and 727).

Sounding rockets are single or two stage launchers fired on a nearly-vertical suborbital trajectory, to apogees up to several hundreds of kilometers. They are mainly dedicated to measurements in Earth science, heliophysics and astrophysics. However, up to 750 s of very high quality microgravity can be obtained with very low g-jitter (residual gravities on the order of 10^{-5} g) during the free-fall part of their trajectory. Active sounding rocket programs in Europe include the MAXUS launcher where almost 15 min microgravity time can be attained with a payload of 800 kg. The TEXUS and MASER carriers provide about 6 min of microgravity for a payload of about 400 kg. A similar program (TR-1A) was operated by JAXA seven times and achieved an apogee of 260 km. Payloads could be as large as 750 kg with four to five experiments supported simultaneously. NASA's sounding rocket program provides many launches per year, with some flights dedicated to microgravity science. In most of these facilities, interaction and control of the experiment is possible via telecommands and real-time video images can be transmitted to/from ground.

Spacelab, the Space Shuttle, and other orbiting satellites have been used to conduct boiling experiments. The International Space Station (ISS) is currently the facility of choice for long-duration, high-quality boiling experiments. This report documents results from the first long duration microgravity boiling experiments performed aboard the ISS.

Previous low-g pool boiling research.—Many of the early experimental studies regarding boiling heat transfer in microgravity environments were performed under NASA sponsorship in drop towers during 1960s. The results of these early experiments were somewhat contradictory, with some experiments showing no effect of gravity on heat transfer and others showing a strong dependence. Much of the discrepancy was attributed to natural convection that occurred before drop initiation and could not be eliminated during the short drop time. Visual observations of the boiling process, however, revealed that a large increase in bubble size (up to a few millimeters) occurred under microgravity conditions, with small bubbles coalescing into larger bubbles a small distance from the heater. Siegel and Keshock (Ref. 17), for example, found the bubble departure radius varied approximately as $a^{-1/3}$ for $0.1 < a/g < 1$, and according to $a^{-1/2}$ for lower gravities.

Straub and coworkers (Refs. 18 and 19) studied at boiling in microgravity environments beginning in the early 1980s. Investigations were carried out using sounding rockets (test times of up to 6 min) under the TEXUS program, and using NASA's KC-135 aircraft (test times of about 25 s per parabolic flight path). Boiling curves from wires and flat plates at saturated and subcooled conditions were obtained for Freon 12, Freon 113, and water. Their results indicated that gravity had little effect on the overall heat transfer from flat plates, i.e., heater temperatures remained constant for given heat fluxes for $\pm 0.03 < a/g < 1.8$, although large increases in the bubble departure radius were observed. Bubble departure was thought to occur as a result of the inertia imparted to the surrounding liquid during bubble growth, which

subsequently pulled the bubble away from the heated surface. The researchers concluded that buoyancy effects were replaced by surface tension effects (coalescence and evaporation-condensation) in microgravity, so the overall level of heat transfer remained about the same. The primary heat transfer mechanism was thought to be evaporation.

Nucleate boiling on a 1.41 mm diameter hemispherical heater and a 0.02 mm diameter wire using Freon 134a was studied by Steinbichler, et al. (Ref. 20) on a Spacelab Mission LMS and a Get Away Special. Their results suggested that stable, saturated boiling was possible on heaters small compared to the container, in contrast to the findings of Ohta et al. (Ref. 21) who found that vapor accumulation near the heater prevented stable, steady-state boiling. They pointed out that, in contrast to other studies, the dynamics of the vapor generated by their small heaters were not restricted by the test cell walls. They attributed the high heat transfer coefficients in microgravity saturated boiling to several factors. First, while the nucleation sites on the hemispherical heater and on the wire were concentrated on the top surface of the heater in Earth gravity, they were evenly distributed over the entire surface in microgravity. Bubble coalescence and turbulence in the fluid aided vapor removal from the surface. At small subcooling, strong thermocapillary flows were observed to hold the bubbles onto the surface that supported the condensation/transport of vapor from the heated surface to the bulk fluid. At high subcooling, rapid growth and collapse of the bubbles on the surface were observed. CHF was observed to decrease with decreasing gravity, but the use of constant heat flux heaters precluded quantitative measurement of critical heat flux levels with accuracy.

Merte also performed many experiments in reduced gravity over the years. Lee and Merte (Ref. 22) describe the results of boiling experiments using R-113 from five space flights between 1992 and 1996. They used a gold film (19- by 38-mm) sputtered on a quartz substrate as both heater and temperature sensor. Boiling behavior for heat fluxes ranging from 2 to 8 W/cm² under saturated and subcooled conditions were obtained. They observed eventual dryout of the surface under high heat fluxes at saturated conditions, but steady nucleate boiling at the same heat flux when the subcooling was increased to 22 °C. When steady nucleate boiling was observed, a very large bubble above the surface acted as a vapor sink for numerous smaller bubbles growing on the heater surface. The large bubble maintained its size due to a balance between condensation along the top of the bubble and coalescence with the smaller bubbles at its base. Heat transfer enhancements of up to 32 percent were observed in microgravity compared to Earth gravity. Marangoni convection was also observed to play a significant role in the enhancement of heat transfer since it caused large vapor bubbles to hover above the heater surface and small bubbles to migrate to the heater surface. Increased subcooling was associated with an increase in heat transfer. CHF appeared to decrease significantly in microgravity.

Ohta, et al. (Ref. 21) measured the heat transfer, local temperature, and local liquid film thickness during boiling of ethanol on a sapphire substrate using a NASDA TR-1A rocket. The local heat transfer was calculated using a numerical simulation of the transient heat conduction within the central 50 mm of the sapphire substrate. Information on the boundary condition was provided by a row of platinum, thin film temperature sensors deposited directly onto the surface of the substrate. At saturated boiling, a very large bubble on the order of the test vessel size formed above the heater surface, and was “lifted” from the surface by numerous smaller “primary” bubbles. The authors did not observe a macrolayer. Boiling never reached a steady state since the “primary” bubbles grew and collapsed at regular intervals. The high heat transfer was attributed to the extending microlayer as the “primary” bubbles grew without a corresponding increase in the dry spot. For highly subcooled boiling, small bubbles on the heater surface were observed. Condensation occurred along the top of the bubbles, and steady state boiling was felt to occur.

Son and Dhir (Ref. 23) documented the behavior of single sliding bubbles on downward facing surfaces at various inclinations. A single artificial cavity formed on a polished silicon wafer was used to generate the bubble. Numerical simulations of the bubble growth and departure were performed at various gravity levels.

Xu and Kawaji (Ref. 24) were perhaps the first to study transition boiling in microgravity. The surface-averaged heat flux and liquid-solid contact frequency were measured with a fast-response, 25.4 mm diameter heat flux gauge built onto a stainless steel plate during a quench with PF-5060. The microgravity environment was obtained using the DC-9 aircraft. They observed that the frequency of liquid rewetting in

microgravity was significantly lower than that in Earth gravity. Vapor film collapse and spreading of the liquid film were thought to be the dominant modes of liquid-solid contact. In Earth gravity, both modes were equally significant, but vapor film collapse became less significant in microgravity resulting in lower contact frequencies. The heat flux was observed to fluctuate by several hundred kW/m² during the quench.

DiMarco and Grassi (Ref. 25) studied boiling on a 0.2 mm diameter wire in microgravity using R113 and FC-72 aboard parabolic aircraft and a sounding rocket. They plotted the enhancement in CHF relative to that of a flat plate versus R' at various gravity levels for their wire, along with the enhancement at similar R' values obtained for extremely small wires in Earth gravity. They found that the microgravity data did not correlate with the Earth gravity data, and suggested that separate groups containing the gravity acceleration and wire diameter were needed.

Experiments to date (Table 2) have shown that boiling can be used to provide substantial heat transfer in microgravity provided vapor is removed from the proximity of the heated surface. Nonetheless, there has been little agreement on the heat transfer mechanisms and its quantification. It is generally agreed that CHF is reduced in low gravity (Figure 4), but the measured CHF values tend to be higher than predicted by the extrapolation of Earth gravity based correlations. The discrepancy between the experimental and predicted values tends to increase with decreasing gravity levels (Figure 4). Significant scatter is present in the low-g pool boiling data, and conventional extrapolation schemes based on a constant power law coefficient m that capture the effect of gravity are not accurate. The scaling of CHF in microgravity based on Bond number/Capillary length has been found to be unsatisfactory, and a separate dependence on gravity and heater size seems to exist. Moreover, extremely little work is available regarding boiling heat transfer or at partial gravity (e.g., Moon, Figure 4) or the high quality microgravity levels (10⁻⁶g) possible at the International Space Station. The lack of work by the microgravity boiling community in this area is puzzling since data over a range of partial gravity levels can provide insight into the boiling behavior in microgravity as the effect of buoyancy is gradually diminished. Extensive experimentation is still required to provide information on the basic mechanisms by which heat is transferred under variable gravity conditions. Additional information regarding worldwide activities regarding boiling in low-g environments is provided in Di Marco (Ref. 26), Kim (Ref. 27), and Ohta (Ref. 28).

TABLE 2.—SUMMARY OF LOW-g EXPERIMENTAL WORK

Reference	Date	ENV	Fluid	Heater	Summary
R. Siegel and Keshock	1961 to 1967	DT	Water	Flat smooth nickel surface 22-mm diam. Nichrome ribbon 3.2- by 22.2-mm	Large bubbles with coalescence
Straub et al.	1986 to 2001	OF DT PF	R12 R11 R123 R113	Wire, 0.2/0.5 mm Pipe, 8 mm O.D. Flat plate 40 by 20-mm (gold coated) Hemispherical heater 0.26 mm diam. Circular heaters, 1/1.5/3 mm diam.	Enhancement at low heat flux, unaffected by subcooling
Merte et al.	1992 to 2002	DT	LH ₂	Flat heater, SiO ₂ , 19 by 38-mm ² 22 mm diam. copper sphere	Thermocapillary convection impels large bubble toward heater, 30 percent enhancement at lower heat flux
Di Marco and Grassi	1999 to 2002	PF SR	R113 FC72	Wire, 0.2 mm diam.	No, appreciable effect on heat transfer coefficient CHF reduced by 50 percent
Abe and Oka	1992 to 1999	PF DT	n-pentane CFC12-CFC112 Water CFC113 CFC11	Glass heater, flat ITO coating 30- by 30 mm ² Artificial cavities	Reduced CHF, observed microlayer, Marangoni effect observed
Ohta et al.	1996 to 2002	PF SR	Water Ethanol	Transparent surface, flat ITO, 50 mm diam. Dh = 50 mm	Enhancement at low heat flux, unaffected by subcooling
Dhir et al.	1999 to 2002	PF	Water	Flat heater, strain gage heater, 45 mm diam.	Bubble departure observed from micromachined nucleation sites

Legend: DT, Drop Tower; OF, Orbital Flight; PF, Parabolic Flight; SR, Sounding Rocket.

2.0 Recent Advances Using Low-g Aircraft

The primary objective of this work is to elucidate the effects of gravity by bridging the gap between experiments conducted at low-g and high-g. Taking the logarithm of Equation (1) yields

$$\log(q'') = m \log\left(\frac{a}{g}\right) + c \quad (6)$$

where $c = \log(f) + n \log(\Delta T_w)$. If the power law dependence is valid, a linear variation in $\log(q'')$ versus $\log(a/g)$ with slope m would be expected for a given fluid at a constant superheat and subcooling as the gravity is changed. Changes in wall superheat and gas concentration should affect the intercept c only and not affect the slope m .

To determine the value of m , an experiment is required where the wall heat flux is measured as the gravity level is changed while keeping constant all of the remaining test parameters (fluid properties, gas concentration, wall surface roughness, bulk liquid subcooling, and wall superheat). The ability of a microheater array to provide a constant wall superheat in the various gravity environments produced by low-g aircraft and the ISS allows this very experiment to be performed. The data obtained from these experiments are presented in this section. These results are used to explain many of the inconsistencies present in the low-g boiling literature, and the model developed also provides a framework within which the MABE data can be evaluated.

2.1 Microheater Array

Microheater arrays consisting of 96 platinum resistance heaters deposited in a 10 by 10 configuration onto a quartz substrate were used to measure the heat transfer distributions. Platinum was used as the heater material due to its stability. The size of the individual heaters in the array were nominally 0.27- by 0.27-mm² or 0.7 by 0.7-mm² in size, resulting in heated areas of 2.7- by 2.7-mm² or 7- by 7-mm². Power was transferred via gold power leads 1 μm thick. The Temperature Coefficient of Resistance (TCR) of the deposited platinum film was measured to be nominally 0.0022 $^{\circ}\text{C}^{-1}$. The heater resistance, and thus the heater temperature, was kept constant using a bank of feedback circuits similar to those used in constant temperature hot-wire anemometry. The power required to maintain these heaters at the desired temperature were obtained by sampling the voltages across the heaters. The frequency response for the heaters and feedback circuits was very high ~ 15 kHz. Further details of the microheater array used in the MABE experiment are provided in Section 3.0.

2.2 Variable Gravity Experiments and Quasisteady Boiling

Test platform.—Variable gravity pool boiling heat transfer data was collected during the 48th (Ref. 29) and 52nd ESA Parabolic Flight Campaigns organized in March 2008 and May 2010, respectively. A typical parabola during microgravity flights along with the acceleration levels is shown on Figure 4. Thirty parabolas were flown per flight, and three flights were made during each campaign.

Parabolic flights were primarily used to study boiling under low-g and hypergravity ($>1.5g$) conditions. However, as can be seen in Figure 4, there is a transition period of approximately 3 to 5 s when the acceleration varies continuously from hypergravity to low-g and vice versa. This period is generally considered too short for a process to reach equilibrium and hence unsuitable for making any measurements. Nonetheless, the relatively fast response of the boiling phenomena coupled with the fast response constant temperature microheater arrays (feedback frequency ~ 15 kHz) used in this study resulted in quasisteady boiling data under many conditions during the short transition periods on the ESA Zero-G aircraft.

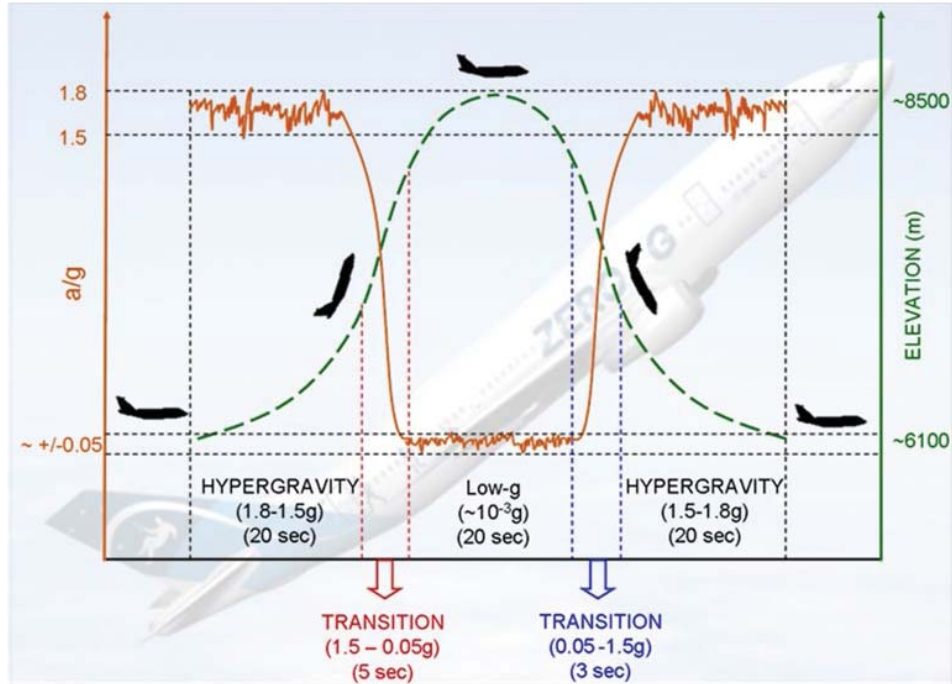


Figure 4.—Schematic of the trajectory of the parabolic flight with corresponding acceleration levels (ESA's Zero-G aircraft in the background).

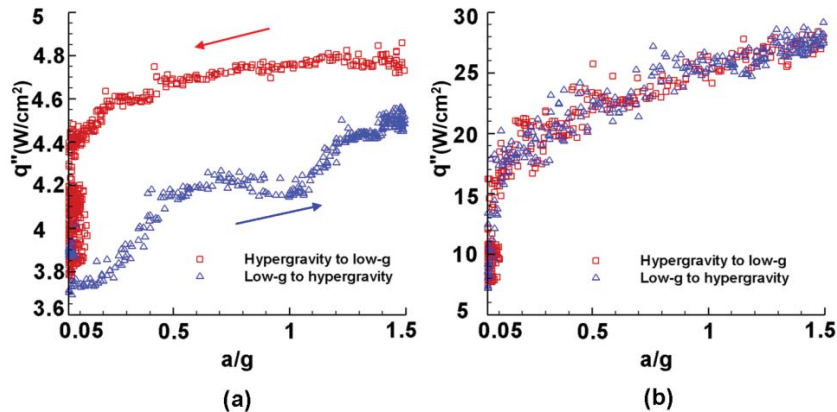


Figure 5.—Heat flux versus acceleration during transition for a typical case with (a) $\Delta T_w = 9 \text{ }^\circ\text{C}$ and (b) $\Delta T_w = 44 \text{ }^\circ\text{C}$.

Quasisteady boiling.—The variation in heat flux q'' versus acceleration during the transition from hypergravity to low-g and vice versa at $\Delta T_w = 9 \text{ }^\circ\text{C}$ and $\Delta T_w = 44 \text{ }^\circ\text{C}$ is shown on Figure 5. If the flow field and heat transfer profiles had sufficient time to achieve steady state at each acceleration level, there should be no difference between the two curves in each graph. However, a hysteresis in the heat flux curve is present at the lower superheat ($\Delta T_w = 9 \text{ }^\circ\text{C}$) (Figure 5(a)). This was observed whenever the superheat was not sufficient to initiate nucleation, and heat transfer was by *natural convection*. As the gravity changed during the natural convection regime, a relatively long time was required for the flow field and heat transfer profiles to develop and achieve steady state. In the high-g period before the transition to low-g, the natural convection flow field was fully developed. During the transition from high-g to low-g, the flow field required more time to achieve steady state than was available, resulting in heat transfer higher than the expected quasisteady value. Similarly, during the transition from low-g to

high-g, the heat transfer was lower than the expected quasisteady value since additional time was needed for the natural convection to develop.

When the wall superheat was raised to $\Delta T_w = 44\text{ }^\circ\text{C}$ (Figure 5(b)), however, the heat transfer was independent of the direction of acceleration. At this temperature, the heat transfer was primarily due to bubble growth and departure. Since bubble departure frequencies could be as high as 30 to 40 Hz at normal gravity and the thermal lag due to the use of a constant temperature heater was negligible (the frequency response of the heater and feedback circuitry was 15 kHz), the boiling heat transfer throughout the transition when boiling occurs was quasisteady.

For each of the data points obtained in low-g, a corresponding steady state Earth gravity experiment was performed under the same test conditions. Additionally, measurements during two steady state hypergravity parabolas (1.3g and 1.6g) at $82.5\text{ }^\circ\text{C}$ (nucleate boiling regime) and different subcoolings ($\Delta T_{sub} = 11, 18$ and $27\text{ }^\circ\text{C}$) were also obtained (Figure 6). Good agreement between these results at 1g, 1.3g and 1.6g and the transition data further confirmed that quasisteady boiling occurred during the relatively quick transition period.¹

Text matrix.—Test conditions for the variable gravity experiments performed during the 48th and 52nd ESA Parabolic Flight Campaign are summarized on Table 3. The experiments were suitably designed such that data sufficient enough to understand the effect of gravity, heater size, subcooling, and dissolved gas concentration on pool boiling heat flux be available.

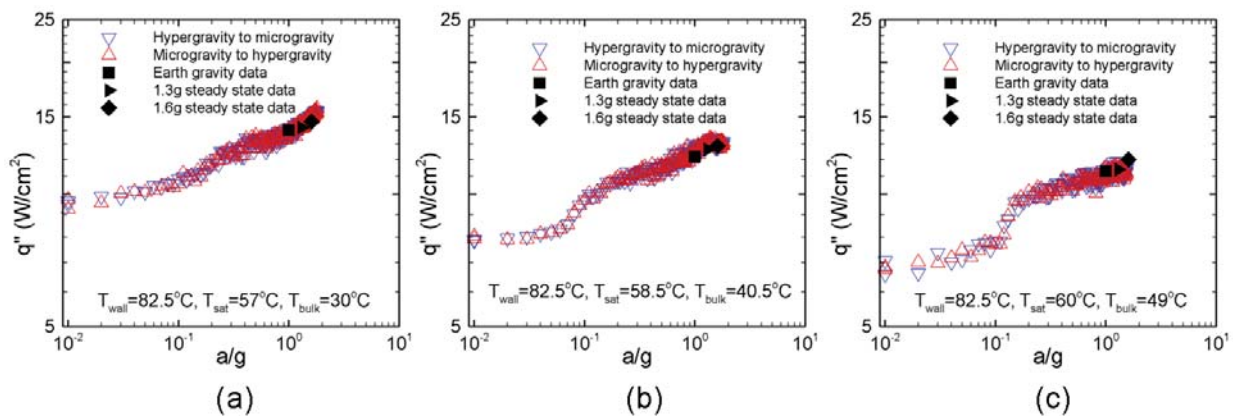


Figure 6.—Heat flux versus acceleration during transition along with steady state data for 1g, 1.3g, and 1.6g.

TABLE 3.—TEST MATRIX FOR THE VARIABLE GRAVITY EXPERIMENTS

ESA campaign no., Fluid	Heater size, mm ²	c_g , ppm	T_w , °C	T_{bulk} , °C	ΔT_{sub} , °C	P , atm
48 th (n-perfluorohexane)	7.0 by 7.0	220 and 1216	65,70,75,80,82.5, 85,87.5,90,95, and 100	30	26	1.0
	7.0 by 3.5			30	26	1.0
	3.5 by 3.5	1216		30	26	1.0
52 nd (Fc-72)	7.0 by 7.0	<123	70, 75, 77.5, 80, 82.5, 85, 87.5, 90, 92.5, and 95	30	27	1.03
			40.5	18	1.08	
	49.5		11	1.13		
	30		27	1.03		
	40.5		18	1.08		
2.1 by 2.1	49.5	11	1.13			

¹ A similar analysis of the data obtained on the various NASA low-g aircraft indicated quasisteady state was never established on this platform due to the shorter transition time between high-g and low-g.

Effect of gravity.—To check the power law dependence assumed in Equations (1) and (2), the boiling heat flux data during one complete parabola was binned based on gravity level into equal intervals of 0.005g. The average heat flux within each bin was assigned to the midpoint acceleration of each bin. Data points corresponding to negative acceleration values (g-jitter) were rejected. An example of the data plotted in log-log coordinates is shown in Figure 7. The squares correspond to the binned data for transition from hypergravity to low-g while the triangles correspond to the data during transition from low-g to hypergravity. A sharp change in heat flux is observed between 0.1g to 0.2g indicating a distinct change in the heat transfer mechanism. *The significance of this observation is that a single power law as per Equation (1) cannot be used to scale the effect of gravity on boiling over the range of gravities tested.* This may explain why previous attempts to correlate boiling data at various gravity levels were not successful. The heat transfer regime that occurs below the transition acceleration will hereafter be referred to as *Surface tension Dominated Boiling (SDB)*, while the regime above this transition will be referred to as *Buoyancy Dominated Boiling (BDB)*.

Comparison of these plots with the video revealed that regular bubble departure occurred in the BDB regime, while a coalesced bubble formed and remained attached to the surface in the SDB regime. The three images on the right (Figure 7, solid arrows at 0.3g, 0.85g, and 1.68g respectively) correspond to departing bubbles in the BDB regime.

The dryout area and the average bubble departure diameter decreased with increasing gravity. Smaller bubble departure diameter corresponded to an increase in departure frequency which, coupled with the decreased dryout area, resulted in an increase in heat transfer with gravity. The image on the left (Figure 7, dashed arrow at 10^{-2} g) is that of a nondeparting coalesced bubble in the SDB regime with large dryout area and lower heat transfer.

Similar qualitative dependence on gravity was observed at other wall superheats as well (Figure 8). The gravity dependence (m) in the BDB regime became stronger with increasing wall superheat and approached a value of $m = 0.25$ near CHF, suggesting that the wall superheat and acceleration effects are not independent as suggested by Equation (1). As will be stressed again below, the parametric effects of gravity and wall superheat are highly interlinked, ruling out the possibility of simple power law correlations with constant m . The dependence of gravity on heat transfer is much smaller in the SDB regime ($0.01 < m < 0.1$, Figure 8).

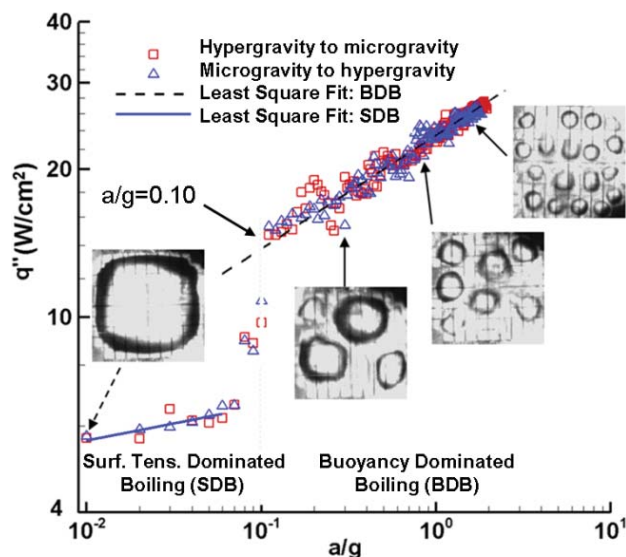


Figure 7.—Plot of heat flux versus acceleration for high gas ($C_g \sim 1216$ ppm) and high subcooling ($\Delta T_{sub} = 26$ °C) case, at $\Delta T_w = 44$ °C and $\Delta T_{sub} = 26$ °C, with

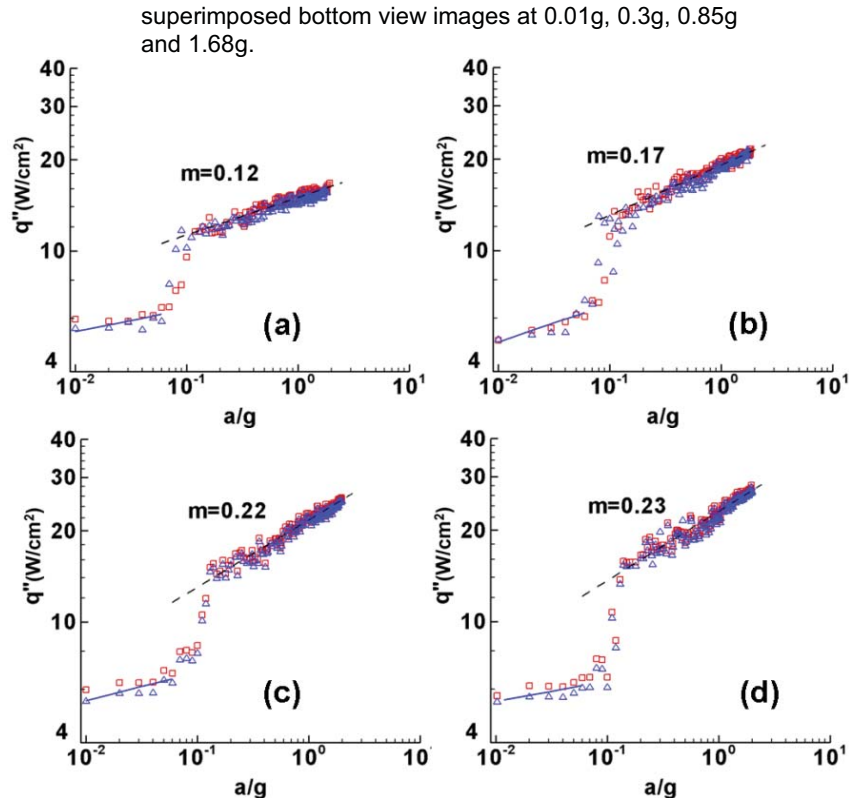


Figure 8.—Plot of heat flux versus acceleration for the high gas ($c_g \sim 1216$ ppm) and high subcooling ($\Delta T_{sub} = 26$ °C) case for (a) $\Delta T_w = 24$ °C, (b) $\Delta T_w = 29$ °C, (c) $\Delta T_w = 34$ °C, and (d) $\Delta T_w = 39$ °C.

Effect of wall superheat.—Boiling curves for the high gas and high subcooling case at a number of gravity levels are shown on Figure 9. For 0.3g, 0.6g, 1g and 1.3g, the data at $\Delta T_w = 9$ °C and $\Delta T_w = 14$ °C were not in quasisteady equilibrium, so this data was not included. In the nucleate boiling regime, the heat transfer continuously increased with wall superheat in the BDB regime. As can be seen from the superimposed bottom view images (solid arrows), most of the heated area experienced natural convection at lower superheats resulting in low heat transfer. With the onset of nucleate boiling, a significant increase in the slope of the boiling curve was observed. Further increases in wall superheat resulted in additional nucleation sites being activated. For a given acceleration level, the bubble departure frequency increased with superheat due to an increase in the bubble growth rate, contributing to the increase in heat transfer.

A sudden decrease in heat transfer is evident as the acceleration decreases from 0.3g to 0.1g due to the transition to the SDB regime (dashed curves, Figure 9)—this corresponds to the formation of a nondeparting coalesced bubble with large dryout area on the heater. The effect of wall superheat is not very clear for the high gas case in the SDB regime. At low wall superheat ($\Delta T_w = 19$ °C, dashed arrow) and 0.1g, a large coalesced bubble with a few satellite bubbles formed, resulting in low heat transfer. At intermediate wall superheats ($\Delta T_w = 29$ °C–31.5 °C) for the same gravity level, more nucleating sites were activated and a coalesced bubble formed amidst numerous satellite bubbles. Lateral movement of the coalesced bubble along the heater array allowed removal of the satellite bubbles through merger with the coalesced bubble, allowing new bubbles to nucleate. For 0.1 g, the heat transfer reached a maximum at $\Delta T_w = 31.5$ °C. At higher superheat ($\Delta T_w = 44$ °C), a large coalesced bubble nearly enveloped the entire heater resulting in lower heat transfer. As the acceleration was decreased to lower levels (0.007g and 0.05g), the heat transfer decreased as well, but the uncertainty in acceleration due to g-jitter became comparable to the acceleration values themselves.

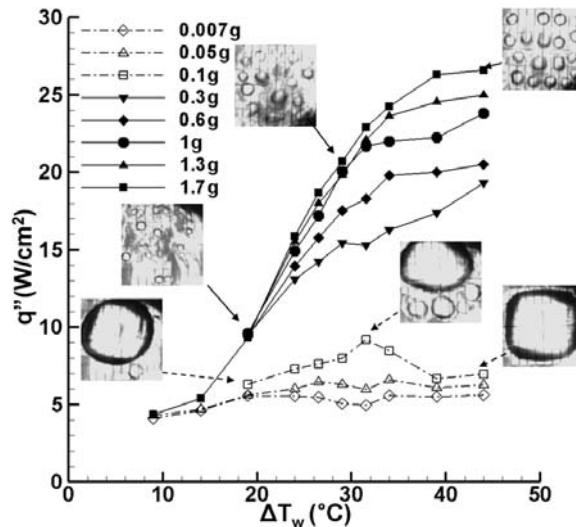


Figure 9.—Boiling curve at different gravity levels for high gas ($c_g \sim 1216$ ppm) and high subcooling ($\Delta T_{sub} = 26$ °C) with superimposed bottom view images for 1.7g and 0.1g at different temperatures. Solid symbols indicate data in the BDB regime, open symbols indicate data in the SDB regime.

Effect of noncondensable gas.—A plot of the heat flux versus acceleration for the low gas and high subcooling case indicated the presence of two regimes (Figure 10 and Figure 11). Similar to the high gas case in the BDB regime (Figure 7 and Figure 8), the bubble departure diameter decreased with acceleration while the departure frequency and nucleate site density increased (Figure 10, solid arrows), resulting in higher heat transfer. Dependence on gravity (m) again increased with wall superheat and approached a value of 0.25 near CHF in the BDB regime (Figure 11). Interestingly, *no jump in heat flux at transition between boiling regimes was observed for the low gas concentration and high subcooling* ($\Delta T_{sub} = 26$ °C). The physical mechanism will be explained in later sections.

Boiling curves for both low and high gas cases at three acceleration levels under high subcooling conditions are shown on Figure 12(a). At low wall superheats, natural convection is the dominant heat transfer mechanism resulting in similar heat transfer coefficients for both gas concentrations. In the BDB regime (1g and 1.7g), the slope of the boiling curves increased significantly after the onset of nucleate boiling. However, as observed by other researchers (Refs. 30 to 32), onset of nucleate boiling for the low gas concentration case (open symbols) occurred at higher superheat since the presence of dissolved gas reduced the vapor pressure required to activate nucleating bubbles. For the accelerations in the BDB regime, nucleate boiling heat transfer was lower for the low gas case than for the high gas case (Figure 12(a) to (b)), consistent with the observations of Rainey et al. (Ref. 31) and Honda et al. (Ref. 32). The presence of gas is thought to promote faster bubble growth and increased bubble departure frequency, resulting in higher heat transfer.

The size of the primary bubble that formed in the SDB regime was smaller for the low gas case than for the high gas case (Figure 12(a)). For boiling in the SDB regime, the influence of gas on heat transfer was opposite of that observed in the BDB regime—heat transfer for the low gas case was higher than for the high gas case (Figure 12(b)). Similar observations based on the experimental work were reported by Henry et al. (Ref. 33), where heat fluxes for the degassed fluid ($c_g < 3$ ppm) were higher than for gas saturated fluid ($c_g \sim 3500$ ppm).

Thermocapillary convection can be a major contributor to the heat transfer *at* lower gravity levels, and results from surface tension gradients along the bubble interface which can form due to temperature gradients:

$$\frac{d\sigma}{dx} = \frac{\Delta\sigma}{\Delta T} \frac{\Delta T}{\Delta x} \quad (7)$$

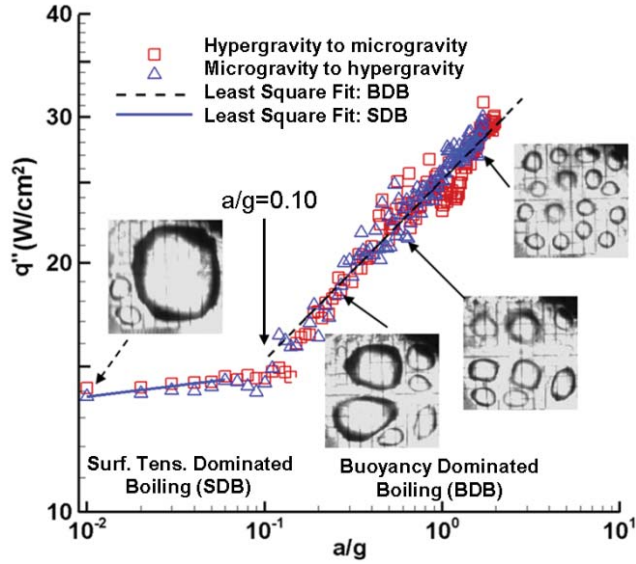


Figure 10.—Plot of heat flux versus acceleration for low gas ($c_g \sim 220$ ppm) and high subcooling case ($\Delta T_{sub} = 26$ °C), at $\Delta T_w = 44$ °C, with superimposed bottom view images at 0.01g, 0.28g, 0.74g and 1.71g.

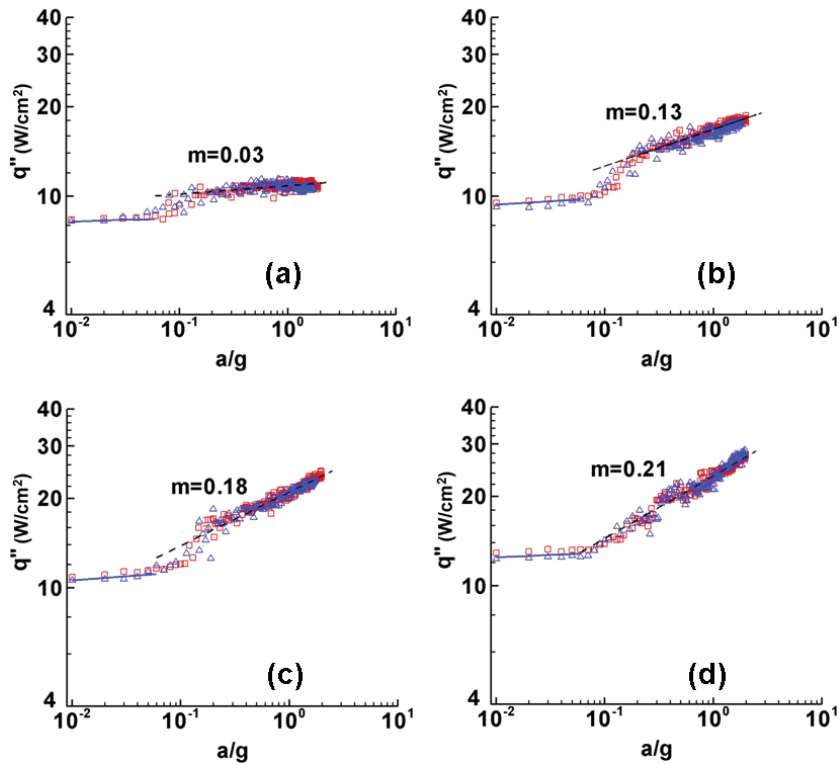
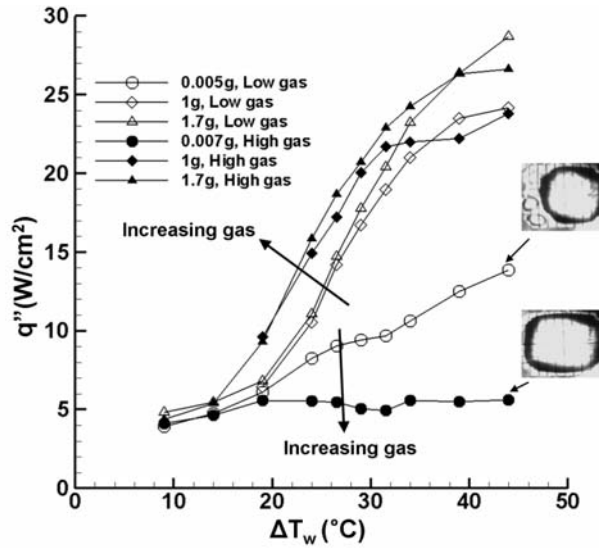
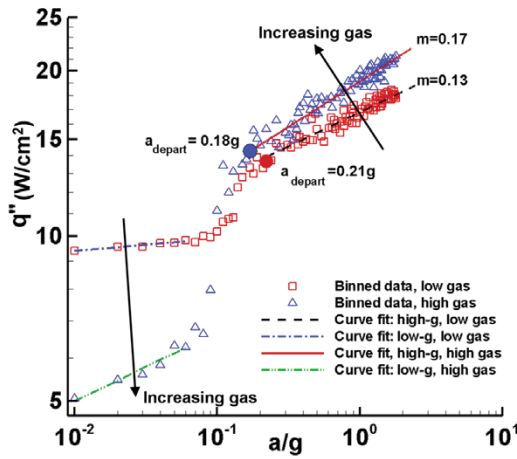


Figure 11.—Plot of heat flux versus acceleration for the low gas ($c_g \sim 220$ ppm) and high subcooling case ($\Delta T_{sub} = 26$ °C), full heater (96 elements) for (a) $\Delta T_w = 24$ °C, (b) $\Delta T_w = 29$ °C, (c) $\Delta T_w = 34$ °C, and (d) $\Delta T_w = 39$ °C.



(a)



(b)

Figure 12.—(a) Boiling curve at three accelerations for low and high gas, (b) heat flux versus acceleration in at $\Delta T_w = 29^\circ\text{C}$, for two dissolved gas concentrations, and high subcooling ($\Delta T_{sub} = 26^\circ\text{C}$).

The first term on the right hand side of Equation (7) is a function of the fluid surface tension while the second term is a function of the available temperature difference along the bubble interface and bubble size. Figure 13 illustrates the differences between the primary bubbles that form at two dissolved gas concentrations. The temperature difference between the heater and the liquid at the top of the bubble is roughly similar for both cases ($\Delta T = T_{wall} - T_{bulk}$). However, due to the smaller bubble diameter ($D_{low} < D_{high}$) and larger contact angle for the low gas concentration ($\theta_{low} > \theta_{high}$), the available length for the surface tension variation was significantly smaller ($\Delta x_{AB} < \Delta x_{CD}$) for the low gas case. The resulting increase in temperature and surface tension gradients along the bubble interface produced stronger thermocapillary flows for the low gas case, which combined with the smaller dryout area, increased the heat transfer. For the high gas case, a larger bubble was formed with a smaller surface tension gradient and a large dryout area resulting in decreased heat transfer in the SDB regime (Figure 12).

Numerical simulations were performed by Raj et al. (Ref. 34) to confirm this behavior and those observed by Henry et al. (Ref. 33). A qualitative study of the effects of dissolved gas content, bubble shape and size, and heat transfer coefficient on the strength of thermocapillary convection was performed

to offer a possible explanation for the existing confusion. Due to the presence of different complex and interrelated mechanisms, the individual mechanisms were decoupled and their overall effect on thermocapillary convection was studied. The results obtained for different bubble radii and contact angles suggested that the strength of thermocapillary convection was determined by the combined effect of the dissolved gas concentration, bubble shape and size, and the variation in evaporation or condensation heat transfer coefficient along the bubble interface. While the increase in dissolved gas concentration helped in the development of the required temperature variation along the bubble interface, the resulting increase in size by orders of magnitude (Figure 13) lowered the temperature gradient and heat transfer across the interface, and ultimately diminished the strength of the thermocapillary convection in the gassy bubble case. The reader is referred to Raj et al. (Ref. 34) for the details of the numerical simulation.

Effects of subcooling.—Results of variable gravity pool boiling experiments at high subcooling and two gas concentrations have been presented thus far. In order to understand the effect of subcooling, additional variable gravity experiments at low and moderate subcooling were undertaken during the 52nd ESA parabolic flight campaign at low dissolved gas concentration (<123 ppm) and three subcoolings. As with the low gas, high subcooling experiments during the 48th campaign, no jump in the heat flux at the transitional acceleration level (a/g) was observed for the high subcooling case while a jump in heat flux at transition was observed for low and moderate subcoolings (Figure 14). Due to this drop in heat flux at this transition, the heat flux in microgravity increased with increasing subcooling (Figure 15). Regardless of the subcooling and dissolved gas concentration levels, however, the acceleration values at transition ($\sim 0.1g$) were similar for all experiments. The power law coefficient m in the BDB regime was observed to increase with superheat and approached a value of 0.25 near CHF. The value of the power law coefficient m in the SDB regime was again small.

2.3 Boiling Regimes

The data presented so far clearly identifies the presence of at least two boiling regimes; the buoyancy dominated boiling (BDB) regime and the surface tension dominated boiling (SDB) regime. Irrespective of the subcooling and dissolved gas concentration levels, transition was observed around $0.1g$ for the 7 mm heater. Above this threshold acceleration, boiling for the 7 mm heater was buoyancy dominated where bubble dynamics similar to Earth gravity boiling were observed. Heat flux and bubble departure frequency increased with acceleration while the bubble departure diameter decreased. Surface tension forces dominated below this threshold acceleration and a large nondeparting coalesced bubble (with occasional departure in some cases) covered the heater. The heat transfer was reduced due to the large dry area and was much less sensitive to gravity. The current section is aimed at understanding the effect of heater size and gravity on the transition between the boiling regimes and the corresponding heat transfer.

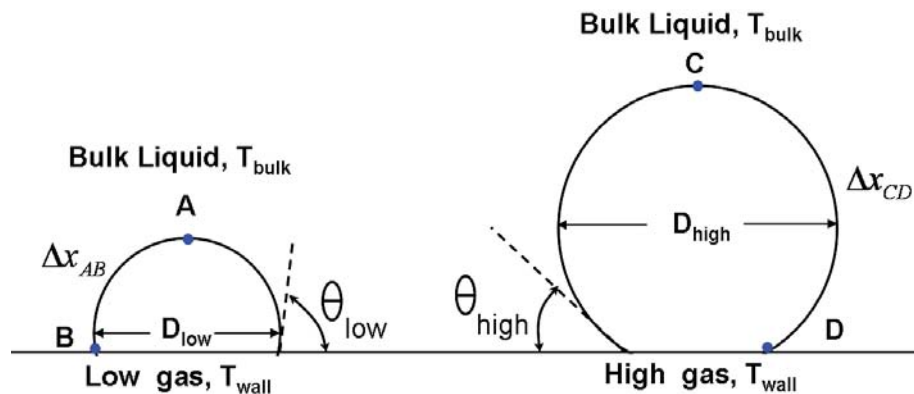


Figure 13.—A schematic of the bubble size and apparent contact angle for the two gas concentrations in the low-g regime.

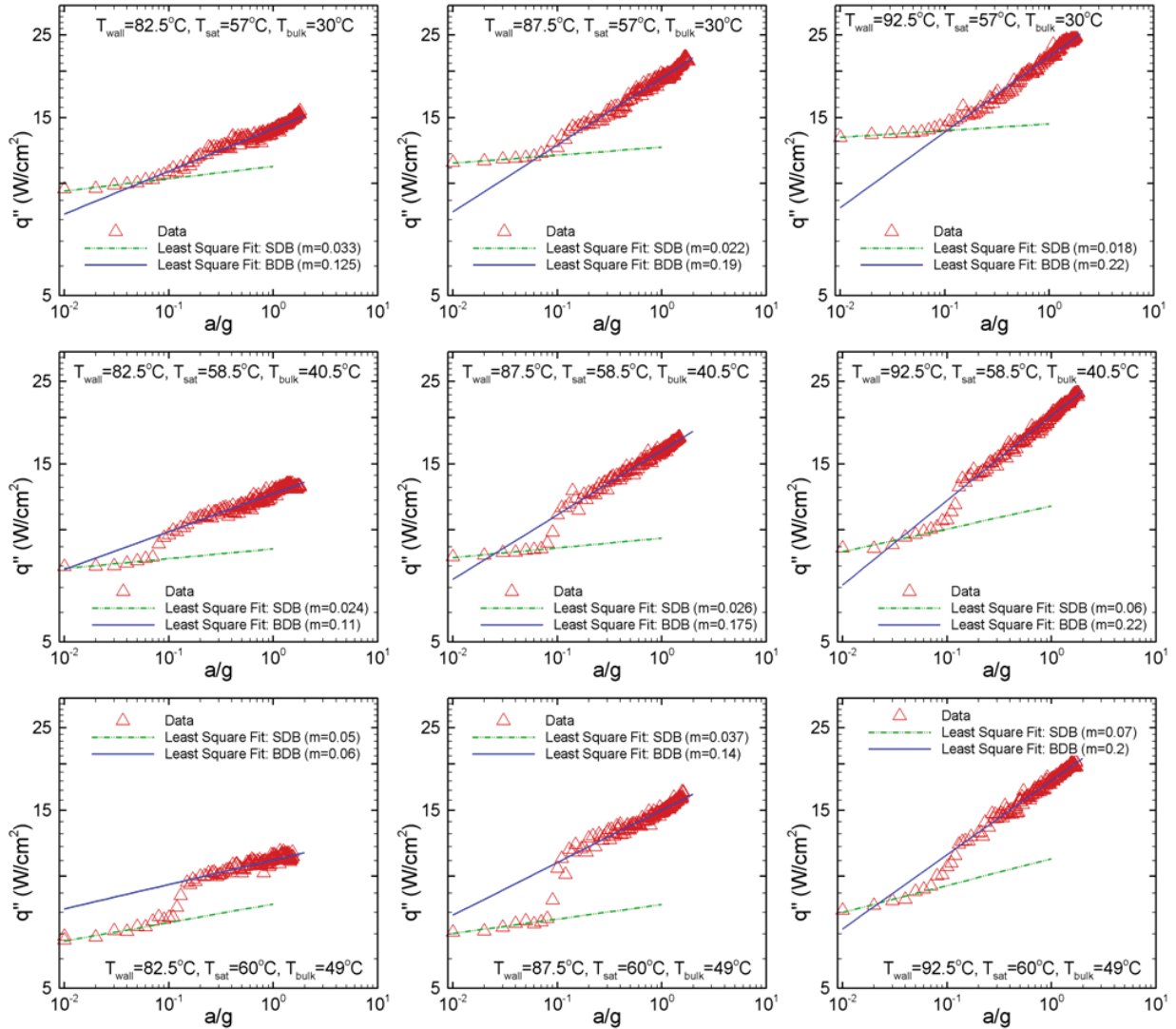


Figure 14.—Plot of the heat flux versus acceleration at three superheats and subcoolings ($L_h = 7$ mm), low gas ($c_g < 123$ ppm).

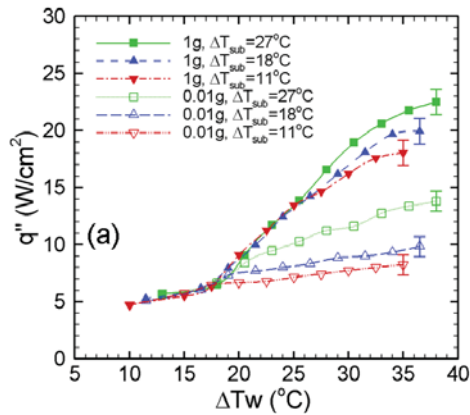


Figure 15.—Boiling curves at different subcoolings and low gas in the BDB (1.0g) and SDB (0.01g) regime.

Boiling on large heaters under Earth gravity conditions is buoyancy dominated and is a combination of natural convection, liquid-vapor phase change, and transient conduction. The ebullition cycle associated with nucleation, bubble growth, departure, and rewetting dominates the heat transfer mechanism. Many semitheoretical models have been developed that predict boiling behavior in Earth gravity. Most of these models assume the heater is of sufficient size such that boiling is independent of heater size. It is generally understood that classical boiling is observed if the heater size is considerably larger than the departure diameter D_d , making it a natural choice of length scale to study heaters size independence. However, estimation of D_d under actual boiling conditions is not straightforward. Although there are correlations for D_d , most of them are only valid for single bubbles and rely on other parameters (e.g., contact angle, departure frequency) which are not easily estimated or measured. The correlations in the literature also result in values for D_d that vary by an order of magnitude or more. For example, Yaddanapuddi and Kim (Ref. 35) compared measured bubble departure diameter and frequency to values obtained from the correlations in the literature, and found errors between -26 to 1400 percent.

On the other hand, capillary length L_c (the ratio of surface tension and buoyancy forces) defined as

$$L_c = \left(\frac{\sigma}{g(\rho_l - \rho_v)} \right)^{1/2} \quad (8)$$

captures the variation of departure diameter, depends only on fluid properties and gravity level, and is easy to estimate. As a result, the ratio of heater size L_h to capillary length L_c is commonly used in the boiling literature (Ref. 36). The quantity $(L_h/L_c)^2$ can also be interpreted as a heater size-based Bond number. Most of the available boiling correlations are valid only if the heater size is considerably larger than the capillary length scale:

$$\frac{L_h}{L_c} \gg 1 \quad (9)$$

Boiling on small heaters under Earth gravity conditions has also been studied extensively (Ref. 37 to 41), and have generally focused on issues such as nucleation, bubble growth rate, and single bubble dynamics. Bakhru and Leinhard (Ref. 42) studied boiling on small diameter wires. They observed that boiling curves for small wires deviate from the classical boiling behavior. Typical boiling behavior from nucleate to film boiling was not observed for $L_h/L_c < 0.15$. Leidenfrost point and critical heat flux (CHF) were also not observed in their study. The heat transfer increased monotonically between first bubble nucleation and full film boiling. It was concluded that the classical boiling curve is only observed if the heater diameter is of the order of $L_h/L_c > 0.15$. They also proposed that similar behavior could be observed for large cylinders at small gravity levels, thus proposing a similarity between heater size and gravity effects.

Henry and Kim (Ref. 41) obtained boiling curves with three heater sizes (0.81- by 0.81-mm², 1.62- by 1.62-mm², and 2.7- by 2.7-mm²) in high gravity environments (~1.7g). As seen on Figure 16, heat fluxes for the two larger sizes were comparable at a given superheat while a smaller heat flux was observed for the smallest size. It was reported that boiling on the 0.81- by 0.81-mm² heated area was surface tension dominated even in hypergravity (1.7g, $L_h/L_c \sim 1.5$), as a stable nondeparting primary bubble similar to boiling in microgravity was formed.

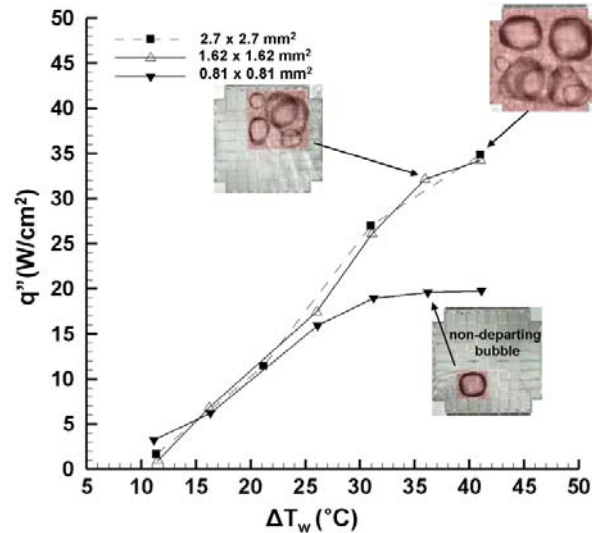


Figure 16.—High gravity boiling curves for three heater sizes with a 2.7 mm microheater array.

An effect of heater size on heat flux is evident from these results. Below a particular heater size (heater width for flat heaters and heater diameter for wires), boiling is surface tension dominated. In this regime, the maximum bubble size becomes comparable to the heater size and a nondeparting primary bubble forms on the heater surface (e.g., 0.81- by 0.81-mm² (Ref. 41)). The heat flux is *heater size dependent* and the boiling curve is specific to that particular heater size in the SDB regime. On the other hand, if the heater size is considerably larger than the capillary length, buoyancy dominated boiling is observed. The bubble size, percentage dryout area, and departure frequency are not influenced by the size of the heater. For any heater size large enough such that boiling is in the BDB regime, the boiling curve is *heater size independent*.

To clarify the relation between gravity and heater size further, variable gravity pool boiling experiments with different heater sizes were performed by changing the number of active heaters within the array. Boiling curves for the three heater sizes at four accelerations are shown on Figure 17. It was observed that the heat flux for three heated areas ranging in size from 7- by 7-mm² to 3.5- by 3.5-mm² (96 heaters to 25 heaters) were similar if the acceleration was 0.3g or larger. In this regime, normal bubble departure was observed (e.g., 0.3g, 1.0g, and 1.7g), boiling was dominated by buoyancy, and the heat transfer was *heater size independent*. However, when the acceleration was smaller than 0.3g, the heat transfer varied significantly with the heater size. As the ratio L_H/L_c decreased due to a decrease in gravity, surface tension forces became increasingly important (0.05g). The sudden drop in heat transfer observed below a particular threshold gravity level was due to the formation of a nondeparting, coalesced bubble and was found to be correlated to the jump in heat flux at transition between boiling regimes as discussed previously.

To identify the threshold heater size for the transition between boiling regimes for heater size independence, further experiments were performed under *Earth gravity* using various fluids and heater sizes to vary L_H/L_c . Data was also obtained at elevated pressures (1.86 atm) and a subcooling of 26 °C with the 2.7 mm microheater array. The reader is referred to Raj and Kim (Ref. 43) for further details. As an example of the results, the data for FC-72 indicated that boiling was buoyancy dominated for heaters larger than 1.62 mm (36 heaters) and heat transfer was independent of heater size (Figure 18). For heaters smaller than 1.62 mm, boiling was surface tension dominated and heat transfer was a function of heater size. Bubble departure frequency was either significantly reduced or a nondeparting coalesced bubble formed, significantly reducing the heat transfer.

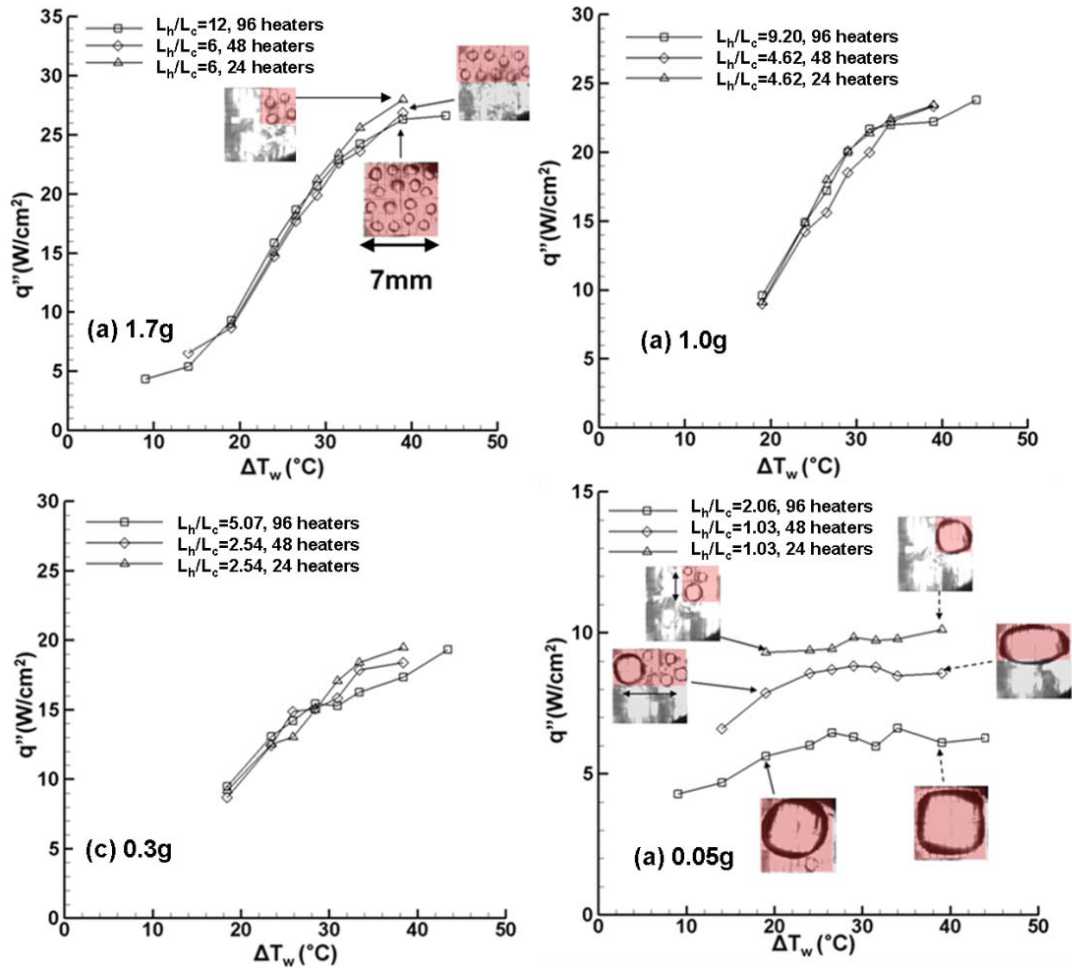


Figure 17.—Boiling curve for three different heater sizes using n-perfluorohexane, high gas ($c_g \sim 1216$ ppm) at (a) 1.7g and (b) 1g, (c) 0.3g, and (d) 0.05g.

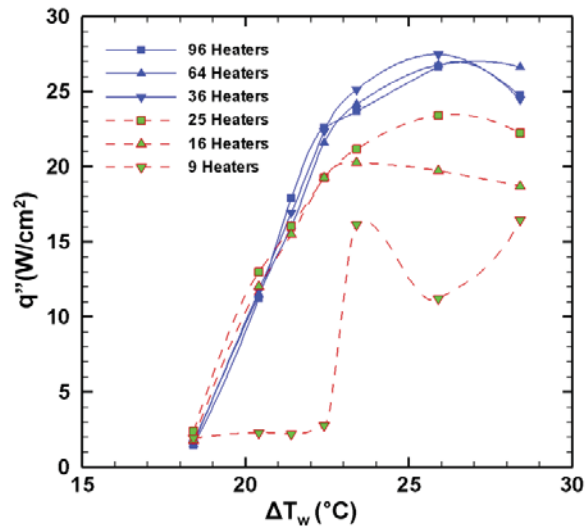


Figure 18.—Boiling curve for different heater sizes using FC-72, $\Delta T_{sub} = 16.6^\circ\text{C}$, $P = 1$ atm, and 2.7 mm microheater array.

These Earth gravity results with variable heater size were correlated with the variable gravity results to obtain a transition criteria based on the heater size and gravity (Ref. 44). The nondimensional length L_H/L_c incorporates the effects of gravity and heater size and differentiates between the boiling regimes. Pool boiling was buoyancy dominated for $L_H/L_c > 2.1$ and surface tension dominated below this value. Lienhard and Dhir (Ref. 45) reported similar observations for CHF during pool boiling experiments on cylinders. They performed Earth and hypergravity experiments with heaters of different diameters such that L_d/L_c (where L_d is the diameter of a cylindrical heater) varied from 0.2 to 20. It was concluded that the CHF follows the classical $g^{1/4}$ power law as proposed by Zuber (Ref. 14) for $L_d/L_c > 2.2$, while a decrease in gravity dependence was observed at CHF for $L_d/L_c < 2.2$. Regardless of the heater size, subcooling, and dissolved gas concentration levels, the acceleration values at transition were very close to the predicted values based on the transition criteria ($L_H/L_c = 2.1$) reported above (Ref. 43):

$$a_{tran} = \frac{4.41\sigma}{L_H^2(\rho_l - \rho_v)} \quad (10)$$

This transition criteria can also be expressed in dimensionless terms as follows:

$$Bo_{tran} = 4.41 = \frac{a_{tran}(\rho_l - \rho_v)L_H^2}{\sigma} \quad (11)$$

A summary of all the experimental data is shown on Figure 19. The nondimensionalized acceleration a/g and the ratio of the heater size to capillary length L_H/L_c are used as the two axes. A line at $L_H/L_c = 2.1$ divides the pool boiling into a heater size independent/BDB regime and a heater size dependent/SDB regime. Data in the surface tension dominated boiling regime (solid symbols) and are dependent on the heater size lie below the line $L_H/L_c = 2.1$, while the data in the buoyancy dominated regime (open symbols) and are heater size independent lie above the line $L_H/L_c = 2.1$. This transition criterion is not a function of the gravity level and holds for the two fluids (pentane and FC-72) investigated. These results at elevated pressures and various subcoolings along with those presented previously at different gas concentrations confirmed the validity of the transition criteria over a wide range of experimental conditions.

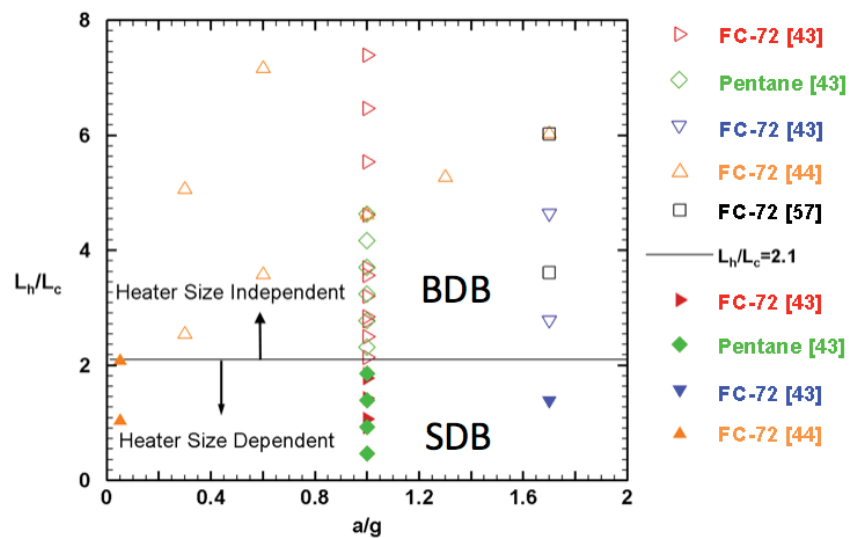


Figure 19.—Pool boiling regime map.

Based on these observations, the terms “small heater” and/or “low-gravity” are not completely descriptive of the boiling conditions. These terms “are better expressed as “surface tension dominated boiling” (SDB) where phenomena was “heater size dependent”. Similarly, the term “buoyancy dominated boiling” (BDB) better expressed boiling for “high gravity” conditions and/or “large heaters” where the phenomena was “heater size independent.”

2.4 Gravity Scaling Parameter for the BDB Regime

The variable gravity pool boiling data acquired during the 48th and 52nd ESA parabolic flight campaign were used to develop a scaling parameter for the BDB regime. As discussed previously, the use of a single value of m to scale for gravity effects is incorrect. This is supported by other studies as well. For example, Oka et al. (Refs. 46 and 47) reported that the deterioration in heat flux was insignificant ($m \sim 0$) due to gravity in the low heat flux region that is characterized by isolated bubbles (analogous to test conditions of low wall superheat for constant temperature heaters for the current work). On the other hand, a 30 to 40 percent decrease as predicted by the conventional one-fourth power law ($m = 0.25$) was reported at CHF.

A plot of m in the BDB regime (m_{BDB}) for all the data available (various subcoolings, heater size, and gas concentrations) to date are summarized in Figure 20. Although the power law coefficient versus superheat/temperature curve depended on gas concentration and wall temperature, they collapsed onto a single curve when plotted using a nondimensional temperature (T^*) defined as (Ref. 48):

$$T^* = \frac{T_w - T_{ONB}}{T_{CHF} - T_{ONB}} \quad (12)$$

Using this nondimensional temperature accounted for shifts in ONB due to dissolved gas concentration or nucleation site densities on the power law coefficient m . The effect of subcooling on m was also not significant. An expression for m that best fit the data with minimal error is given by:

$$m_{BDB} = \frac{0.65T^*}{(1 + 1.6T^*)} \quad (13)$$

Although the RMS error between the predicted m based on (Eq. (13)) and the experimental values is 13 percent, the uncertainty in m had little effect on q'' due to its small value. Based on the variation of m defined by Equation (13), the heat flux at two gravity levels (a_{ref} and a) in the BDB regime can be related as follow:

$$\frac{q''_a}{q''_{a_{ref}}} = \left(\frac{a}{a_{ref}} \right)^{\frac{0.65T^*}{(1+1.6T^*)}} \quad \text{for } L_h / L_c \geq 2.1 \quad (14)$$

Given the heat flux at a reference acceleration a_{ref} in the BDB regime, the heat flux at any other acceleration (a) in the BDB regime can thus be predicted if the superheat at ONB and CHF are known at the reference acceleration.

A summary of the experimental versus predicted results for all the test conditions (Table 3) are shown on Figure 21. Earth gravity data was used as the reference value to obtain predictions at four gravity levels in the BDB regime (0.3g, 0.6g, 1.3g, and 1.7g). The data in this plot includes the effects of wall temperature, heater size, bulk liquid subcooling, dissolved gas concentration, and heater surface morphology. These results clearly rule out the use of a constant m to account for gravity and highlight the need to use a temperature dependent m (Eq. (13)) to describe gravity effects in the BDB regime.

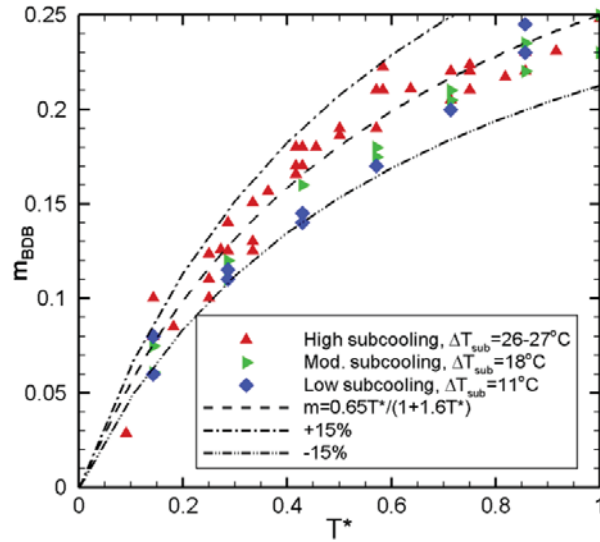


Figure 20.—Plot of the power law coefficient m versus T^* in the BDB regime (60 data points, $\text{RMS}_{\text{error}} = 13$ percent, $11\text{ }^\circ\text{C} \leq \Delta T_{\text{sub}} \leq 27\text{ }^\circ\text{C}$, $123\text{ ppm} \leq c_g \leq 1216\text{ ppm}$, and $2.1\text{ mm} \leq L_h \leq 7\text{ mm}$).

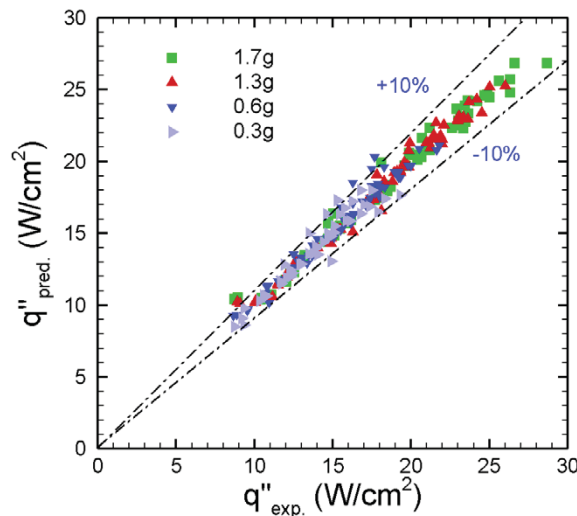


Figure 21.—Comparison of measured and predicted heat flux values using the gravity scaling parameter for BDB regime (240 data points).

2.5 Gravity Scaling Parameter for SDB Regime

While the dependence of heat flux on acceleration (Eq. (13)) in the BDB regime and the acceleration at which transition to the SDB regime occurs (Eq. (10)) are understood, the prediction of heat flux in the SDB regime is complicated by a change in slope and occasional jump in heat flux at transition. A schematic describing the dependence of heat flux on acceleration is shown on Figure 22. For all experiments with *low gas and high subcooling*, no jump in heat flux was observed at transition (Figure 22(a)). For the other three combinations of subcooling and dissolved gas concentrations (i.e., low gas and low subcooling, high gas and low subcooling, and high gas and high subcooling), a jump in heat flux at transition was observed (Figure 22(b)).

The occurrence of a jump in heat flux as the subcooling decreases can be explained using the visualization data. First, consider the low subcooling, low dissolved gas cases: In the BDB regime, the heat transfer at the base of the bubble is balanced by condensation through the bubble cap and by the departure of the bubble itself (i.e., $q_2 = \bar{q}_{e2} = \bar{q}_{c2} + q_{\text{depart}}$, where the macron indicates time average over one bubble cycle), limiting the size of the bubble that forms on the heater (Figure 23(a)). As the gravity level is reduced and transition to the SDB regime occurs, a nondeparting bubble forms on the heater. The heat transfer through the bubble base must now be balanced solely by condensation through the bubble cap since no departing bubbles are available to carry away the heat. The size of the bubble (and therefore the dry area) increases (Figure 23(b)) to a point where evaporation and condensation are in balance

($q_{2'} = \bar{q}_{e2'} = \bar{q}_{c2'}$), resulting in a drop in heat transfer ($\Delta q'' = \frac{q_2 - q_{2'}}{L_h^2}$) as shown on Figure 22(b). For the

high subcooling case, however, the condensation through the bubble cap is not limited by a small temperature difference, thus bubble size and the corresponding heat transfer are not required to change as transition occurs (Figure 23(c) and (d)).

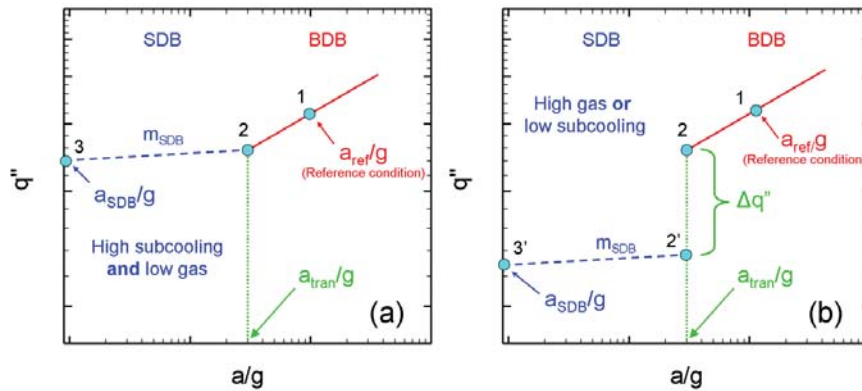


Figure 22.—A schematic of heat flux versus acceleration for different subcooling and dissolved gas concentrations.

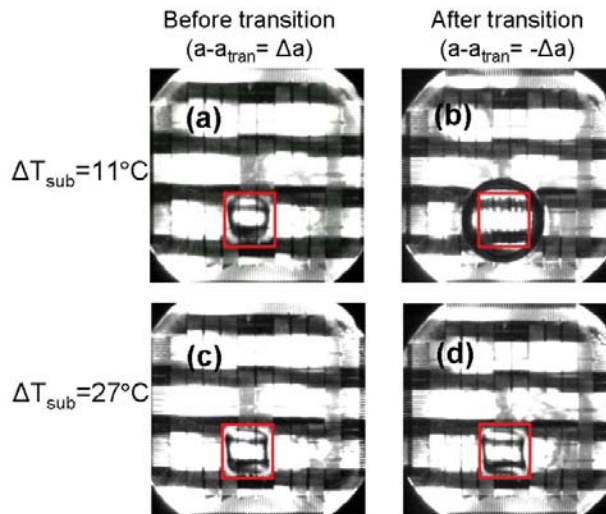


Figure 23.—Comparison between bubble sizes at a gravity level in the BDB regime just before transition (left), and the stable bubble in equilibrium at a gravity level just after transition into the SDB regime (right) for two subcoolings ($L_h = 2.1 \text{ mm}$, $T_{\text{wall}} = 90 \text{ }^\circ\text{C}$).

A similar argument can be used to explain the jump in heat flux that forms as the dissolved gas concentration increases. For boiling with significant dissolved gas concentration, the rate of condensation through the bubble cap is limited by diffusion of vapor through the accumulated gas within the bubble. As a result, the bubble must grow in size once transition to the SDB regime occurs. An increase in bubble size increases the dry area on the heater, decreasing the evaporation heat transfer until it is balanced by condensation. This decrease in heat flux at transition is reflected as a drop in heat flux for high gas concentration cases ($\Delta q''$ in Figure 22(b)).

A step-by-step procedure to quantify the magnitude of the jump and develop scaling laws for the SDB regime is now discussed. Cases with no jump are first considered followed by modeling of the jump due to subcooling and dissolved gas in turn.

High Subcooling with Low Dissolved Gas Cases.—First, consider the cases with high subcooling and low dissolved gas concentration where no jump occurs (Figure 22(a)). In order to scale the heat flux from a reference high gravity condition (point 1 in Figure 22(a)) to a surface tension dominated boiling condition (point 3 in Figure 22(a)), knowledge of transition acceleration and scaling laws from point 1 to 2 and from point 2 to 3 are required. The transition acceleration can be calculated from Equation (10), and the gravity scaling parameter for the BDB regime (Eq. (14)) discussed in the previous section can be used to scale the heat flux from points 1 and 2. Scaling from points 2 and 3 requires a model for the power law coefficient in the SDB regime m_{SDB} .

A plot of m_{SDB} for all data points available is shown in Figure 24. Unlike the BDB regime, a model for m_{SDB} was characterized by the lack of any distinct trend in the data. The scatter in the data may be due to the relatively large g-jitter on the aircraft ($\sim 10^{-2}g$). The much smaller gravity dependence in the SDB regime, however, allowed the selection of a constant value for m_{SDB} . Based on Equations (10), (13), and (14), the scaling factor from points 1 to 3 for the low gas and high subcooling case is represented by Equation (15).

$$q''_{SDB} = q''_{ref} \left(\frac{a_{tran}}{a_{ref}} \right)^{\frac{0.65T^*}{(1+1.6T^*)}} \left(\frac{a_{SDB}}{a_{tran}} \right)^{m_{SDB}} \quad (15)$$

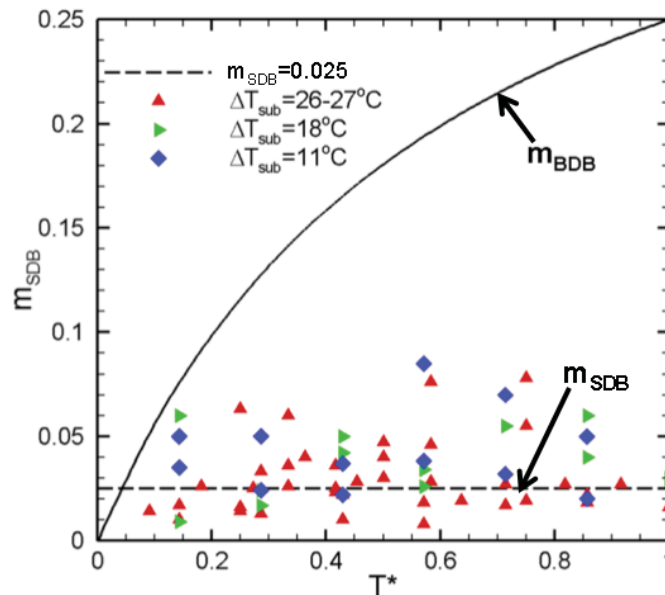


Figure 24.—Plot of the power law coefficient m versus T^* in the SDB regime.

The second term on the right hand side is the gravity scaling parameter (points 1-2) for BDB (Eq. (14)) with the numerator being the acceleration at transition (a_{tran} , point 2). The third term is the scaling parameter in the SDB regime. As seen from this equation, given the heat flux at a reference acceleration a_{ref} (1), the heat flux in the SDB regime (q_{SDB} , 3) can be predicted if the superheat at ONB and CHF are known at the reference condition, i.e., given a pool boiling curve in Earth gravity or any other reference gravity condition in the BDB regime, pool boiling curves under similar experimental conditions in the SDB regime can be generated.














The list of studies used to validate the scaling parameter for SDB is summarized in Table 4. Cases where the coalesced bubble was much larger than the active heater size in the SDB regime (2.1- by 2.1-mm², $\Delta T_{sub} = 18$ and 11 °C) were not included since the heater was completely dry and the heat transfer was artificially low in these cases. These cases were not representative of heater size and will not be included in further discussions concerning the effect of heater size. The value of m_{SDB} that minimized the error was found to be 0.025. The results of the prediction for the high subcooling and low gas test cases (nos. 5, 7, 10, and 11)² are shown at $a/g = 0.01$ (representative of the acceleration in the aircraft low-g environment) in Figure 25. The overall agreement between the predicted and experimental results is good and the RMS error, defined as

$$RMS_{error} = \sqrt{\frac{\sum_{i=1}^n \left(\frac{q_{exp,i}'' - q_{pred,i}''}{q_{exp,i}''} \right)^2}{n}} \times 100 \quad (16)$$

is within 12 percent. The scaling for the high subcooling, low gas cases can be written as:

$$q_{SDB}'' = q_{ref}'' \left[\frac{4.41\sigma}{L_h^2(\rho_l - \rho_v)a_{ref}} \right]^{(1+1.6T^*)} \left[\frac{L_h^2(\rho_l - \rho_v)a_{SDB}}{4.41\sigma} \right]^{0.025} \quad (17)$$

TABLE 4.—LIST OF TEST CASES USED TO VALIDATE THE SCALING PARAMETER FOR SDB

Study	Case no.	Symbol	L_h , mm	ΔT_{sub} , °C	C_g , ppm
Kim, Benton, and Wisniewski (2002) (Ref. 40)	1		2.7	32.6	<1500
	2		2.7	25.4	<1500
	3		2.7	20	<1500
	4		2.7	7	<1500
Henry, Kim, and McQuillen (2006) (Ref. 33)	5		7	28	<3
	6		7	28	3500
Raj, Kim, and McQuillen (2009) (Ref. 44)	7		7	26	220
	8		7	26	1216
	9		3.5	26	1216
Raj, Kim, and McQuillen (2012) (Ref. 48)	10		7	27	<123
	11		2.1	27	<123
	12		7	18	<123
	13		7	11	<123

² The logic behind selecting these four test runs as high subcooling and low gas and the quantification of subcooling and gas concentration levels will become clear in later section.

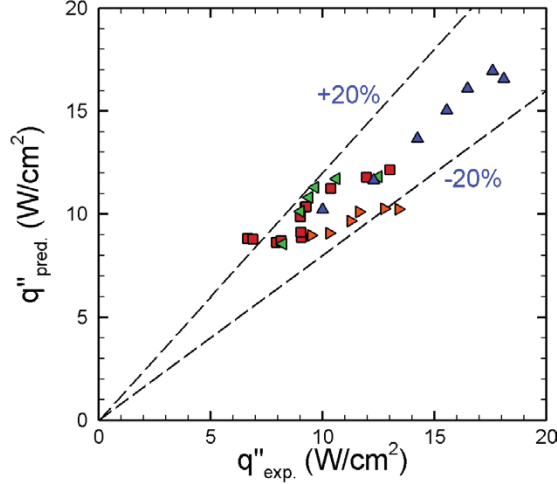


Figure 25.—Comparison of experimental and predicted heat flux value at 0.01g for the high subcooling and low gas cases ($RMS_{error} = 12$ percent).

Effect of subcooling with low dissolved gas concentrations.—The more complicated case of a jump in heat flux ($\Delta q''$) due to subcooling and dissolved gas (Figure 22(b)) is considered next. For the sake of simplicity, a sharp jump in heat flux is assumed to occur at the transition acceleration throughout this study ($a_2 = a_{2'} = a_{tran}$). In order to account for the dissolved gas effect described above, subcooling is based on the saturation pressure of the partial vapor pressure when modeling the jump. Referring to Figure 22(b), scaling laws from 1–2, 2–2', and 2'–3' are required. The scaling of heat flux from 1–2 and from 2'–3' are same as the previous case with high subcooling and low gas. However, a parameter to scale the jump in heat flux from 2–2' is required as follows $K_{Jump} = q_2'/q_2$, $\Delta q'' = (q_2 - q_2')/L_h^2$:

$$q''_{SDB} = q''_{ref} \left[\frac{4.41\sigma}{L_h^2(\rho_l - \rho_v)a_{ref}} \right]^{\left(\frac{0.65T^*}{1+1.6T^*} \right)} K_{jump} \left[\frac{L_h^2(\rho_l - \rho_v)a_{SDB}}{4.41\sigma} \right]^{0.025} \quad (18)$$

A trend in the magnitude of K_{Jump} at transition is clear for the range of subcoolings investigated. No jump in heat transfer was observed for the high subcooling cases ($K_{Jump} \sim 1$, $\Delta T_{sub} = 27$ °C) while a jump was observed at lower subcoolings ($K_{Jump} < 1$, $\Delta T_{sub} = 18$ and 11 °C). Lee (Ref. 49) performed pool boiling experiments on space flights at various subcoolings and reported negligible heat transfer near saturation ($\Delta T_{sub} = 0.3$ °C). It was reported that the heat transfer at lower subcoolings was small due to negligible condensation at the bubble cap which allowed the bubble to grow and cover the entire heated area. These experiments of Lee (Ref. 49) imply $K_{Jump} = 0$ as the subcooling is reduced to 0 °C. Combining these observations, it can be concluded that K_{Jump} varies from 1 at high subcoolings to 0 at saturation.

The data for the 7 mm and 2.1 mm heater results also indicate a decreasing K_{Jump} with increasing heater size at a given subcooling. This can be attributed to the increased tendency of the smaller bubble (2.1 mm) to grow after transition into the SDB regime in order to balance the condensation and evaporation heat transfer, resulting in a smaller value of K_{Jump} .

Based on these trends where the jump increases with decreasing subcooling, increasing gas concentration, and decreasing heater size, the following equation was used to model K_{Jump} :

$$K_{jump} = 1 - e^{-C Ma} \quad (19)$$

where $Ma = -\frac{d\sigma}{dT} \frac{\Delta T_{sub,app} L_h}{\mu \alpha}$. The Marangoni number (Ma) is a nondimensional quantity that includes subcooling and heater size, and is often used to quantify microgravity heat transfer. Since the gradient of surface tension with temperature is negative for common fluids, Ma as defined above is always positive, and hence, the value of K_{Jump} varies from 0 to 1. Using the appropriate thermo-physical properties for FC-72, $C = 8.3 \times 10^{-6}$ yielded the smallest error in the predicted heat flux for all the available low-g data in Table 4. A plot of K_{Jump} and Ma versus subcooling for the four heater sizes investigated in this study is given on Figure 26(a). For large heaters and higher apparent subcoolings, Ma is large and hence the value of K_{Jump} is approximately 1 (Figure 26(a)). As the apparent subcooling is decreased and boiling occurs under saturated conditions, the value of Ma approaches 0 for all sizes and K_{Jump} approaches 0, resulting in negligible heat transfer in agreement with the observations of Lee (Ref. 49). The results of heat transfer prediction for the cases in Table 4 are shown on Figure 26(b). The overall agreement is good and the RMS error is 19 percent for the data under wide range of dissolved gas concentration, subcooling and heater sizes.

Finally, a comparison between the predictions based on the gravity scaling law for the SDB regime developed in the current study (Eq. (18)) and other models in the literature for the experimental the data points in Figure 26(b) is shown on Table 5. The models in the literature fail largely due to the use of a constant power law coefficient throughout the nucleate boiling regime. The current study based on the unified framework yields significantly lower error.

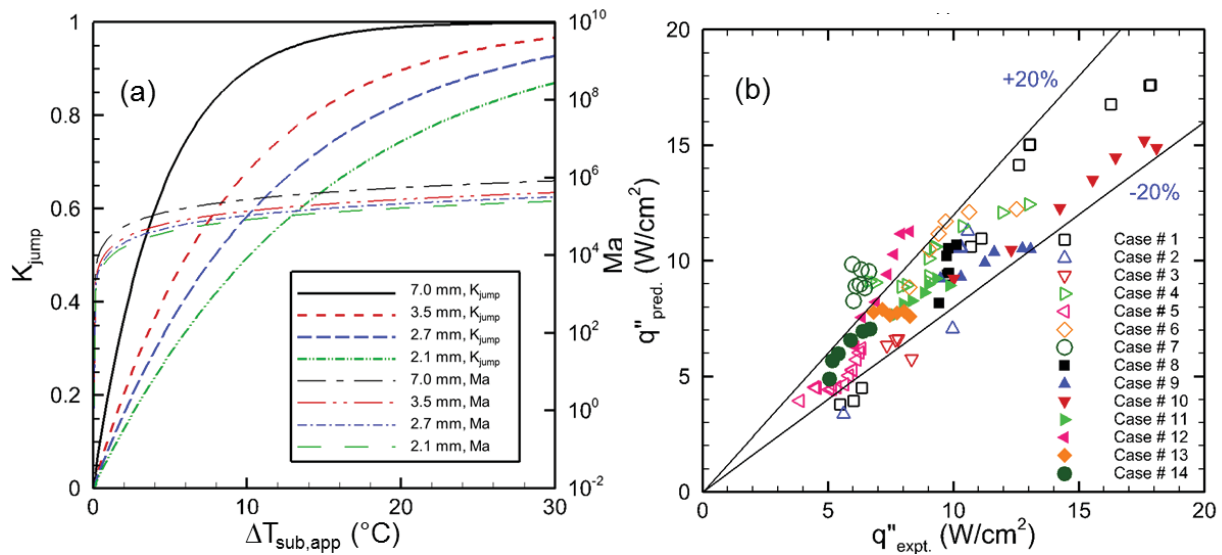


Figure 26.—(a) K_{Jump} at transition versus subcooling, and the (b) comparison of experimental and predicted heat flux values at 0.01g (RMS_{error} = 20 percent).

TABLE 5.—RMS ERROR IN PREDICTION USING THE AVAILABLE CORRELATIONS

Study	m	RMS error, percent
Rohsenow 1962 (Ref. 5)	0.5	82
Straub 2001 (Ref. 8)	0.13	40
Kannengieser et al. 2009 (Ref. 9)	0.17	35
Current Study	$0.65T^*/(1+1.6T^*)$	19

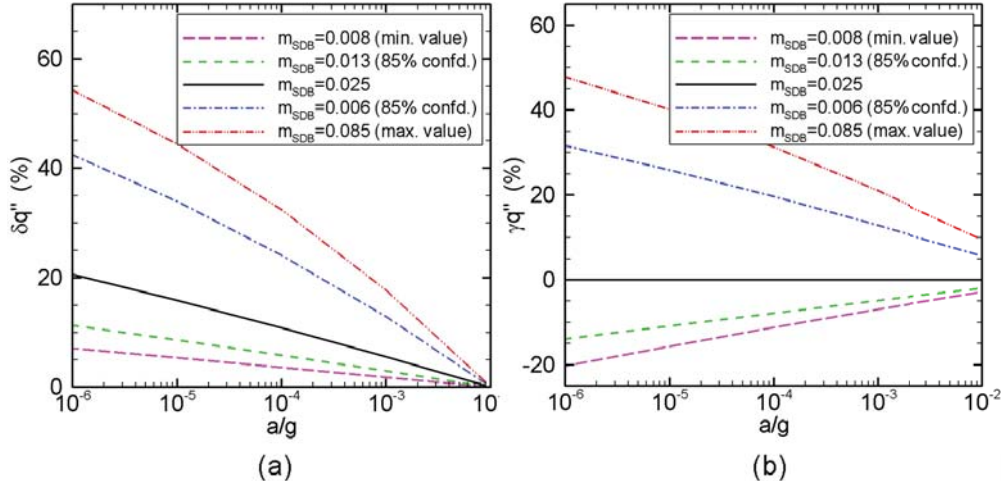


Figure 27.—Sensitivity of (a) microgravity acceleration, and (b) low gravity power law coefficient m on heat flux.

Sensitivity analysis.—The sensitivity of the heat flux prediction to the value of m_{SDB} is shown in Figure 27. A plot of the percent change in heat flux ($\delta q''$) with gravity for different values of m_{SDB} is shown in Figure 27(a) where

$$\delta q'' = \frac{q''_{0.01g, m_{SDB}} - q''_{a, m_{SDB}}}{q''_{0.01g, m_{SDB}}} \times 100 \quad (20)$$

For $m_{SDB} = 0.025$, the predicted heat flux only changes by 20 percent even though the acceleration is reduced by four orders of magnitude. Figure 27(b) shows the sensitivity of the heat flux ($\gamma q''$) to the power law coefficient m_{SDB} at any reference acceleration (a) in the SDB regime for the 7 mm heater.

$$\gamma q'' = \frac{q''_{a, 0.025} - q''_{a, m_{SDB}}}{q''_{a, 0.025}} \times 100 \quad (21)$$

Although the errors in heat flux due to errors in m_{SDB} at higher residual accelerations ($\sim 10^{-2}g$) are not significant, the error increases if the model is to be used to predict the heat flux at very high quality microgravity conditions ($\sim 10^{-6}g$). All these observations point towards a need to perform further experiments at different residual gravity levels to develop a better model for m_{SDB} .

2.6 Summary of Ground-Based Work

This section has highlighted the recent advances made towards the development of a heat flux scaling law for gravity effects on pool boiling using microheater arrays operated at constant temperature on low-gravity aircraft. Two boiling regimes (SDB and BDB) were identified, and scaling laws for boiling heat flux in the BDB and SDB regimes were developed. For large heaters and/or high gravity conditions, boiling was buoyancy dominated and the ebullition cycle dominated the contribution to heat transfer. As the acceleration and/or heater size was reduced, surface tension forces became increasingly important, leading to a transition to the SDB regime where a nondeparting coalesced bubble with large dry area resided on to the heater surface. The effect of gravity on pool boiling heat transfer in the SDB regime was smaller than in the BDB regime. Using the data from preliminary parabolic flight experiments, a

framework was developed whereby knowledge of pool boiling heat flux in the BDB regime could be used to predict heat transfer in the SDB regime. The scaling laws and conclusions were validated for experiments with $0.3 < L_h/L_c < 12$.

Although these equations may be valid outside this range, the presence of other boiling regimes cannot be ruled out and should be investigated. An example of another regime is illustrated by the boiling pattern observed during the orbital flight experiment results of Lee and Merte (Ref. 22) (Figure 3) where the coalesced bubble hovered just off the heater surface. Their experiments were performed during the orbital flights at very low gravity levels ($\sim 10^{-4}$ g, Table 6) and hence lower L_h/L_c than those for the results reported in this section (Table 6).

The MABE experiment on the Boiling eXperiment Facility (BXF) described in the next few sections is aimed at understanding boiling under high quality ($\sim 10^{-6}$ g), long duration microgravity conditions with n-perfluorohexane as the test fluid. MABE houses two constant temperature microheaters arrays (2.7 and 7 mm) similar to those used for the results discussed in this section. Results using heaters of various sizes in high quality microgravity conditions are reported, allowing a verification of the conclusions made so far.

TABLE 6.—DIFFERENT MICROGRAVITY ENVIRONMENTS AND THE CORRESPONDING PARAMETERS

a/g	Microgravity environment	L_h/L_c , ($L_h = 7$ mm, FC-72)
10^{-2}	PF	0.9
10^{-3}	-----	0.3
10^{-4}	SR, OF	0.09
10^{-5}	SR, OF	0.03
10^{-6}	ISS	0.009

3.0 MABE/BXF Apparatus

BXF was designed to study pool boiling in the low-g environment of the ISS. BXF incorporates two experiments in a single apparatus; MABE and UCLA's Nucleate Pool Boiling Experiment (NPBX). This section describes the test setup and parameters for the MABE, the subject of the current report.

The BXF apparatus (Figure 28) was composed of a Containment Vessel (CV) and an Avionics Box (AB) mounted inside the ISS Microgravity Science Glovebox (MSG). In addition, local acceleration measurements were provided by a Space Acceleration Measurement System (SAMS) head mounted within the MSG. The CV was comprised of a boiling chamber, a fluid control system, a temperature control system, a pressure control system, electronic and video data sensors, and heater control circuitry. NTSC cameras and embedded control boards were incorporated within the structure. A commercial off-the-shelf (COTS) high-speed digital camera (HSC) and microscopic lens was affixed to the CV to visualize the boiling process through several windows. The primary functions of the AB were power conversion and distribution and computer control for the facility operation. The signal processing electronics for the high-speed digital imager was attached to the top of the AB. Details of the MABE/BXF experiment are given below.

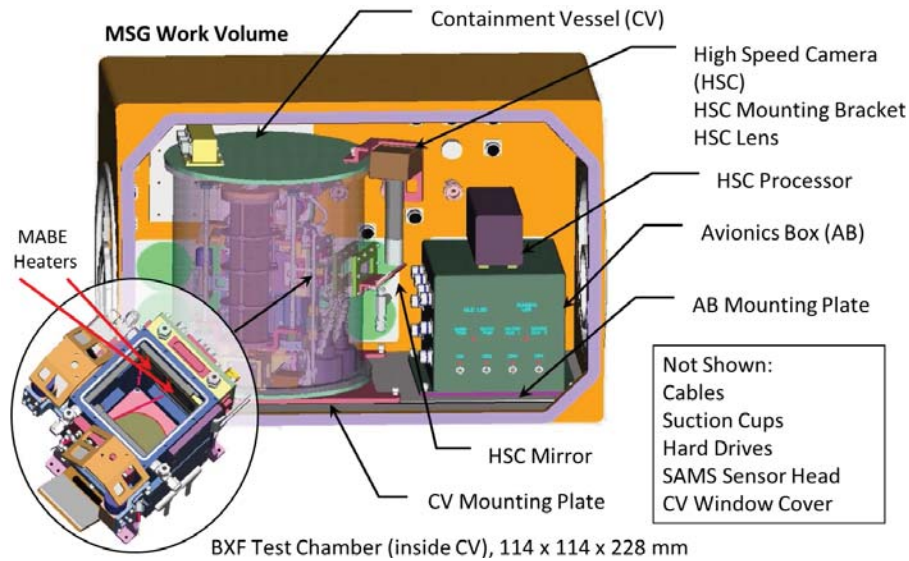
3.1 MABE Science Heaters

While most of the boiling studies to date used heater power as the independent variable, MABE used a constant temperature approach. There are several advantages to this:

- a. The risk of heater burnout is minimized, especially at critical heat flux and heater dryout conditions, since the feedback circuits automatically regulate the power required to keep each microheater at the set point.
- b. Lateral substrate conduction is minimized. Since adjacent microheaters are maintained at nearly the same temperature, there is very little thermal conduction between microheaters. Only the microheaters on the edges of the array conduct significant amounts of heat laterally outward through the quartz substrate. These microheaters actually serve as "guard heaters" for the remaining heaters.

Microheater arrays.—The two microheater arrays used in BXF are shown on Figure 29 (top right). An enlarged image of the 2.7 mm array with electrical leads is shown on the left. For the 2.7 mm array, each of the individual heaters was about 0.26- by 0.26-mm² in size, had a nominal resistance of 975 Ω, and a nominal temperature coefficient of resistance (TCR) of 2.3 Ω/°C. For the 7.0 mm array, individual heaters were about 0.70- by 0.70-mm² in size, had a nominal resistance of 250 Ω, and a nominal TCR of 0.6 Ω/°C.

To manufacture the heaters, platinum was sputtered onto the entire surface of a 500 μm thick wafer to a thickness of 0.2 μm, a layer of photoresist was deposited and patterned to define the heater geometry, then the platinum from the unmasked areas (serpentine pattern) was removed using an ion mill to form a resistance heater. Gold was then vapor deposited to a thickness of 1 μm onto the surface, the gold power leads were masked off, and the remaining gold was removed using a wet chemical etch. A 1 μm thick layer of SiO₂ was finally deposited over the heater array to provide the surface with a uniform surface energy. The boiling surface was viewed under an electron microscope, and the surface roughness was found to be on the order of the thickness of the gold power leads to the heaters (~1 μm).



BXF Test Chamber (inside CV), 114 x 114 x 228 mm

Figure 28.—BXF mounted in MSG with transparent CV. (Inset: view inside the boiling chamber housing the two microheater arrays.)

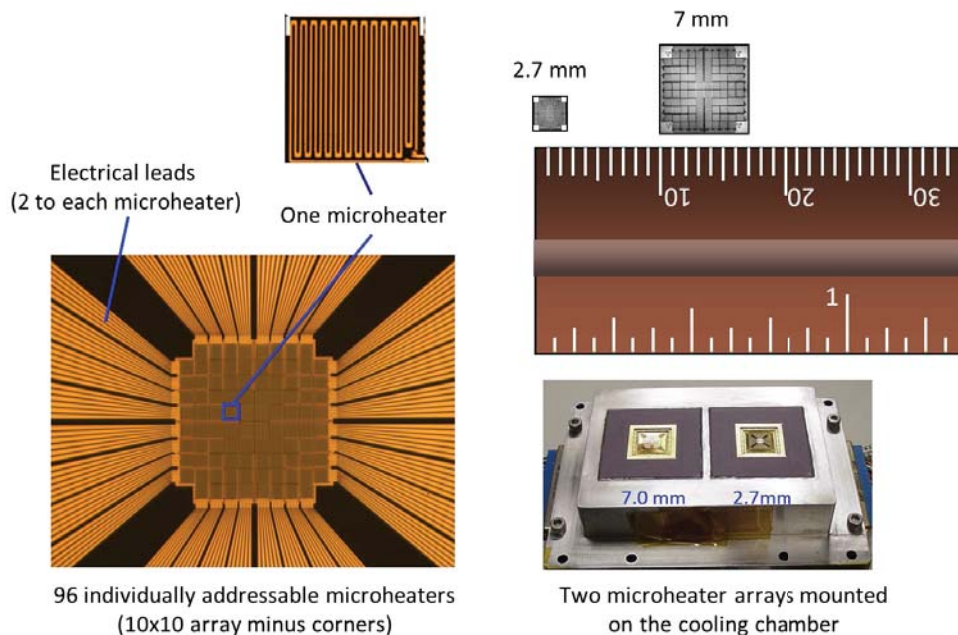


Figure 29.—Images of the two microheater arrays.

The completed quartz wafer was diced into chips, each containing a single heater array. The chips were mounted onto a Pin Grid Array (PGA) package using epoxy adhesive, and the pads on the PGA were connected to the power leads of the heater array chip using a conventional wire bonding technique. The completed package was then mounted in a PGA socket that was in turn mounted into the cooling chamber (Figure 9, bottom right). Electrical connections were then made to the MABE embedded controller boards.

Since a single processed wafer contained multiple microheater arrays, the flight arrays were chosen based on the results of resistance measurements. The microheater arrays that were selected for space flight typically had the most “functional” microheaters and the smallest standard deviation of resistance for those functional heaters. Both “shorts” and “opens” occasionally occurred during the manufacturing and assembly process. The characteristics of the microheater arrays selected for the space flight experiment are summarized in Table 7.

TABLE 7.—MICROHEATER ARRAY PARAMETERS

	2.7 mm microheater array	7.0 mm microheater array
Minimum resistance at 25 °C, Ω	918	236
Maximum resistance at 25 °C, Ω	1008	328
Average resistance at 25 °C, Ω	970	292
Standard deviation, Ω	20	20
Number of “open” microheaters	1	2
Number of “shorted” microheaters	0	2
Number of “good” microheaters	95	92
TCR, Ω/°C	2.3	0.6

Control circuit.—The temperature of each heater in the array was kept constant by feedback circuits based on a Wheatstone bridge, similar to the technique used in constant temperature hot-wire anemometry. An optimized circuit was needed that could provide the necessary temperature sensitivity over the range of operation (50 to 110 °C) as well as provide a “continuity” check at room temperature using the circuit for all 96 microheaters. The control circuits for the 2.7 and 7.0 mm microheater arrays along with the optimal resistances (R_{10} , R_{14} , R_{17} , and R_{13}) for best temperature sensitivity are shown on Figure 30.

The chopper op amp was used to sense an imbalance in the Wheatstone bridge, represented by R_h , R_{10} , R_{14} on the left and R_{17} , R_{13} , and R_{AD5235} on the right. The op-amp (LTC1150CS8) output a voltage proportional to the imbalance between V_{left} and V_{right} to the gate of the transistor (MMBT2222A/SOT3) allowing additional current to flow from the 16.5 V source through the bridge. This current caused an increase in the temperature of the heater (joule heating) with a corresponding increase in resistance. The resistance of the heater continued to rise until a new equilibrium state was reached corresponding to a balance in the Wheatstone bridge ($V_{\text{left}} = V_{\text{right}}$). The Wheatstone bridge balance could be adjusted by changing the digital potentiometer (AD5235) setting. The circuit was designed so that very little power was dissipated across the right side of the bridge (R_{17} , R_{13} were relatively large). R_{10} , R_{14} , R_{17} , and R_{13} were precision resistors whose value changed very little with temperature. The frequency response of the circuit/heater combination was measured to be ~15 kHz, which is much faster than the dynamic behavior of the boiling process. The time-varying voltage across the heater resistance ($V_{\text{top}} - V_{\text{left}}$) in Figure 30 along with the heater resistance at the set temperature was measured so the total power dissipated by the heater to maintain it at constant temperature could be computed. Due to a limitation in the maximum voltage that could be recorded by the data acquisition system, a differential amplifier circuit with a gain of 0.5 was used to scale down the voltage ($V_{\text{top}} - V_{\text{left}}$) across the heater resistance to V_{amp} . The output voltage to the data acquisition units V_{amp} could be related to the voltages across the heater as follows:

$$V_{\text{amp}} = \frac{(R_f + R_1)R_g}{(R_g + R_2)R_1} V_{\text{top}} - \frac{R_f}{R_1} V_{\text{left}} \quad (22)$$

Since the current flowing through the heater was the same as that flowing through R_{10} and R_{14} to the ground, a second relation between V_{top} and V_{left} is given by:

$$\frac{V_{\text{amp}} - V_{\text{left}}}{R_h} = \frac{V_{\text{left}}}{R_{10} + R_{14}} \quad (23)$$

Solving these two equations for the voltage across the heater yields

$$V_h = V_{\text{top}} - V_{\text{left}} = R_1(R_2 + R_g)R_h \left[\frac{V_{\text{amp}}}{R_{10}(-2R_2R_f + 2R_1R_g) + (R_1 + R_f)R_gR_h} \right] \quad (24)$$

Calibration.—Calibration of the microscale heater array was performed by placing the array in a constant temperature environment. Once thermal equilibrium was attained, the calibration program determined the digital potentiometer (AD5235) resistance setting which balanced the Wheatstone bridge (Figure 30) as indicated by a sudden increase in V_{amp} as the digital potentiometer setting was increased. These settings, called DQ values, were written to a text file and stored for future use. Calibration was performed in 5 °C increments between 60 to 110 °C. Calibration of the heater array was repeatable within 3 digital potentiometer positions for all heaters.

The theoretical DQ values based on the TCR of the heaters and the experimental values were very close validating the calibration procedure. Although the DQ values corresponding to different heaters at any temperature were different as might be expected since the heater resistance values varied, the slope of the curve, and hence their TCR, was almost same. To set the heater temperatures during an experiment, the digital potentiometer was set to the DQ corresponding to the desired temperature.

3.2 Test Fluid

BXF contained approximately 4 liters of *normal*-perfluorohexane (nPFH), the linear isomer of C_6F_{14} . This isomer is also the principal constituent of FC-72, a heat transfer fluid manufactured by 3M. nPFH was selected as the test fluid in place of FC-72 to address a safety concern raised by a NASA toxicologist

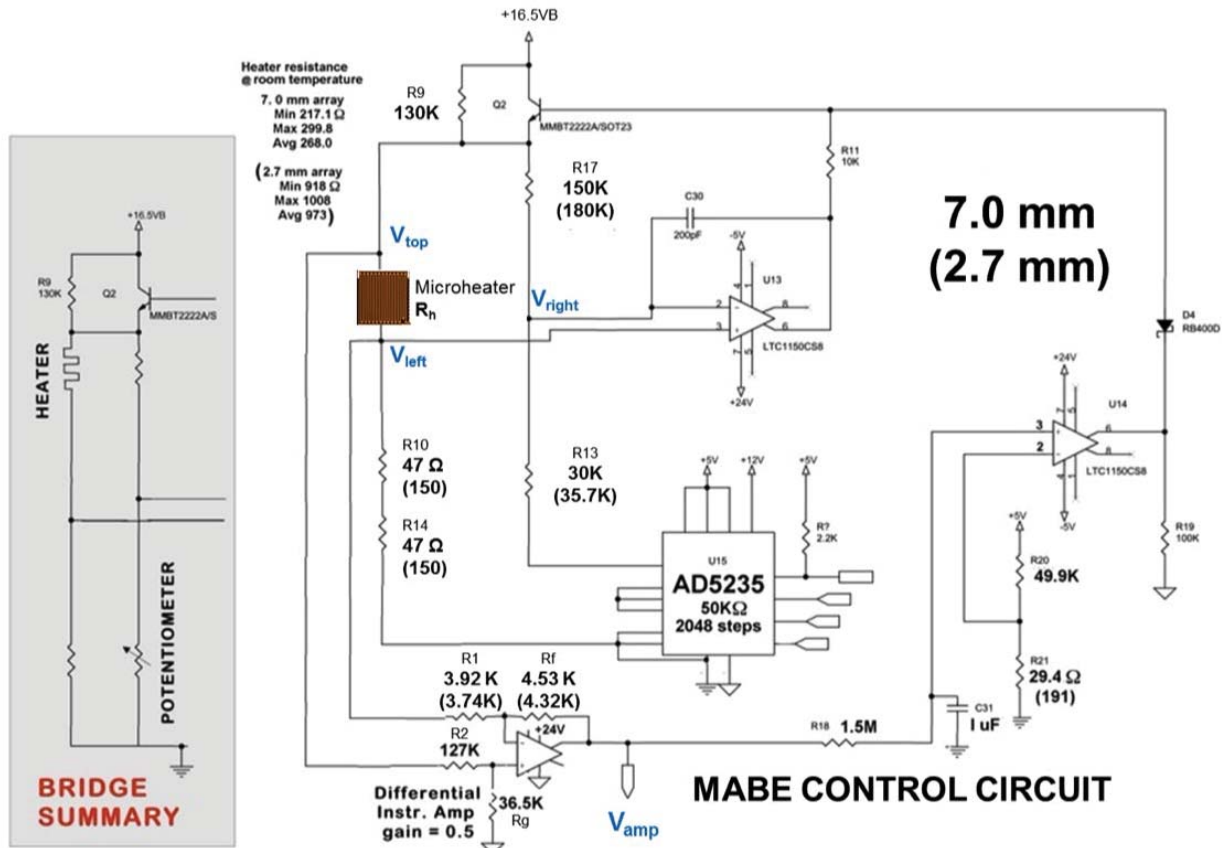


Figure 30.—The MABE feedback circuit.

that other isomers within FC-72 when exposed to temperatures above 200 °C could generate perfluoroisobutene (PFiB), a with an acceptable exposure limit of 10 parts per billion or less,. The safety concern was based on a caution statement within the Material Safety Data Sheet and on the chemical similarity of a FC-72 isomer to some of the branched isomers studied by Tortelli and Tonelli (Ref. 50). While BXF had safety shutdowns to limit the temperatures within the boiling chamber to no more than 60 °C, if there were a leak, the ISS Trace Contaminant Control Subassembly (TCCS) had a catalytic reactor bed that operated in excess of 450 °C. Based on an extensive literature review and a series of experiments under exposure conditions similar to the ISS TCCS, these concerns were alleviated (Ref. 51). However, because of the chemical composition of FC-72 and the difference in the normal boiling temperatures of some of the constituents (Ref. 52), the test fluid was changed to nPFH.

3.3 Boiling Chamber

A boiling chamber with interior dimensions of approximately 228- by 114- by 114-mm³ was fabricated from aluminum. An external view of the chamber can be seen through the transparent CV in Figure 28. A cutaway, top-down view shown in Figure 28 shows the placement of the two MABE microheater arrays on the side. A photograph of the flight hardware showing the internal components is shown on Figure 31.

NTSC video cameras mounted to the boiling chamber captured side views of the boiling process for recording to the MSG video tape recorders. Because the microheater arrays were semitransparent, it was also possible to view through the microheater array and a back-side cooling chamber (described below). This view through the bottom of the MABE microheater array was captured at 500 images per second for 4 s per test using a Photron Ultima-512 high speed digital imager with 512 by 512 pixel resolution. Image data captured by this camera was stored for post-flight data analysis on removable hard drives. An LED array was used to provide backlighting for each of the views.

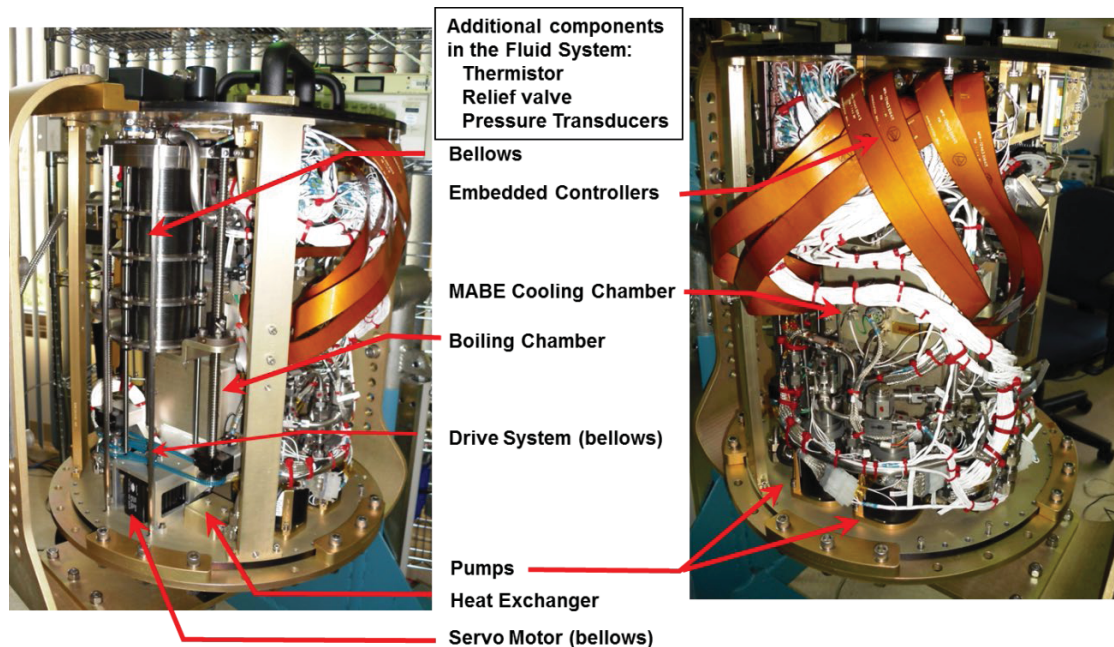


Figure 31.—A picture BXF hardware with the containment vessel removed.

3.4 Flow System

The flow system was designed to condition the test fluid, maintain system pressure during a test, and provide cooling to the backside of the MABE microheater arrays. The flow path illustrated in Figure 32 includes parallel pumps, isolation solenoid valves, filter, flow meter, check valves, heat exchanger, cooling chamber, heaters and the boiling chamber.

To mitigate the risk associated with part failure, redundancy was provided in both the pumps and the solenoid valves. Only one valve and pump was operated at any given time. The gear pumps were run for approximately 100 hr before insertion into the test loop to minimize the amount of impellor material shed into the flow. This protocol was based on the pump manufacturer’s recommendation. Nonetheless, a 10 µm filter was placed downstream of the pumps to capture any additional debris.

“Normally-Open” solenoid valves (S1 and S2) were used. Once the test fluid in the boiling chamber reached the desired temperature, both valves could be commanded to the shut position to isolate the boiling chamber from flow during data acquisition. However, only one valve was shut at any time to allow both the fluid to expand and contract in order to maintain an acceptable pressure difference between the boiling and cooling chambers to prevent structural failure of the MABE heater arrays.

Flow into the boiling chamber was through three open ended tubes at the top of the chamber. These tubes surrounded cartridge heaters which were used to condition the fluid. Six thermistors were strategically located to determine the homogeneity of the temperature distribution within the boiling chamber prior to the start of a test, and obtain limited temperature profiles during the test. The operating temperature range of BXF was 35 to 59 °C. The fluid exited at the bottom of the chamber.

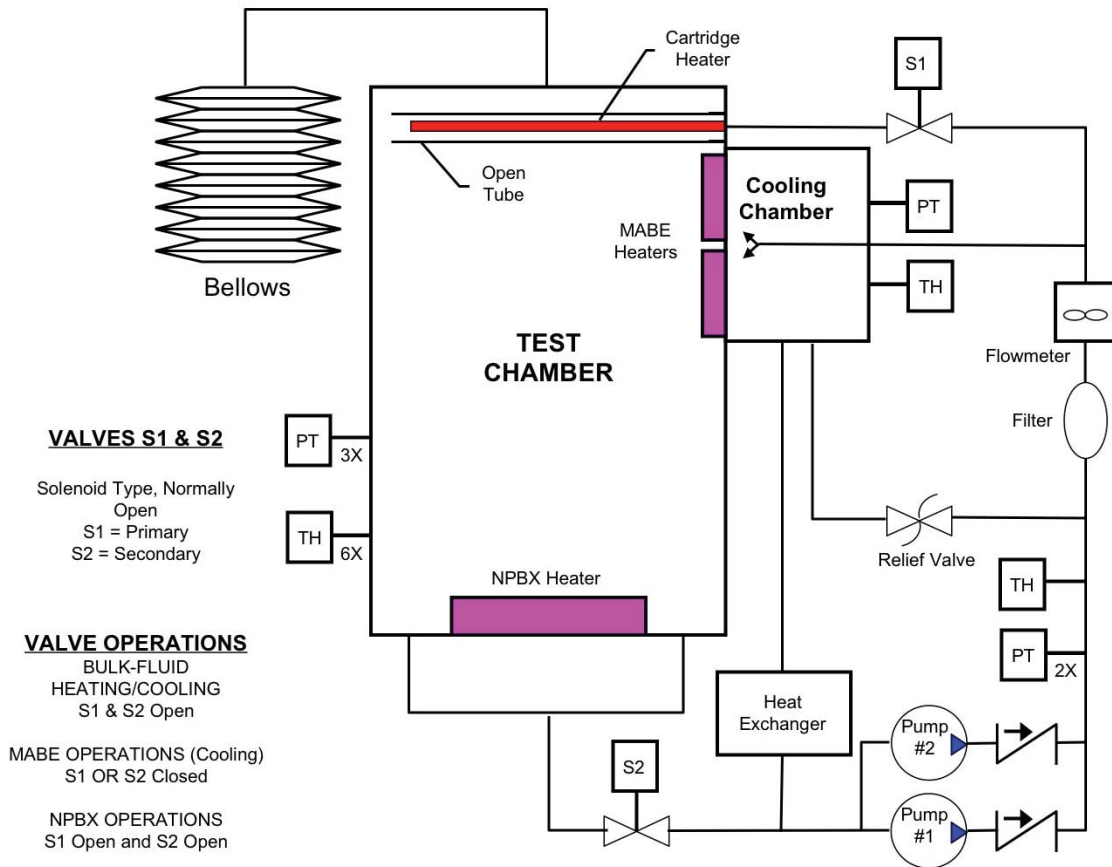


Figure 32.—BXF flow schematic

When the CV was mounted within the MSG, the heat exchanger was positioned directly above the MSG cold plate. While the MSG did provide some cooling via its air recirculation system, the use of the MSG cold plate minimized the size of the BXF heat exchanger.

System pressure was maintained via a bellows. The bellows was driven by a stepper motor and sized to accommodate the expected fluid expansion due to the liquid density differences between 20 and 60 °C and the growth of a bubble up to 7 cm in diameter for the NPBX. The operating pressure range was 61 to 270 kPa.

3.5 Cooling Chamber

The primary purpose of the cooling chamber was to ensure that the microheater arrays were always “ON” during a test. While the control circuitry was designed to sense and control temperatures to within 0.35 °C, it was possible that once the heaters achieved their set point, the control circuitry could shut off power to some adjacent heaters that might be at slightly cooler temperature, but still within the 0.35 °C margin, resulting in lateral heat conduction into these deactivated microheaters. To prevent this scenario, it was necessary to force a minimal amount of cooling to the backside of the MABE heater array by jetting cooler fluid onto it.

The second purpose of the cooling chamber was to minimize the pressure differential across the MABE quartz substrate, and thus the pressure differential between the cooling chamber and the boiling chamber. The benefit of this approach is that the cooling and boiling chamber structures could then carry the brunt of the pressure induced loading that the fluid saw during testing for pressure conditions ranging from 61 to 270 kPa.

The cooling chamber provided the mounting for both MABE microheater arrays that were mounted into PGAs. A printed circuit board and “flex circuits” provided the interface between the PGAs and multiple conductor connectors that were welded into the side of the cooling chamber.

3.6 Embedded Control Circuitry

To minimize the number of electrical connectors through the CV wall, embedded controller (EC) boards were located in the CV. Power and commands were fed from the AB to the ECs, which dispersed and interpreted them as appropriate. The ECs sent data and status back to the AB. This is illustrated in Figure 33. Two MABE EC’s, one dedicated to each microheater arrays, were used. The BXF EC was responsible for the remaining controller assignments which included controlling the NPBX heater, bulk fluid temperature, pumps, valves, pressure control, thermistors, cameras, lighting, and MABE array selection. The BXF EC also produced a 500 Hz clock signal which that was used to synchronize the trigger a data acquisition cycle from the 96 microheaters and the high-speed video frame.

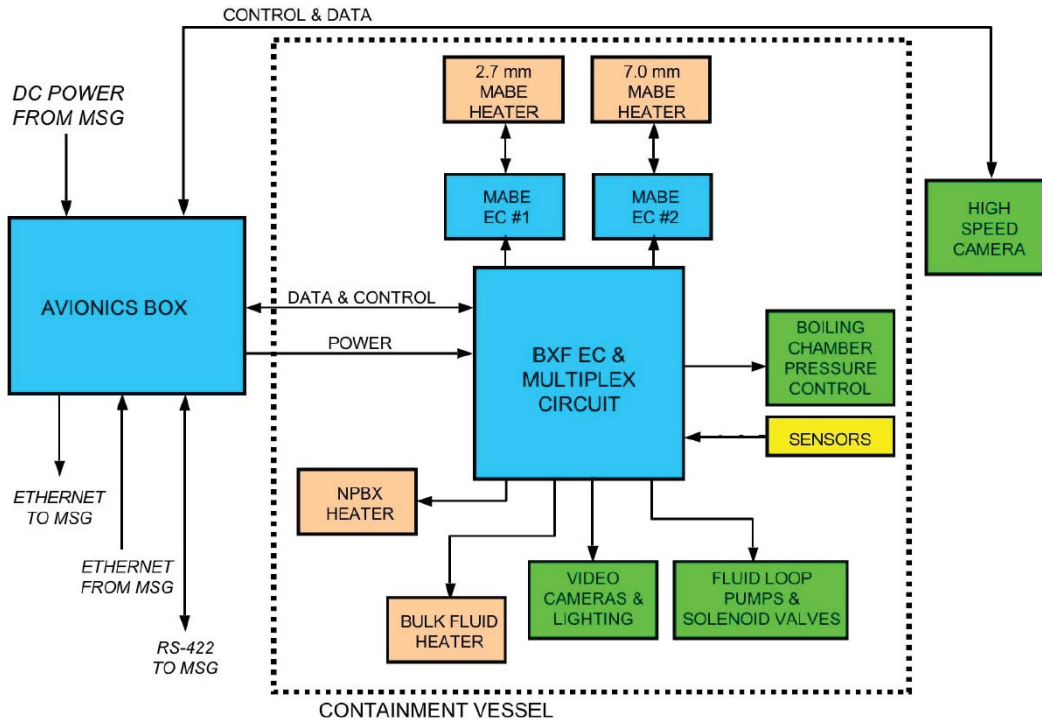


Figure 33.—BXF control system block diagram.

4.0 Test Matrix, Data Acquisition and Reduction, and Uncertainty Analysis

4.1 Test Matrix

A summary of the full Earth gravity test matrix is shown on Table 8. A subset of this test matrix was run on ISS. The test points were designed such that the effects of wall superheat, liquid subcooling, pressure, and heater size on boiling heat transfer could be obtained in an efficient manner. CHF was reached for a majority of the test conditions, generating a wealth of data regarding the influence of these parameters on boiling heat transfer. At each test condition, the heater temperature was decreased in 5 °C/2.5 °C increments starting from a maximum heater temperature higher than T_{CHF} to a temperature lower than that required for ONB. Three heater sizes (96, 64, and 36) were tested. Regular 30 Hz video (side and bottom) was also acquired for better visualization of the phenomena during these tests.

4.2 Data Acquisition

The fluid was first conditioned and the bulk liquid was brought to the desired temperature (column 4) and pressure (column 3) as per the test number and run number in the test matrix (Table 8). Data acquisition at 120 Hz commenced next. The backside cooling jet was turned on at the same time and allowed to stabilize for a few seconds. The LED array illuminating the boiling chamber was then momentarily turned off—the step change in voltage across the LED recorded by the data acquisition system and the change in illumination observed in the video were used to synchronize the video and the data. Five seconds into the start of cooling jets, the heater was set to the desired temperature T_{wall} (column 6). Due to the smoothness of the microheater arrays (surface roughness on the order of ~ 1 μm) and the wetting nature of the test fluid, no nucleation on the heaters at nominal nucleate boiling temperatures was observed. After 5 s at T_{wall} , the heater temperature was changed to 130 °C to initiate nucleation on the heater surface. The heater temperature was then brought back to T_{wall} , however, this time boiling was established and the heater experienced a higher heat transfer relative to the first 5 s where heat transfer was mainly by natural convection/conduction. The heater was turned off after 30 s of boiling data has been acquired.

TABLE 8.—TEST MATRIX FOR EARTH GRAVITY EXPERIMENTS
[Tests under conditions corresponding to test numbers 10, 11, 13, 14, 15, 17, and 18 were obtained on the ISS.]

Test no.	Heater, mm	P , psia, atm	T_{bulk} , °C	ΔT_{sub} , °C	T_w , °C	No. of active elements	Total no. of tests
1	2.7	1	30	26	70,72.5,75,77.5,80,82.5,85,87.5,90,95	96,64,36	30
2	2.7	1	45	11	70,72.5,75,77.5,80,82.5,85,87.5,90,95	96,64,36	30
3	2.7	1	55	1	70,72.5,75,77.5,80,82.5,85,87.5,90,95	96,64,36	30
4	2.7	0.58	30	11	55,57.5,60,62.5,65,67.5,70,72.5,75,80	96,64,36	30
5	2.7	0.58	40	1	55,57.5,60,62.5,65,67.5,70,72.5,75,80	96,64,36	30
6	2.7	1.6	45	26	85,87.5,90,92.5,95,97.5,100,102.5,105,110	96,64,36	30
7	2.7	1.6	60	11	85,87.5,90,92.5,95,97.5,100,102.5,105,110	96,64,36	30
8	2.7	1.86	50	26	90,92.5,95,97.5,100,102.5,105,107.5,110,115	96,64,36	30
9	2.7	1.38	40	26	80,82.5,85,87.5,90,92.5,95,97.5,100,105	96,64,36	30
10	7.0	1	30	26	70,72.5,75,77.5,80,82.5,85,87.5,90,95	96,64,36	30
11	7.0	1	45	11	70,72.5,75,77.5,80,82.5,85,87.5,90,95	96,64,36	30
12	7.0	1	55	1	70,72.5,75,77.5,80,82.5,85,87.5,90,95	96,64,36	30
13	7.0	0.58	30	11	55,57.5,60,62.5,65,67.5,70,72.5,75,80	96,64,36	30
14	7.0	0.58	40	1	55,57.5,60,62.5,65,67.5,70,72.5,75,80	96,64,36	30
15	7.0	1.6	45	26	85,87.5,90,92.5,95,97.5,100,102.5,105,110	96,64,36	30
16	7.0	1.6	60	11	85,87.5,90,92.5,95,97.5,100,102.5,105,110	96,64,36	30
17	7.0	1.86	50	26	90,92.5,95,97.5,100,102.5,105,107.5,110,115	96,64,36	30
18	7.0	1.38	40	26	80,82.5,85,87.5,90,92.5,95,97.5,100,105	96,64,36	30
Total number of tests							340

4.3 Data Reduction

The objective of the data reduction was to accurately estimate the amount of heat transferred from each individual heater element to the boiling fluid. The first step involved calculation of the total power generated at each element. Part of this power was transferred to the liquid and the remainder was conduction into the substrate. The second step involved estimation of the power conducted laterally into the substrate or through the substrate into the backside cooling fluid so the power transferred to the liquid could be estimated. The following sections explain these steps.

Raw heat flux calculation.—The scaled voltage V_{amp} from the data acquisition unit was converted to a voltage across the heaters using Equation (24). The voltage across the i^{th} heater element ($V_{h,i}$) along with heater resistance ($R_{h,i}$) at the set temperature (T_h) and the area (A) were used to calculate the raw heat transfer ($q''_{gen,i}$) for each individual heater element (i):

$$q''_{total,i} = \frac{V_{h,i}^2}{A_i R_{h,i}} \quad (25)$$

The data acquired within the first 5 s was later used to estimate and subtract the substrate conduction losses from the overall heat transfer to accurately estimate the heat flux utilized for boiling. This is explained using an example later in this section. Side and bottom view video data were recorded at ~ 30 Hz starting in the natural convection regime throughout the data acquisition period.

The nominal area (A_i) of each element in the 7- and 2.7-mm microheater arrays was 0.7- by 0.7-mm² and 0.27- by 0.27-mm², respectively. Changes in heater temperature changed the heater resistance according to the following relation:

$$R_{h,i} = R_{ref,i} + TCR * (T_h - T_{ref}) \quad (26)$$

where TCR is the temperature coefficient of resistance for the microheaters. Finally, the spatially averaged heat flux was calculated as follows:

$$q''_{total} = \frac{\sum_{i=1}^N q''_{total,i}}{N} \quad (27)$$

Only a portion of the total heat generated calculated above was actually delivered to the fluid. The next section describes the methodologies adopted to estimate the portion of heat transfer utilized for boiling.

Substrate conduction.—A simplified resistance network model was used to identify the relative magnitudes of lateral conduction and backside cooling losses. Figure 34 shows a schematic of the chip along with the major heat transfer paths. Using the heater geometry and material properties of the chip, estimates of the values of thermal resistances for these heat transfer paths are shown. The thermal resistance in the lateral direction was almost two orders of magnitudes higher than that to the backside of the chip, resulting in negligible lateral conduction losses. This assumption was also validated by 3-D COMSOL model. Two boundary conditions were used at the side walls. In the first analysis, the side walls were assumed to be adiabatic. In the second analysis, the side walls were prescribed the bulk liquid temperature (this is closer to the actual experimental condition). The difference between the results of the two analyses (max. 3 percent) was negligible. The lateral conduction term was also within 1 percent of the backside losses.

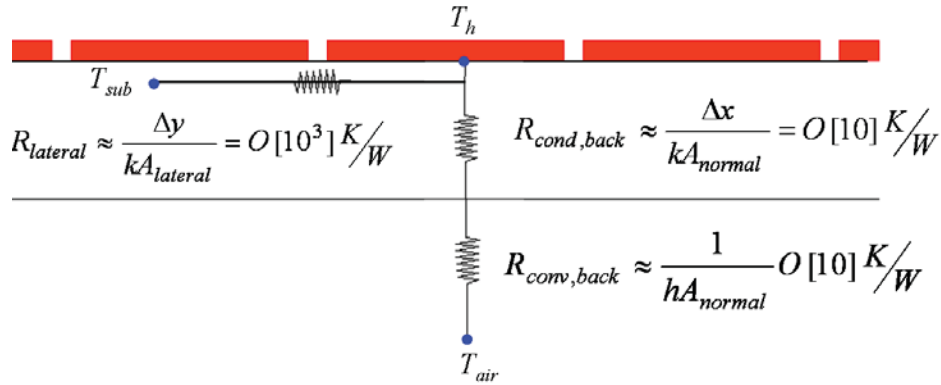


Figure 34.—Simplified resistance network model for the major heat transfer paths associated with an element in the microheater array (Δx and Δy are dimension vertical and lateral dimensions respectively).

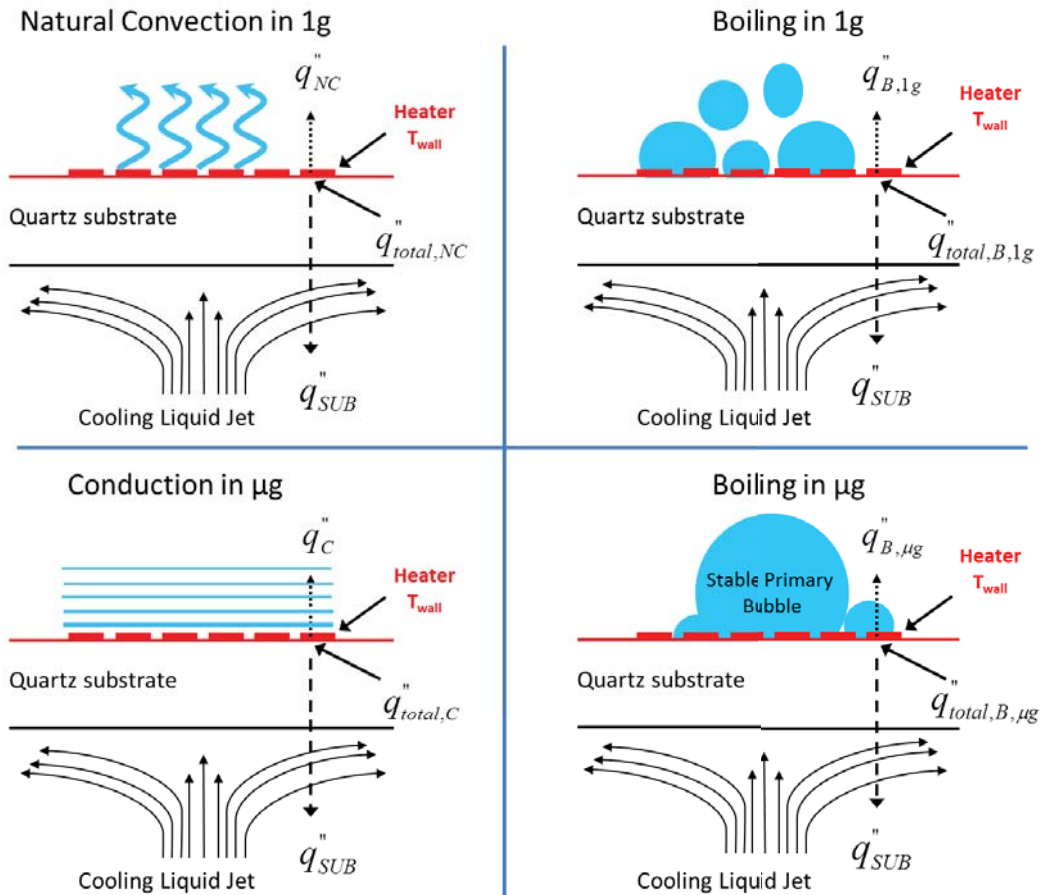


Figure 35.—The schematic of the heat transfer contributions under different gravity conditions.

Based on the above assumption, heat transfer paths within the microheater array chip are illustrated in Figure 35. The heaters are maintained at a temperature T_{wall} for all four cases. First consider the top two figures illustrating the Earth gravity situations. The figure on top left shows a case when boiling has not been initiated on the heater. In this case, a portion of the generated heat ($q''_{total,NC}$) is convected to the fluid (q''_{NC}) while the other portion is transferred to the backside (q''_{SUB}). The figure on top right depicts a

case where boiling is occurring on the heater surface maintained at T_{wall} . Similar to the previous case, a portion of the overall generated heat ($q''_{total,B,lg}$) is used for boiling ($q''_{B,lg}$) while the remaining heat is transferred to the cooling jet through the backside of the heater (q''_{SUB}). It should be noted here that at a given heater temperature T_{wall} , the loss to the backside (q''_{SUB}) is independent of the conditions on the liquid side of the heater. Using these two cases, an equation can be written as follows:

$$q''_{B,lg} - q''_{NC} = q''_{total,B,lg} - q''_{total,NC} = q''_{SUB} \quad (28)$$

The natural convection heat transfer at Earth gravity conditions is significantly smaller than boiling heat transfer ($q''_{B,lg} \gg q''_{NC}$). As a result, the right side of Equation (29) is a good approximation for the boiling heat flux, the quantity of interest is this work.

$$q''_{B,lg} \sim q''_{total,B,lg} - q''_{total,NC} \quad (29)$$

Similarly under microgravity conditions (Figure 35, bottom two figures), the heat transfer through conduction is much smaller than through boiling ($q''_C \ll q''_{B,\mu g}$) and hence the boiling heat flux can be estimated as follows:

$$q''_{B,\mu g} \sim q''_{total,B,\mu g} - q''_{total,C} \quad (30)$$

Sample data reduction steps.—These data reduction steps are now explained with the help of an example. Heat flux evolution during this experiment is shown on Figure 36. The top left plot is the heat flux evolution for a single heater numbered 32. The different stages of data acquisition are clearly visible. The first 3.2 s represent the time when the heaters were off and backside cooling jet was allowed to achieve steady state condition. The heater was set at T_{wall} (80 °C) between 3.2 and 7.5 s. During this period, heaters were regulating to maintain elements at 80°C and heat was lost to fluid through natural convection (NC) as well as conducted to the backside where it was lost to the cooling jet. At 7.5 s, heater temperature was raised to temperature of 130 °C ($T_{nucleation}$) to initiate nucleation on the microheaters (N). At this temperature, the microheater array was in the film boiling regime. At 13.7, the heater temperature was again brought back to T_{wall} (80 °C) and the heater experienced nucleate boiling (NB) from 13.7 s until the end of experiment at 30 s. The portion of the data run that is of interest is comprised of two components, one used for boiling while the other lost to the cooling jet through the backside of the heater. The regime labeled as NC represents the top left plot on Figure 35 while the regime labeled as NB represents the situation in top right plot on Figure 35. The time average of the heat flux during NC regime was calculated to serve as the baseline as defined by Equation (29). The top right plot on Figure 36 shows the heat flux after subtraction of this baseline. The heat flux value of 18.7 W/cm² during the NB regime on this plot represents the boiling heat flux provided by heater no. 32. The heat transferred during the NC regime is reduced to zero as expected.

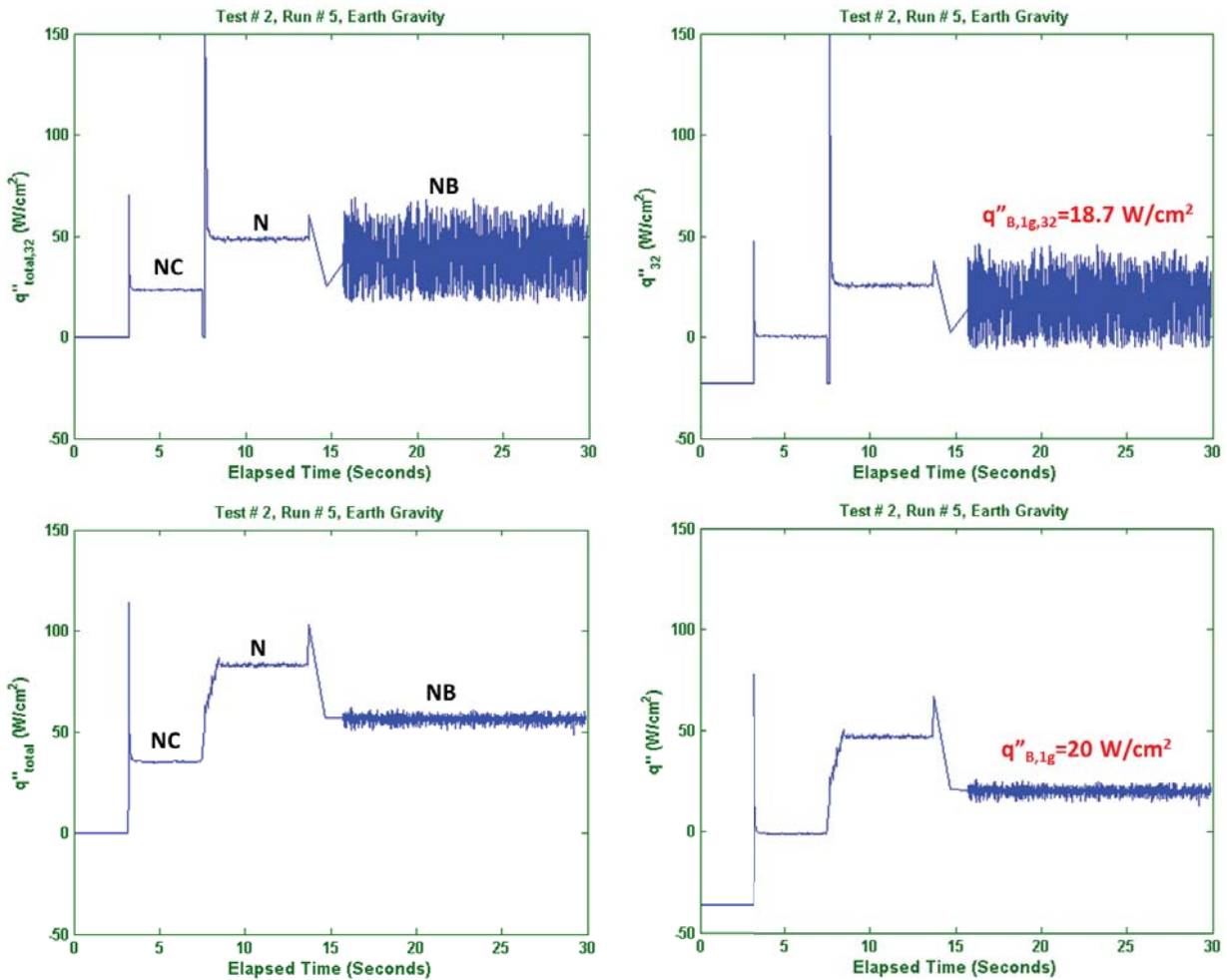


Figure 36.—Heat flux evolution for a single heater (no. 32, top) and 96 heater average (bottom) during a sample Earth gravity experiment (Test no. 2, Run no. 5)

The bottom two plots represent the same calculation performed over the average of 96 heaters instead of just heater no. 32 as explained above. The bottom left plot is the area averaged heat flux evolution of the microheater array for this particular run. The different stages and the associated timeline are same as that for the single heater. The bottom right plot on Figure 36 shows the area averaged heat flux evolution after the subtraction of baseline heat transfer due to natural convection and substrate conduction losses to the cooling jet. The heat flux during the NB regime on this plot is a representation of the area averaged boiling heat flux provided by the microheater array. Again, the area averaged heat transferred during the NC regime is reduced to zero. Time and area averaged heat flux of 20 W/cm² in the NB regime is of interest in this study and provides a data point on the boiling curve. All points on the boiling curve and those presented elsewhere in this report were obtained using a similar data reduction routine.

Having explained the data reduction procedure on a heat flux versus time plot, some important details are now highlighted through the spatial heat flux distribution plots shown on Figure 37 and Figure 38. The top left plot on Figure 37 represents the spatial distribution of total/raw heat flux at 5.16 s, i.e., in the natural convection regime (NC, bottom left on Figure 36). The heat transfer from the peripheral elements is relatively large due to enhanced convection and 2-D conduction losses to the substrate. The convection heat transfer is known to increase at the periphery of a heater due to the inflow of cooler liquid from the sides. For heater elements completely surrounded by other regulating heaters, the temperature in the substrate varies primarily in the normal direction (1-D conduction) with very little lateral conduction as

shown by Henry (Ref. 53). His analyses also showed that for the edge elements, 2-D conduction losses were significant and could not be ignored.

The top right plot is the time averaged heat flux distribution in the natural convection regime (3.2 to 7.5 s), and is an estimate of the substrate conduction (third term in Eq. (28)). The bottom left figure is the residual heat flux at 5.16 s. Although the value of heat transfer after substrate conduction is has some minor fluctuations and is not zero at any instant, the time averaged value throughout the *NC* regime is zero for each heater as shown on the bottom right plot (note the very small scale for this plot).

The top left plot on Figure 38 represents the spatial distribution of total/raw heat flux at 20.68 s, i.e., in the nucleate boiling regime (*NB*, bottom left on Figure 36). Again the heat transfer for the peripheral heaters is relatively high due to lateral conduction and entrainment of the cooler liquid from the bulk. The top right is the time averaged plot of the total heat flux during the boiling regime. The bottom left figure is the instantaneous boiling heat flux at each heater calculated by subtracting the heat flux in the top right of Figure 38 (estimated substrate conduction) from the top left of Figure 38. A time average of all such plots in the *NB* regime gives us the bottom right plot, the time averaged boiling heat flux at each heaters. The area averaged value obtained from this plot is 20.0 W/cm^2 , the same as the value from the bottom right plot in Figure 36. Although the time averaged color-map plots shown in these two figures do not show any interesting trend due to smaller bubble sizes and the random boiling nature in Earth gravity, the plots in the microgravity environment are interesting due to the presence of a coalesced primary bubble and significantly higher heat transfer at the periphery.

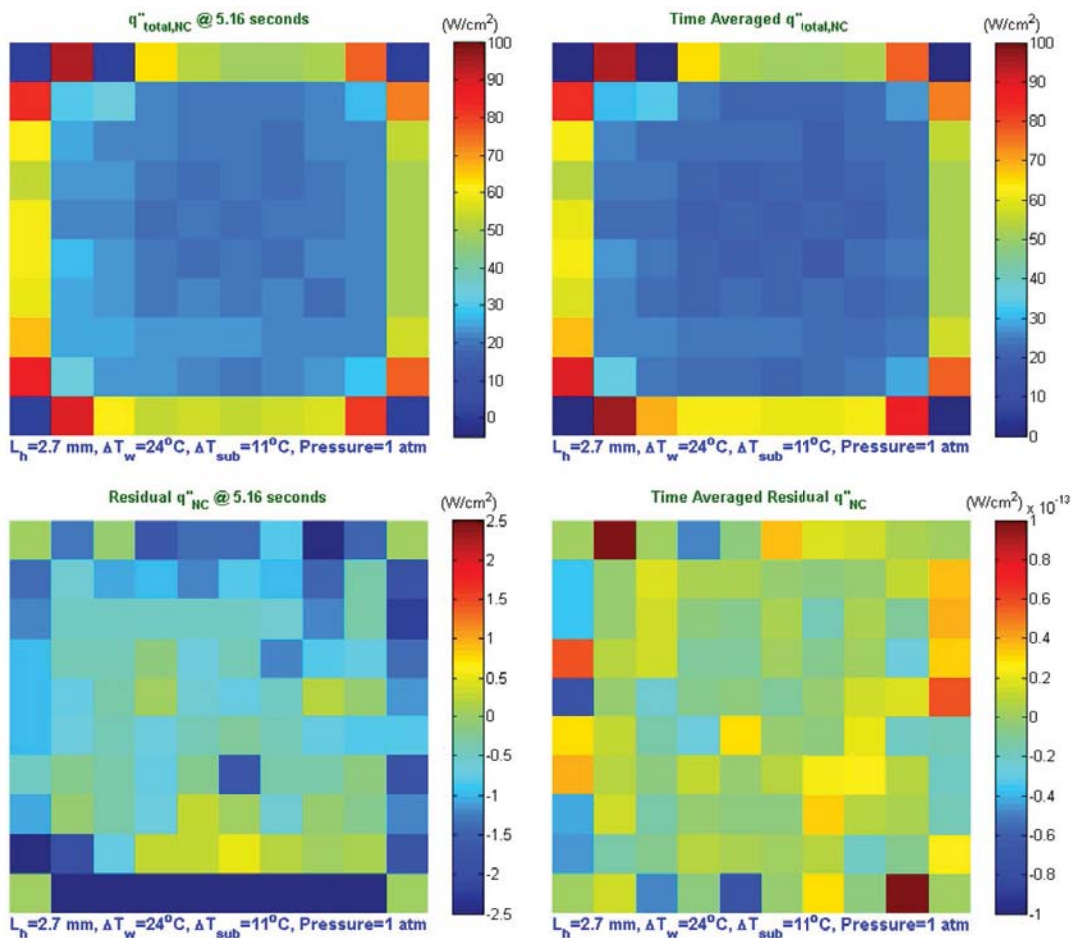


Figure 37.—Natural convection heat flux maps at different stages of data reduction

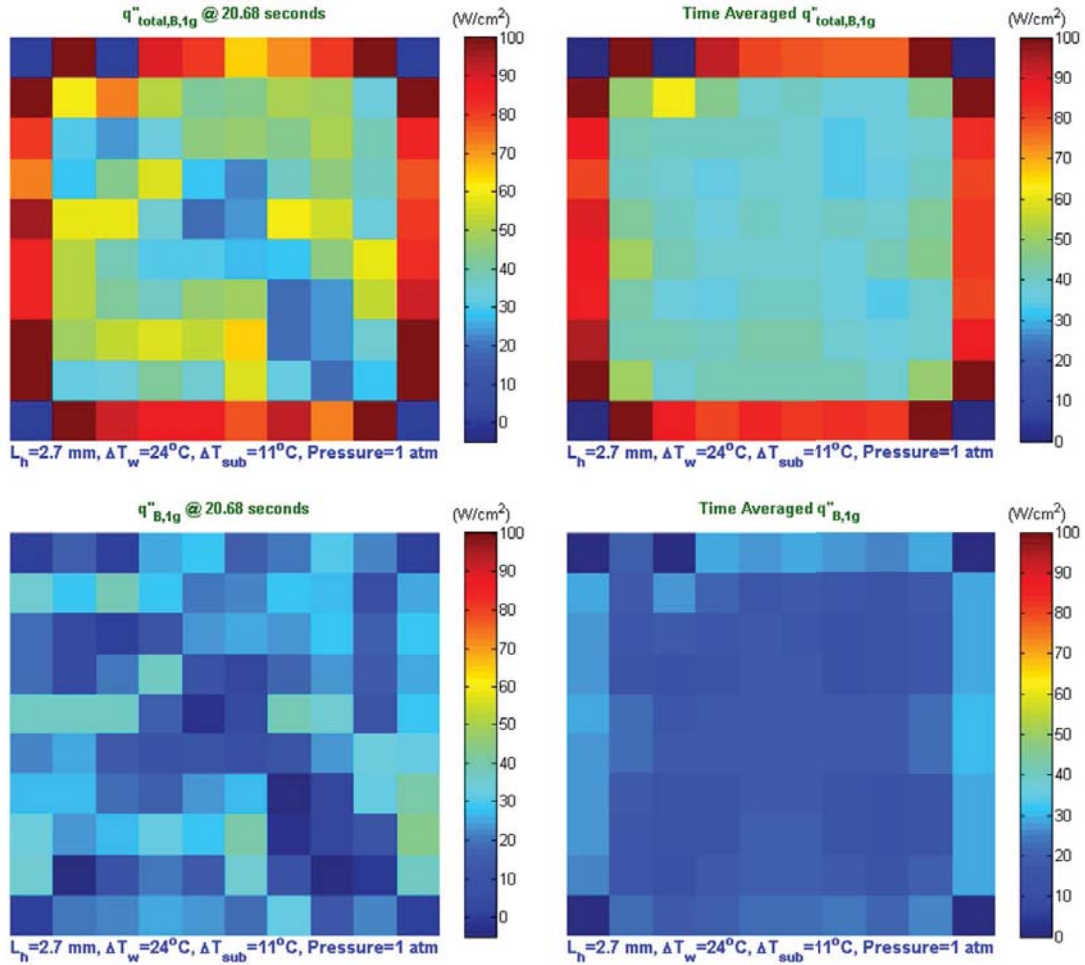


Figure 38.—Boiling heat flux maps at different stages of data reduction

4.4 Uncertainty Analysis

Uncertainty propagation analysis (Ref. 54) was used to calculate the overall uncertainty in the value of measured parameters. For a general case of an experimental result, r , computed from J measured variables $X_{1...J}$, the data reduction equation can be written as:

$$r = r(X_1, X_2, \dots, X_J) \quad (31)$$

The uncertainty in the experimental result is given by

$$U_r^2 = \left(\frac{\partial r}{\partial X_1} \right)^2 U_{X_1}^2 + \left(\frac{\partial r}{\partial X_2} \right)^2 U_{X_2}^2 + \dots + \left(\frac{\partial r}{\partial X_J} \right)^2 U_{X_J}^2 \quad (32)$$

where U_r is the uncertainty in the result, U_{X_1} is the uncertainty in the variable X_1 , etc. The individual uncertainty U_x of the measured variable/parameter was based on the resolution/least-count of the corresponding sensors. For cases where a curve fit/regression approach was adopted for the measurement of certain quantities, the individual uncertainty U_x was based on the standard deviation of the measured parameters from the curve used. The next three sections describe the uncertainty in the value of measured parameters for the different sets of experimental results presented in this work.

Bulk liquid temperature.—Six thermistors (BF1-BF6) were located in the BXF test chamber to record the bulk liquid temperatures. The thermistors were calibrated at the NASA Glenn Research Center Metrology Lab prior to being incorporated into the final assembly. Each thermistor was calibrated over the range of 10 to 70 °C in 10 °C increments against a Standard Platinum Resistance Thermometer (SPRT). The uncertainty in bulk liquid temperature (Figure 39) was only dependent on the sensor uncertainty. For all uncertainty calculations involving a contribution in uncertainty from the bulk liquid temperature, an average of the uncertainties in the six sensors reported on Figure 39 are used.

Pressure.—Three pressure sensors (TC1-TC3) were located in the BXF test chamber to record the chamber pressure. Each of the three sensors were calibrated at the NASA Glenn Research Center Metrology Lab from 0 to 70 psia and at five different temperatures, 22, 30, 40, 55, and 70 °C. At each temperature, three independent pressure cycles were recorded. For all uncertainty calculations involving a contribution in uncertainty from the pressure sensors, an average of the uncertainties in the three sensors reported on Figure 40 were used.

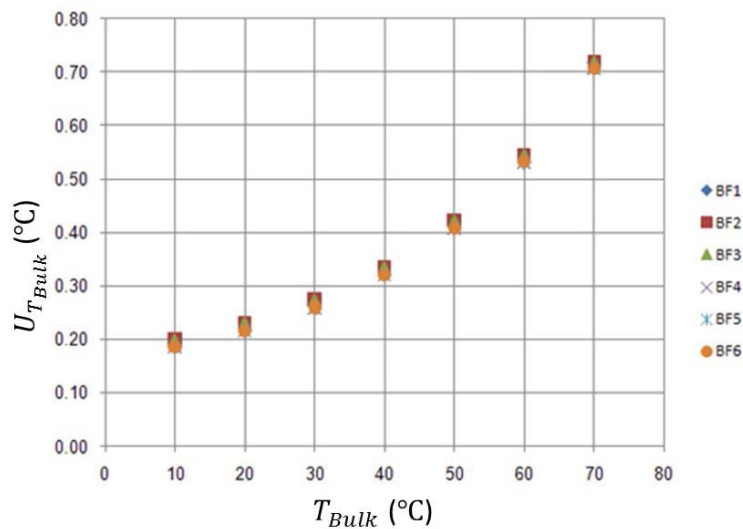


Figure 39.—Bulk fluid thermistor uncertainty results.

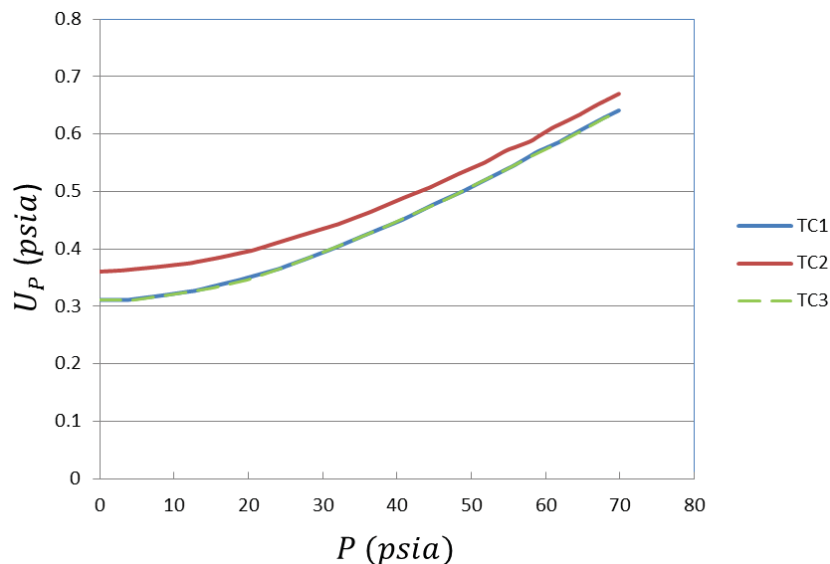


Figure 40.—Pressure uncertainty results.

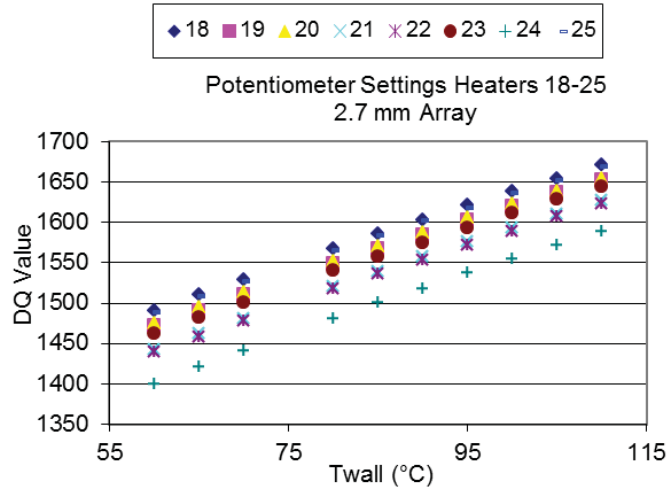


Figure 41.—An example of calibration results for eight microheaters in the 2.7 mm array.

Heater temperature.—The microheater array was operated between 55 and 110 °C. An example of calibration results for eight heaters (Heater nos. 18 to 25 in the 2.7 mm array) is shown on Figure 41. The slope of the DQ versus T_{wall} curve is $\sim 3.71/^\circ\text{C}$, i.e., a temperature resolution of 0.27°C . The uncertainty of 0.5°C associated with the calibration temperature and a temperature resolution of 0.27°C due to the least count of the digital potentiometer used in the feedback circuit could introduce a maximum uncertainty of 0.57°C in the measurement of wall temperature. The uncertainty in the wall temperature for all microheaters in the 7 mm heater array was also within 0.6°C . Hence, a conservative value of 0.6°C for wall temperature uncertainty ($U_{T_{wall}}$) was used for both microheater arrays.

Saturation temperature.—Saturation temperature is a direct function of pressure only. Saturation pressure of n-perfluorohexane (mm Hg) as a function of pressure is given by (Ref. 55):

$$\log(P) = 6.8919 - \frac{1090.52}{214.73 + T_{sat}} \quad (33)$$

Converting from mm Hg to psia yields

$$\log(P) = \log\left(\frac{14.72}{760}\right) + 6.8919 - \frac{1090.52}{214.73 + T_{sat}} \quad (34)$$

Solving for the temperature term

$$T_{sat} = \frac{1090.52}{5.17899 - \log(P)} - 214.73 \quad (35)$$

where pressure is in psia and temperature is in °C. Based on Equation (31) and Equation (35),

$$U_{T_{sat}}^2 = \left(\frac{\partial T_{sat}}{\partial P}\right) U_P^2 \quad (36)$$

The uncertainty in saturation temperature for the different test conditions specified in the test matrix (Table 8) is summarized on Table 9.

Wall superheat.—The wall superheat is defined as the difference between heater temperature and the saturation temperature ($\Delta T_w = T_{\text{wall}} - T_{\text{sat}}$). The uncertainty in heater temperature and the saturation temperature being known, the uncertainty in superheat was calculated using:

$$U_{T_{\text{sat}}}^2 = \left(\frac{\partial T_{\text{sat}}}{\partial P} \right) U_P^2 + U_{T_{\text{wall}}}^2 \quad (37)$$

The uncertainty in wall superheat liquid subcooling for the different test conditions specified in the test matrix (Table 8) is summarized on Table 9.

Subcooling.—The liquid subcooling defined as the difference between saturation temperature and bulk liquid temperature ($\Delta T_{\text{sub}} = T_{\text{sat}} - T_{\text{Bulk}}$). The uncertainty in saturation and bulk liquid temperatures being known, the uncertainty in subcooling was calculated using:

$$U_{T_{\text{sat}}}^2 = \left(\frac{\partial T_{\text{sat}}}{\partial P} \right) U_P^2 + U_{T_{\text{Bulk}}}^2 \quad (38)$$

The uncertainty in liquid subcooling for the different test conditions specified in the test matrix (Table 8) is summarized on Table 9.

Dissolved gas concentration.—While a direct means of measuring the dissolved gas concentration is always preferred, issues with sample withdrawal, maintaining sample integrity, and development of sample standards has prevented these types of measurements. Use of Henry's Law coupled with Dalton's Law is a viable alternative that permits in-situ measurements. The total pressure of any system is equal to summation of the partial pressures of the constituents:

$$P_{\text{total}} = P_{v,\text{NPFH}} + P_g \quad (39)$$

Using the vapor pressure versus temperature data available from NIST Standard Reference Database 85 NIST/TRC Table Database, WinTable, Version 2004, and performing a linear regression on the $\ln(P_{v,\text{NPFH}})$ and $1/T$ data,

$$P_{v,\text{NPFH}} (\text{kPa}) = \exp \left(16.18 - \frac{3841.63}{T + 273.15} \right) \quad (40)$$

TABLE 9.—CONSERVATIVE ESTIMATE OF UNCERTAINTIES IN THE VALUE OF MEASURED PARAMETERS

Test no.	P , psia, atm	T_{Bulk} , °C	U_P , psia	$U_{T_{\text{Bulk}}}$, °C	$U_{T_{\text{wall}}}$, °C	$U_{T_{\text{sat}}}$, °C	$U_{\Delta T_w}$, °C	$U_{\Delta T_{\text{sub}}}$, °C
1, 10	14.7, 1.0	30	0.35	0.27	0.6	0.70	0.92	0.75
2, 11	14.7, 1.0	45	0.35	0.38	0.6	0.70	0.92	0.79
3, 12	14.7, 1.0	55	0.35	0.49	0.6	0.70	0.92	0.86
4, 13	8.5, 0.58	30	0.33	0.27	0.6	1.02	1.20	1.05
5, 14	8.5, 0.58	40	0.33	0.33	0.6	1.02	1.20	1.07
6, 15	23.5, 1.60	45	0.38	0.38	0.6	0.53	0.80	0.65
7, 16	23.5, 1.60	60	0.38	0.54	0.6	0.53	0.80	0.76
8, 17	27.3, 1.86	50	0.39	0.42	0.6	0.48	0.77	0.64
9, 18	20.3, 1.30	40	0.36	0.32	0.6	0.56	0.82	0.65

and hence,

$$P_g = P_{\text{total}} - \exp\left(16.18 - \frac{3841.6}{T + 273.15}\right) \quad (41)$$

Henry's Law states that the concentration of any dissolved gas c_g (ppm) is equivalent to the partial pressure of the gas above it, P_g , or

$$c_g = H_g P_g * 10^{-6} \quad (42)$$

where H_g is the Henry's Law Coefficient which is a function of temperature. Dissolved gas concentration is usually measured at or near room temperature; however, for this analysis it will be assumed that these measurements may be made up to the normal boiling point of about 60 °C. For air in FC-72, H_g has been measured to be 5.4×10^{-5} mole/mole-kPa for $31 \text{ °C} < T_{\text{Bulk}} < 60 \text{ °C}$. This value for Henry's law is assumed to apply to n-perfluorohexane as well. The uncertainty equation for the dissolved gas concentration is

$$U_{c_g}^2 = \left(\frac{\partial c_g}{\partial P}\right) U_P^2 + \left(\frac{\partial c_g}{\partial T}\right) U_{T_{\text{Bulk}}}^2 \quad (43)$$

Using the uncertainty values of total pressure and bulk liquid temperature calculated above (Table 9) along with Equation (42) and Equation (43), the maximum possible uncertainty in the dissolved gas concentration c_g was determined not to be exceed 150 ppm for any of the test runs.

Heat flux.—The uncertainty in total power supplied to the heaters is negligible since the voltage and heater resistance were very accurately measured. Higher uncertainties were associated with the partitioning of total heat into heat used for boiling and heat lost to the backside. The methodology described in Section 4.3 subtracts the backside losses as well as natural convection from the overall heat dissipation. As a result, the boiling heat flux from the heater was underestimated by the amount of heat transferred to the liquid during natural convection regime. The uncertainty in the boiling heat flux is thus the value of natural convection heat flux at that wall temperature and gravity.

$$U_{q'}^2 = U_{q',SUB}^2 \quad (44)$$

The natural convection heat transfer on an upward facing heater was estimated using

$$Nu_L = 0.54 Ra_L^{0.25} \quad (45)$$

where $Nu_L = \frac{hL}{k}$, $Ra_L = \frac{g\beta(T_{\text{wall}} - T_{\text{bulk}})L^3}{\nu\alpha}$ and $L = \frac{L_h}{4}$. The values reported in these tables are based on the run corresponding to the maximum heater temperature for that particular test number. Table 10 and Table 11 summarize the estimation of uncertainty in the boiling heat flux at 1g and $10^{-6}g$.

The uncertainty in the boiling heat flux at the maximum heater temperature for any test number and under Earth gravity conditions are of the order of ~ 1 to 2 W/cm^2 , however, within 10 percent of the actual heat flux. Moreover, the values are much lower at lower wall temperatures. Also, these numbers are reduced significantly upon decreasing the gravity level. The reduction in the gravity level diminished the natural convection heat transfer, the source of uncertainty in the boiling heat flux.

TABLE 10.—CONSERVATIVE ESTIMATE OF UNCERTAINTIES IN HEAT FLUX AT 1g

Test no.	P , psia, atm	T_{Bulk} , °C	L_h , mm	U_{q'',Lh_2} , W/cm ²	L_h , mm	U_{q'',Lh_2} , W/cm ²	L_h , mm	U_{q'',Lh_2} , W/cm ²
1	14.7, 1.0	30	2.7	1.86	2.16	1.97	1.62	2.11
2	14.7, 1.0	45	2.7	1.34	2.16	1.42	1.62	1.52
3	14.7, 1.0	55	2.7	1.01	2.16	1.07	1.62	1.15
4	8.5, 0.58	30	2.7	1.34	2.16	1.42	1.62	1.52
5	8.5, 0.58	40	2.7	1.01	2.16	1.07	1.62	1.15
6	23.5, 1.60	45	2.7	1.86	2.16	1.97	1.62	2.11
7	23.5, 1.60	60	2.7	1.34	2.16	1.42	1.62	1.52
8	27.3, 1.86	50	2.7	1.86	2.16	1.97	1.62	2.11
9	20.3, 1.30	40	2.7	1.86	2.16	1.97	1.62	2.11
10	14.7, 1.0	30	7.0	1.47	5.6	1.55	4.2	1.67
11	14.7, 1.0	45	7.0	1.06	5.6	1.12	4.2	1.2
12	14.7, 1.0	55	7.0	0.8	5.6	0.85	4.2	0.91
13	8.5, 0.58	30	7.0	1.06	5.6	1.12	4.2	1.2
14	8.5, 0.58	40	7.0	0.8	5.6	0.85	4.2	0.91
15	23.5, 1.60	45	7.0	1.47	5.6	1.55	4.2	1.67
16	23.5, 1.60	60	7.0	1.06	5.6	1.12	4.2	1.2
17	27.3, 1.86	50	7.0	1.47	5.6	1.55	4.2	1.67
18	20.3, 1.30	40	7.0	1.47	5.6	1.55	4.2	1.67

TABLE 11.—CONSERVATIVE ESTIMATE OF UNCERTAINTIES IN HEAT FLUX AT 10⁻⁶g

Test no.	P , psia, atm	T_{Bulk} , °C	L_h , mm	U_{q'',Lh_2} , W/cm ²	L_h , mm	U_{q'',Lh_2} , W/cm ²	L_h , mm	U_{q'',Lh_2} , W/cm ²
1	14.7, 1.0	30	2.7	0.1	2.16	0.11	1.62	0.12
2	14.7, 1.0	45	2.7	0.08	2.16	0.08	1.62	0.09
3	14.7, 1.0	55	2.7	0.06	2.16	0.06	1.62	0.06
4	8.5, 0.58	30	2.7	0.08	2.16	0.08	1.62	0.09
5	8.5, 0.58	40	2.7	0.06	2.16	0.06	1.62	0.06
6	23.5, 1.60	45	2.7	0.1	2.16	0.11	1.62	0.12
7	23.5, 1.60	60	2.7	0.08	2.16	0.08	1.62	0.09
8	27.3, 1.86	50	2.7	0.1	2.16	0.11	1.62	0.12
9	20.3, 1.30	40	2.7	0.1	2.16	0.11	1.62	0.12
10	14.7, 1.0	30	7.0	0.08	5.6	0.09	4.2	0.09
11	14.7, 1.0	45	7.0	0.06	5.6	0.06	4.2	0.07
12	14.7, 1.0	55	7.0	0.04	5.6	0.05	4.2	0.05
13	8.5, 0.58	30	7.0	0.06	5.6	0.06	4.2	0.07
14	8.5, 0.58	40	7.0	0.04	5.6	0.05	4.2	0.05
15	23.5, 1.60	45	7.0	0.08	5.6	0.09	4.2	0.09
16	23.5, 1.60	60	7.0	0.06	5.6	0.06	4.2	0.07
17	27.3, 1.86	50	7.0	0.08	5.6	0.09	4.2	0.09
18	20.3, 1.30	40	7.0	0.08	5.6	0.09	4.2	0.09

5.0 Results of the MABE Experiment on the ISS

The data acquired using MABE are described in this section. The model developed using the ground-based data described in Section 2.0 is validated using the MABE data, and modifications to the model are discussed. A demonstration of the wide applicability of this model in predicting low gravity pool boiling data is then given.

BXF was sent to the ISS on the last flight of the Space Shuttle Discovery on February 24, 2011. BXF was installed into MSG, and operations commenced in March 2011. It was planned to obtain MABE data at each of the test conditions given in the test matrix shown in Table 8. However, about three weeks into testing on the ISS and the completion of Tests nos. 10, 11, 13, 14, 15, 17, and 18 (all these tests were with the 7.0 mm heater array), one of the cartridge heaters used to control the bulk fluid temperature failed and shorted to ground, causing a drop in voltage of one of the 24V power supplies. Since this supply also powered the feedback circuits, no regulation of the heater array power was possible and no additional data could be obtained. Measurements of the dissolved gas content also showed an increase from an initial value of less than 150 ppm, perhaps as the fluid deteriorated as the heater burned out, but the data reported here were obtained when the dissolved gas concentration was less than 250 ppm. BXF was shut down after the anomaly occurred, and returned to ground on the last flight of the Space Shuttle Atlantis on July 21, 2011.

The data downloaded during MABE operations were reduced as they were received. The test points the effects of wall superheat, liquid subcooling, pressure, and heater size on boiling heat transfer to be evaluated. CHF was reached for a majority of the test conditions. For each test condition, the heater temperature was increased in 2.5 or 5 °C increments starting from a temperature below the minimum required for onset of boiling to a heater temperature above that required for CHF. Three microheater array configurations corresponding to heater sizes of 7-, 5.6-, and 4.2-mm were tested. The Earth gravity and microgravity pool boiling curves for the tests completed are shown on Figure 42 and Figure 43.

5.1 Onset of Nucleate Boiling

The superheat required for the onset of nucleate boiling (ONB) was found to decrease with increasing pressure, consistent with the observations in literature (Ref. 31). This can be attributed to the nonlinearity in the saturation temperature versus vapor pressure curve for nPFH/FC-72. As a result of this nonlinearity, the differential pressure, and hence the superheat required for the vapor embryos in the cavities to grow and nucleate bubbles, decreases at larger pressures. In microgravity, ONB was often observed to occur at lower superheats when compared to the 1-g values (e.g., Figure 42, $P = 1$ atm, $\Delta T_{sub} = 11$ °C, $L_h = 7.0$ and 5.6 mm). As a result, the heat flux at lower superheats and microgravity conditions were often observed to be larger than the corresponding Earth gravity values, consistent with the observations of other researchers (Ref. 56).

5.2 Effect of Subcooling and Pressure

Heat transfer was observed to increase with subcooling at both Earth and microgravity conditions (Figure 42). As has been discussed in the literature, the effect of subcooling at 1-g was more pronounced at higher superheats near CHF while the nucleate boiling curve mostly remained unaffected (e.g., Figure 42: $P = 0.58$ atm, $\Delta T_{sub} = 26.5$ °C, $L_h = 7.0$ mm, heat flux is 7.3 W/cm² for $\Delta T_{sub} = 1$ °C and 7.5 W/cm² for $\Delta T_{sub} = 11$ °C). However, the degradation in heat flux with decreasing subcooling was significantly higher under microgravity conditions since the jump in heat flux at transition increases with decreasing subcooling, resulting in lower heat transfer at lower gravity levels (Ref. 48). At very low subcoolings ($\Delta T_{sub} = 1$ °C, Figure 42), boiling heat transfer was negligible under microgravity conditions since the bubbles grew to large diameters in order to balance the evaporation at the bubble base and the

entire heater became covered by the vapor. The heat transfer throughout the entire nucleate boiling regime up to CHF was also observed to increase with increasing pressure (Figure 42 and Figure 43) in agreement with the literature (Ref. 31). This can be attributed to an early ONB and increase in the slope of nucleate boiling curve with increasing pressure.

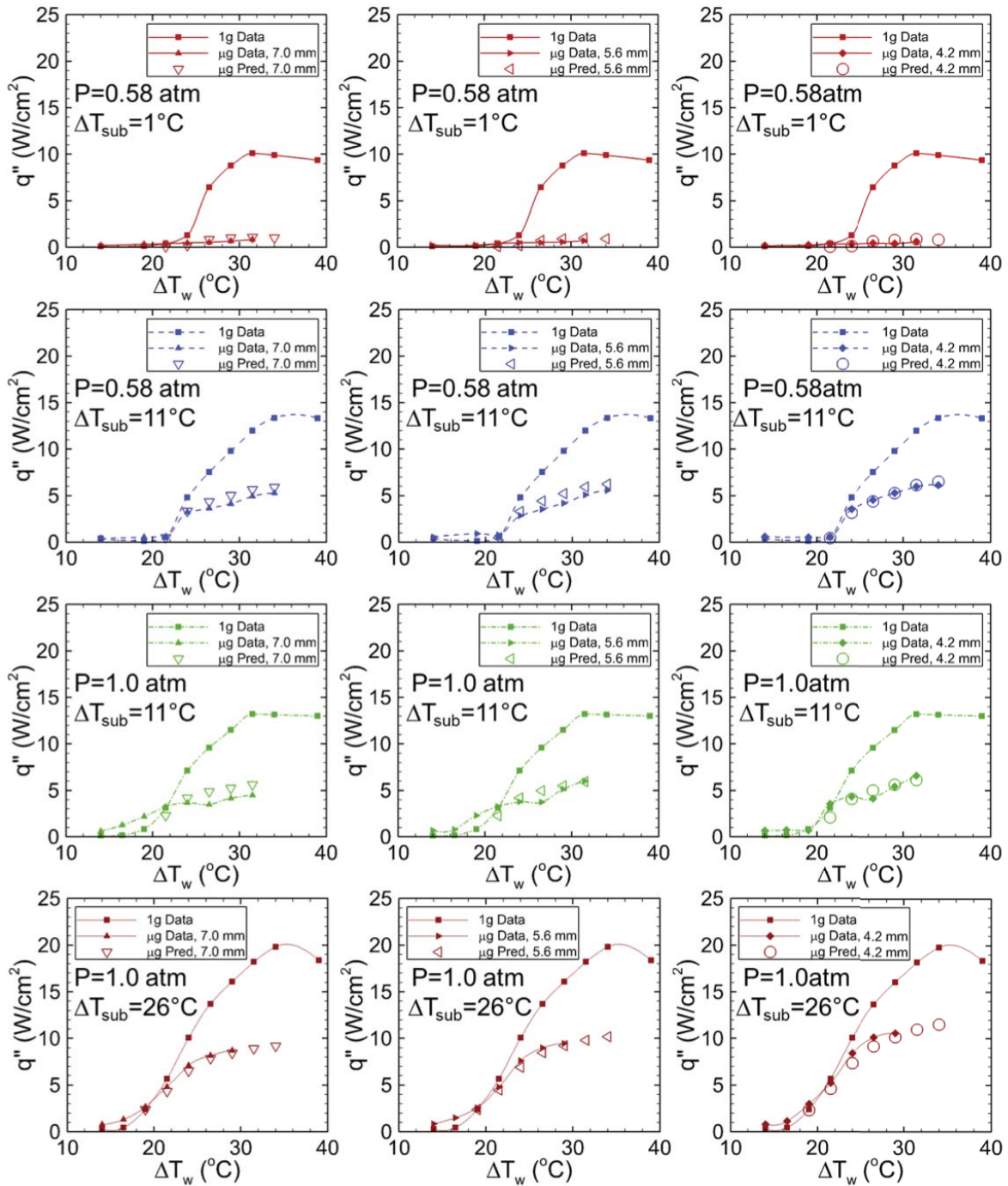


Figure 42.—Experimental Earth gravity and microgravity pool boiling curves along with the microgravity predictions assuming $m_{SDB} = 0$ (Tests nos. 10, 11, 13, and 14 in Table 8).

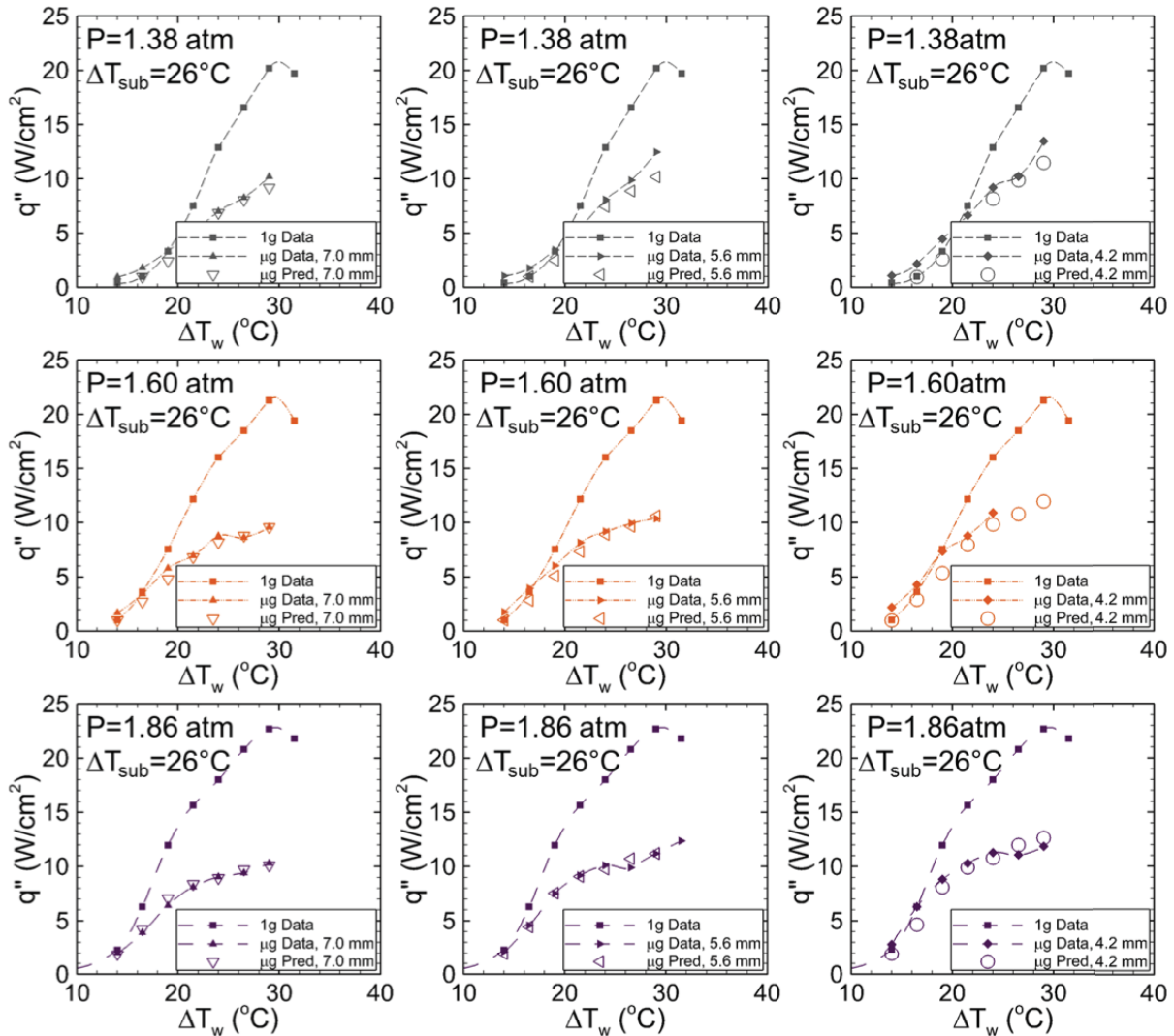


Figure 43.—Experimental Earth gravity and microgravity pool boiling curves along with the microgravity predictions assuming $m_{SDB} = 0$ (Tests nos. 15, 17, and 18 in Table 8).

5.3 Effect of Gravity and Heater Size

The effect of heater size and gravity on nucleate boiling was qualitatively similar to what has been observed in our previous studies (Refs. 43, 44, 48, and 57). Boiling heat transfer was heater size independent in the BDB regime (Earth gravity) while surface tension dominated boiling (SDB regime) was observed in microgravity. As reported previously (Ref. 43), the boiling curve was heater size dependent in the SDB regime. At very high subcoolings (Figure 42 and Figure 43: $\Delta T_{sub} = 26^\circ\text{C}$, $P = 1.0$, 1.38, 1.6, and 1.86 atm), heat flux decreased with increasing heater size under microgravity conditions. However, the trend in heat flux could be reversed at lower subcooling. This behavior where the trend in heat flux with heater size can be reversed with decreasing subcooling has been explained with the help of increasing jump magnitude in heat flux at a_{tran} as discussed in the previous study (Ref. 48).

5.4 Modified Gravity Scaling Parameter

The ability of the gravity scaling parameter developed in the previous work (Eq. (18), (Ref. 48)) to predict the microgravity boiling data obtained on the ISS is shown on Figure 44(a). The Earth gravity

boiling curves obtained prior to launch were used as the reference for all the prediction results. A bias in the experiment versus prediction curve wherein experimentally observed values are higher than the predicted results is clearly apparent. It was stated in the earlier work that the power law coefficient for gravity obtained in the SDB regime ($m_{SDB} = 0.025$) had much scatter and needed to be verified with high quality microgravity experiments. Since the g-jitter in the aircraft data is on the order of 0.01g, the heat transfer measured in the SDB regime is likely to be artificially high as the bubble responds to the fluctuating acceleration. In the true microgravity environment provided by the ISS, the level of g-jitter is much lower and the heat transfer can be lower as well. In fact, we hypothesize that the gravity level may not affect the heat transfer at all in the SDB regime since the shape of the bubble will not change much when the acceleration is lower than a_{tran} . This can be tested by setting $m_{SDB} = 0$ and seeing if this results in better agreement with the data. The excellent agreement between the experimental versus predicted microgravity heat flux values in the nucleate boiling regime when $m_{SDB} = 0$ (Figure 44(b)) tends to support this hypothesis. The prediction results on Figure 42 and Figure 43 calculated using $m_{SDB} = 0$ also agree well with the experiments.

A power law coefficient of $m_{SDB} = 0$ in the SDB regime is physically reasonable. Once in the SDB regime where a nondeparting, coalesced bubble covers the heater, a small change in the gravity level would only change the bubble shape without affecting the steady state value of heat transfer significantly. However, if the gravity levels continuously fluctuate as is the case in parabolic flights where the g-jitter values are relatively large, the resulting continuous adjustments in bubble shape can produce flow around the bubble increasing the heat transfer. In essence, the fluctuation in acceleration (g-jitter) affects heat transfer more than the absolute value of acceleration in the SDB regime. This is one of the most significant findings of the current work performed under space microgravity environments and may address the widely discussed problem of the effect of g-jitter on pool boiling studies (Ref. 36). Based on this agreement, the gravity scaling parameter for pool boiling heat flux can be modified as:

$$q''_{SDB} = q''_{BDB} \left[\frac{a_{tran}}{a_{BDB}} \right]^{m_{BDB}} K_{jump} \quad (46)$$

where a_{tran} , m_{BDB} , and K_{jump} , are given by Equations (10), (13), and (19), respectively.

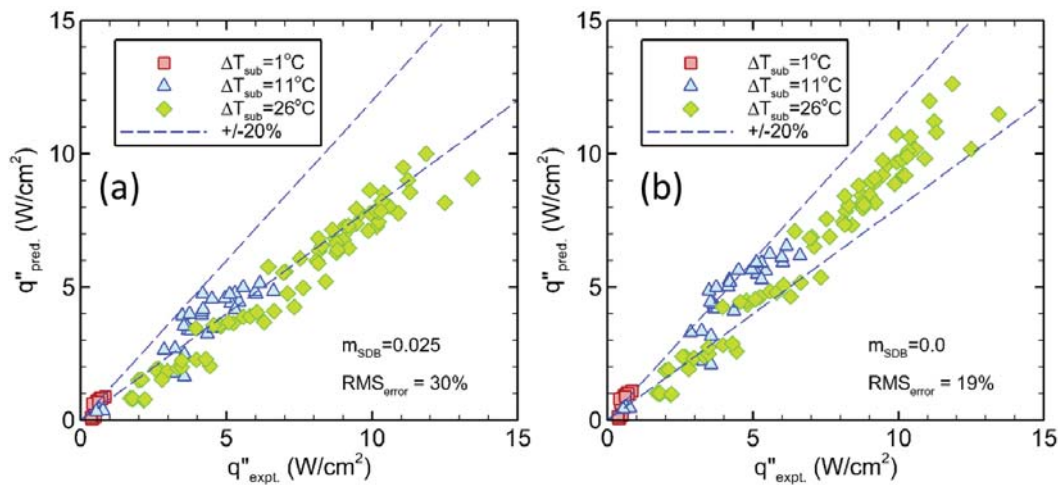


Figure 44.—Comparison of the experimental data and predicted heat flux values in the SDB regime using (a) Equation (18), and (b) Equation (18) with $m_{SDB} = 0$.

5.5 Comparison with Other Microgravity Heat Transfer Data

A theoretical framework for scaling pool boiling heat flux with gravity and heater size has been validated for its robustness over a range of experimental conditions including the high-quality microgravity environment ($<10^{-6}g$) available aboard the International Space Station. This scaling parameter will now be used to explain some of the contradictory trends in the literature.

Merte.—Merte's group (Refs. 56, 58, and 59) studied boiling on flat heaters (19.05- by 38.1-mm²) under the long duration microgravity provided by the space shuttle ($10^{-4}g$). Under these conditions, R' , the ratio of characteristic length (length of the smaller side) to the capillary length, was 0.19 and hence boiling behavior was in the SDB regime. The absence of boiling data for the entire nucleate boiling regime ruled out using the current scaling parameter to predict low-g heat fluxes. Nonetheless, some of the trends in their data agree qualitatively with the current data and can be explained by the current framework. For example, the effect of subcooling was more pronounced under low-g conditions. This was already explained in Section 2.0 and can be attributed to increase in the jump with decreasing subcooling. Similar to the current ISS results, Merte's group also observed early onset of nucleate boiling and heat transfer enhancement in the low heat flux regime at low-g conditions. Boiling heat transfer under low-g conditions was very small at nearly saturated conditions, similar to the observations in the current study.

Dhir.—Dhir (Ref. 60) argued against the usefulness of empirical and mechanism based methodologies in developing comprehensive pool boiling models and presented an alternative in the form of direct numerical simulation of the boiling process. It was argued that the use of empirical correlations is limited by the range of applicability while a complete mechanistic prediction is difficult due to the complex nature of the subprocesses involved, multi-dimensional design space in boiling processes, and lack of supporting data over a wide range of conditions. Four subprocesses (active nucleation site density, thermal response of the heater, bubble dynamics, and heat transfer mechanisms) were identified as being important to the development of a credible predictive model of nucleate boiling. A direct numerical simulation of the boiling process was performed on a micro-fabricated surface (controlled cavities) and a constant temperature heater (thermally decoupled heater) allowing him to focus only on the other two subprocesses (bubble dynamics and heat transfer mechanisms). The results of the simulation in the form of pool boiling curves were then compared with the data of Qui et al. (Ref. 61) where the cavities were also controlled. The good agreement between the experimental values and the numerical predictions at 1g and low-g (Figure 45) was used to stress on the advantages of the numerical models over empirical or semitheoretical models.

Although direct numerical simulation can be a powerful tool for modeling purposes, these techniques for boiling are in their infancy and most of the results are valid for simplified cases such as discussed above. All of these numerical models are heavily dependent on the exact knowledge of the active nucleation site density which usually is unknown in practical applications of interest. As a result, a complete deterministic numerical model for boiling valid across a range of conditions is not possible at this time.

Scaling laws similar to those developed in the current study can be a suitable alternative for some of these applications. The current study has demonstrated that if the boiling curve is known for a given heater at a reference gravity condition, it is possible to scale the heat flux to any other gravity level of interest. Use of the same heater decouples the effect of nucleation site density, improving the accuracy of the prediction. The ability and usefulness of the current framework to accurately scale gravity effects on pool boiling heat flux is highlighted through a few example cases from the boiling literature.

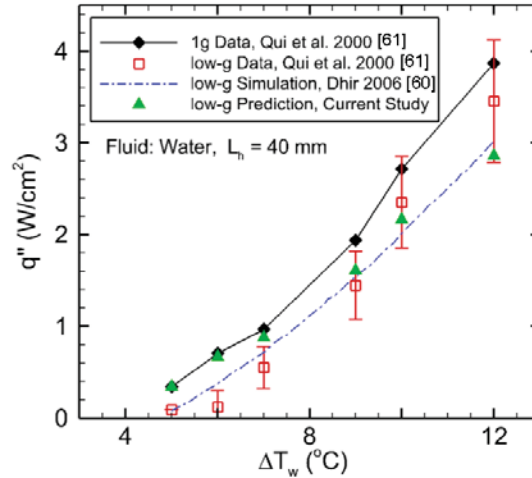


Figure 45.—Comparison of the numerical simulation (Ref. 60) and the current scaling law in predicting microgravity heat transfer of Qui et al. (Ref. 61).

The scaling law is first used to predict the microgravity heat transfer in the saturated boiling experiments of Qui et al. (Ref. 61) (Figure 45). The transition acceleration for boiling of FC-72 on their 40 mm heater can be calculated from Equation (10) to be 0.017g. Since these experiments were performed aboard a parabolic flight where the residual gravity levels are usually of the order of 0.02g to 0.04g, microgravity boiling in these experiments is expected to be in the BDB regime. This is supported by their observations of bubble departure under the low-g conditions aboard the aircraft. As a result, the equation developed for the BDB regime can be used to scale the Earth gravity heat flux to predict the aircraft low-g heat transfer:

The predicted results for the experimental data of Qui et al. (Ref. 61) are shown in Figure 45. The predictions (solid triangles) are mostly within the experimental uncertainty and comparable to the numerical simulations of Dhir (Ref. 60). Both the predictions and simulations may be lower than the experimental data due to the g-jitter as noted in Section 2.0. The power of the scaling law is evident from the fact that no information (e.g., nucleation site density) other than the reference Earth gravity boiling curve was required for the predictions.

$$q''_{\text{low-g}} = q''_{1g} \left(\frac{0.017}{1} \right)^{1+1.6T^*} \quad \text{where } T^* = \frac{T_w - T_{ONB}}{T_{CHF} - T_{ONB}} \quad (47)$$

Oka.—We now discuss the trends in the data of Oka et al. (Refs. 47 and 62) wherein CHF during the parabolic flight (10^{-2} g) boiling experiments were observed to follow the one-fourth power relationship while the CHF during the drop tower (10^{-5} g) experiments were significantly underpredicted using the same relationship. For the first set of experiments (Ref. 47) on the aircraft with 40- by 80-mm² flat heaters, the CHF for CFC-113 and pentane in low-g was reduced to about 40 percent of the Earth gravity values as shown by the open symbols (left pointing triangle and open upward pointing triangle for CFC-113 and pentane, respectively) on Figure 46. A power law coefficient $m = 0.25$ for CHF predicts a 32 percent reduction in CHF (Figure 46, closed left pointing triangle and closed upward pointing triangle at 0.01g for CFC-113 and pentane, respectively) which they argued to be within the experimental uncertainty limits. Considering that the fluctuations in the acceleration were of the same order as the nominal acceleration values during their parabolic flight experiments, better agreement between the data

and the CHF prediction can be expected if g-jitter is taken into account. Taking the smaller side of the heater (40 mm) as the characteristic heater length for the rectangular elements in the parabolic flight experiments, the transition accelerations for CFC-113 and pentane can be calculated from Equation (10) to be 0.003g and 0.007g (Table 12), respectively, so the low-g boiling data obtained during parabolic flight are in the BDB regime (Table 12) and should still be correlated by a power law coefficient $m = 0.25$. Since the boiling in this regime is influenced by the g-jitter (0.035g and 0.02g for CFC-113 and pentane, respectively), including g-jitter in the value of acceleration results in better agreement with the predictions (42 percent for CFC-113—closed left triangle at 0.035g, and 38 percent for pentane—closed delta at 0.02g, Figure 46).

Based on results of their next experiments (Ref. 62) utilizing the drop tower facility ($a/g \sim 10^{-5}$, 30- by 30-mm² heater), Oka doubted the validity of the one-fourth power relationship since the CHF values in these new experiments (Figure 46, closed diamond and inverted triangle for water and CFC-113, respectively) were significantly higher than those predicted by $m = 0.25$ (solid line, 6 percent at $a/g = 10^{-5}$). The current framework, however, indicates that their drop tower ($10^{-5}g$) data were in the SDB regime for both water and CFC-113 (Table 12). Since the one-fourth power relationship is only valid in the BDB regime until transition (0.005g for CFC-113 and 0.04g for water, 30 mm heater, Table 12), the current framework incorporating a jump at transition (Table 12, K_{Jump} is 0.75 for CFC-113 and 1 for water) and $m = 0$ in the SDB regime predicts the drop-tower CHF values for CFC-113 (dashed line) and water (dot-dashed line) very well. The differences between the predictions and experiments may be due to the fact that the value of C used in this example is based on FC-72 data and may not be appropriate for modeling jump when using CFC-113 and water.

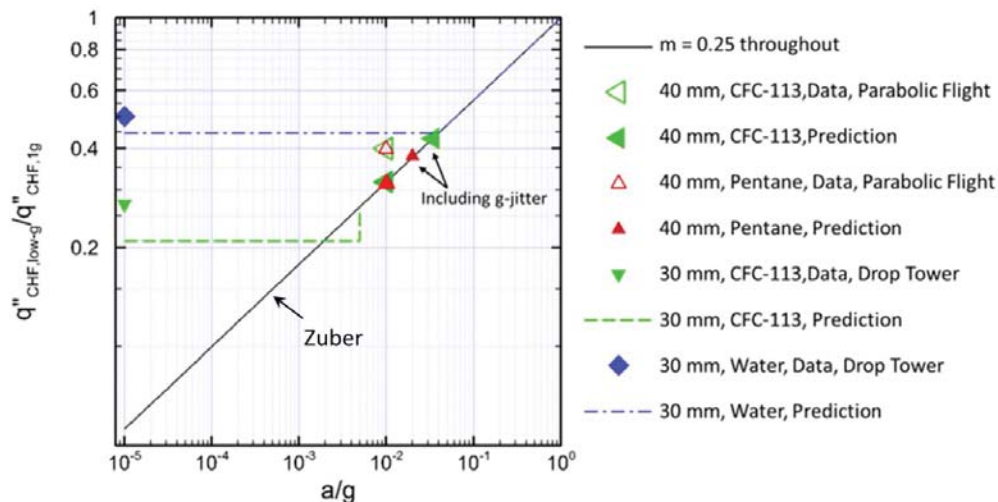


Figure 46.—Normalized CHF versus acceleration for different fluids and microgravity levels (Refs. 47 and 62).

TABLE 12.—THERMO-PHYSICAL PROPERTIES OF CFC-113, PENTANE AND WATER

$L_{h,2}$ mm ²	a_{tran}/g	a/g	Fluid	ρ_l, ρ_v , kg/m ³	σ , N/m	$\Delta T_{sub,0}$ C	$d\sigma/dT$, N/m-K	μ , kg/m-s	k , W/m-K	α , m ² /s	K_{Jump}
40 by 80	0.003	10^{-2} (BDB)	CFC-113	1507, 4.5	0.015	----- N/A – never in the SDB regime -----					
	0.007		Pentane	609, 2.9	0.014	----- N/A – never in the SDB regime -----					
30 by 30	0.005	10^{-5} (SDB)	CFC-113	1507, 7.5	0.015	1	-1.1×10^{-4}	5.0×10^{-4}	0.06	4.3×10^{-8}	0.75
	0.04		Water	958, 0.60	0.059	1	-2×10^{-4}	2.8×10^{-4}	0.66	1.7×10^{-8}	1

Application of scaling parameter to other geometries.—Having explained a few examples for flat surfaces, the scaling model is now applied to additional geometries. CHF predictions for various geometries (Lienhard and Dhir (Ref. 45)) are shown in Figure 47(a). The abscissa is the ratio of the characteristic heater length scale to the capillary length while the ordinate is the ratio of the observed CHF to that predicted by the Zuber correlation (Ref. 14). The presence of two boiling regimes is clearly evident for all the geometries reported. Since the heater length scale is used to vary R' , CHF is independent of the characteristic length scale above a threshold value of R' for each geometry. Below this threshold, CHF increases with decreasing length scale. However, if the length scale is held constant and acceleration is changed to alter the value of R' , CHF would follow a one-fourth power relationship above the threshold R' . Below this threshold, heat transfer would be constant for sphere and would follow a one-eighth power relationship for other geometries. This is now explained in the context of the current framework along with a representative example for boiling of liquid nitrogen on spheres.

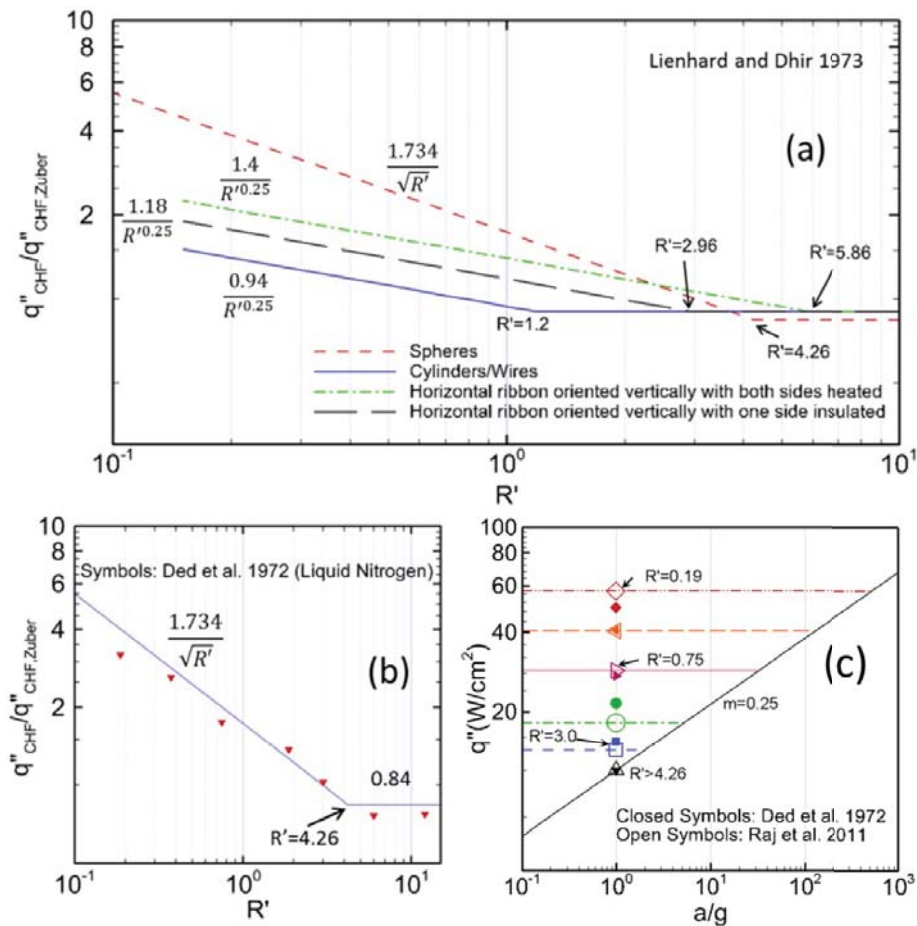


Figure 47.—CHF for finite bodies (a) Lienhard and Dhir (Ref. 45), (b) Ded and Lienhard (Ref. 63), and (c) the current study.

The 1-g CHF data for liquid nitrogen boiling on spheres from Ded et al. (Ref. 63) is shown on Figure 47(b) and Table 13. For the two largest sizes (1.27 cm and 0.635 cm) where the value of R' is above the threshold value of 4.26 for spheres (Table 13), boiling is heater size independent ($\sim 12 \text{ W/cm}^2$) and hence in the BDB regime. These cases are represented by upward pointing triangles and inverted triangles on the $m = 0.25$ line in Figure 47(c) which is a plot of CHF versus normalized acceleration. For all the other sizes, boiling at Earth gravity is heater size dependent and hence surface tension dominated (SDB regime). These cases are represented by other closed symbols on Figure 47(c). Figure 47(b) shows that there is no jump and the slope changes upon transition to the SDB regime. If gravity is changed, a slope of -0.25 on Figure 47(a) or Figure 47(b) in the SDB regime ($R' < 4.26$ for spheres) changes to a slope of 0 on Figure 47(c). A power law coefficient/slope of zero for spheres in the SDB regime is also confirmed by the variable gravity experiments of Steinbichler 2000 (Ref. 64) wherein R113 pool boiling heat transfer on 1.4 mm diameter spheres was similar at 1-g ($R' = 1.8$, SDB regime) and microgravity ($\sim 10^{-2}g$, $R' = 0.18$, SDB regime) for 0 to 30 K subcooling. Using the heater size independent heat flux value of 12 W/cm^2 in the BDB regime as the reference value, the heat flux for other five sizes in the SDB regime (Table 13) can be predicted using Equation (48) with $K_{\text{Jump}} = 1$ for spheres.

$$q''_{SDB, L_{h1}} = q''_{BDB, L_{h2}} \left(\frac{a_{\text{tran},1}}{1g} \right)^{0.25} K_{\text{Jump}} = q''_{BDB, L_{h2}} \left(\frac{2.1L_c}{L_{h1}} \right)^{0.5} \quad (48)$$

where $L_{h1} < 4.26L_c < L_{h2}$.

As an example, for $R = 0.198 \text{ cm}$, $a_{\text{trans}} = 5.2g$ and hence the experiments of Ded et al. (Ref. 63) are in the SDB regime. The heat transfer at 1g is therefore the same as that computed at 5.2g using the one-fourth power relationship. The CHF predictions (open symbols) for other four sizes using the same approach are seen to be very close to the experimentally observed 1-g values (closed symbols) by Ded et al. (Ref. 63) (Figure 47(c)).

This example explains how the normalized CHF data in the literature (Figure 47(a) and (b)) might be converted to a plot of absolute heat flux versus acceleration (Figure 47(c)). The general observation wherein the CHF is reduced in low gravity, but is still higher than predicted by the extrapolation of correlations obtained in Earth gravity has long been a source of confusion in the boiling literature. The current framework wherein the heat transfer follows the one-fourth power law in the BDB regime above a_{trans} explains both the reduction in CHF with gravity, while a constant heat transfer in the SDB regime explains how higher CHF values than that predicted by Zuber's correlation can occur at accelerations below a_{trans} . Similarly, the increase in CHF with decreasing size in the SDB regime can be explained by the increase in a_{trans} leading to departure from the one-fourth power relationship at higher accelerations as shown on Figure 47(c).

Data for the other geometries on Figure 47(a) can also be transformed into a CHF versus acceleration plot (Figure 47(c)) where the corresponding parameters required for scaling pool boiling heat flux are summarized in Table 14. Additional variable gravity pool boiling experiments are, of course, required to verify the values for a_{tran} , and K_{Jump} , dependence of m_{BDB} on T^* , and the value of m_{SDB} for other geometries not validated in this study (cylinders and two ribbon configurations). Particularly for the case of cylinders, the trend in CHF at very low values of R' is not clear (Ref. 25). For example, Zell et al. (Ref. 65) found CHF to be gravity independent ($m_{SDB} = 0$) in their Earth gravity ($0.22 < R' < 0.46$) and low-g ($0.022 < R' < 0.046$ assuming $a/g = 0.01$) pool boiling experiments on a 0.2 mm diameter wire with R12 as the test fluid. Zero slope in the SDB regime cannot be explained either by Lienhard and Dhir (Ref. 45) or by Sun and Lienhard (Ref. 66) who investigated boiling at very small values of R' . Such confusion might be attributable to the large scatter (Ref. 67) in pool boiling data at smaller values of R' and the possibility of multiple subregimes (Ref. 25) within the SDB regime for cylinders. Very clearly, additional experiments with cylinders where R' is varied by changing both the diameter and gravity level is required to understand heat flux variation in the surface tension dominated boiling regime.

TABLE 13.—1g CHF DATA FOR SPHERES (REF. 63)

R , cm	R'	Boiling regime	q_{CHF}'' , W/cm ²	$q_{CHF}''/q_{CHF,Zuber}''$, W/cm ²	a_{tran}/g	$q_{CHF,pred.}''$, W/cm ²
1.3	12.0	BDB	$\sim 12^3$	0.77	520	N/A
0.63	6.0	BDB	$\sim 12^3$	0.77	129	N/A
0.32	3.0	SDB	15	1.03	32	14
0.20	1.87	SDB	22	1.37	5.2	18
0.079	0.75	SDB	27	1.75	2.0	29
0.040	0.38	SDB	41	2.60	0.5	40
0.020	0.19	SDB	50	3.19	0.13	57

TABLE 14.—PARAMETERS FOR SCALING POOL BOILING HEAT FLUX ON DIFFERENT GEOMETRIES

Geometry	Transition criteria	$m_{BDB,CHF}$	m_{SDB}	K_{Jump}
Flat plate facing upward	$R' = 2.1$	0.25	0	Eq. (19)
Spheres	$R' = 4.26$	0.25	0	1
Cylinders	^a $R' = 1.2$	0.25	^a 0.125	^a 1
Horizontal ribbon oriented vertically with both sides heated	^a $R' = 5.86$	0.25	^a 0.125	^a 1
Horizontal ribbon oriented vertically with one side insulated	^a $R' = 2.96$	0.25	^a 0.125	^a 1

^a Verified by changing R , needs to be verified by changing a/g

³ Reference (BDB regime) for scaling predictions at all other sizes in the SDB regime

6.0 Summary and Conclusions

Work performed in preparation for the MABE ISS pool boiling experiment as well as the results from over two hundred pool boiling experiments performed in space environment aboard the International Space Station have been described in this report. The effects of gravity, heater size, superheat, subcooling, and pressure on pool boiling heat transfer were discussed. A recently developed unified framework for scaling pool boiling heat flux with gravity and heater size was presented based the aircraft data, then modified based on the MABE results. The microgravity heat transfer predictions based on the modified scaling law were shown to be in excellent agreement with the experimental data. Finally, many unexplained trends in boiling literature were explained and modeled using the scaling framework and future research directions were proposed. The principal discoveries and conclusions are summarized below.

(1) At least two boiling regimes were found to exist, one dominated by buoyancy (BDB regime) and another dominated by surface tension (SDB regime). The gravity dependence in each of these regimes was different, and the transition from one regime to another could be accompanied by a sharp change in heat flux. Thus, correlations that assume a single power-law dependence of pool boiling on gravity could not be used to account gravity changes when scaling across the regimes.

(2) The boundary between the BDB and SDB regimes depended on both the heater size and gravity level. Heat transfer was *heater size independent* in the BDB regime (“large” heaters” or “high” gravity levels) while the heat transfer was *heater size dependent* in the SDB regime (“small” heater or “low” gravity levels). The nondimensional ratio L_H/L_c (heater length to capillary length ratio) which incorporates the effect of gravity and heater size was found to be a suitable parameter to differentiate between the boiling regimes. Transition between the regimes was observed to occur at $L_H/L_c \sim 2.1$.

(3) The dependence of heat transfer on gravity in the BDB regime was found to be dependent on the wall superheat. A gravity scaling factor based on a nondimensional wall temperature T^* was shown to be able to capture this temperature dependence over a wide range of dissolved gas concentrations, subcoolings, and surface morphologies gravity levels in the BDB regime.

(4) No dependence of heat transfer on gravity was found in the SDB regime due to the dominance of surface tension effects. The scatter in the heat flux data during boiling in the SDB regime was attributed to the g-jitter associated with the microgravity platform on which the experiments were performed.

(5) The magnitude of the jump in heat transfer at the transition between the BDB and SDB regimes depended on the dissolved gas content, heater size, and subcooling. The dependence could be captured as a function of the Marangoni number.

(6) The framework developed to account for gravity scaling could be used to explain some of the discrepancies in the literature regarding gravity effects. It also has the potential to geometries other than flat plates.

References

1. Chiaramonte, F. P., and Joshi, J. A., 2004, "Workshop on Critical Issues in Microgravity Fluids, Transport, and Reaction Processes in Advanced Human Support Technology," Technical report, NASA/TM—2004-212940.
2. Nukiyama, S., 1934, "The Minimum and Maximum Values of Heat Q Transmitted from Metal to Boiling Water Under Atmospheric Pressure," *J. Jap. Soc. Mech. Eng.*, **37**, pp. 367-374.
3. Drew, T. B., and Mueller, C., 1937, "Boiling," *Trans. AIChE*, **33**, p. 449.
4. Lee, H. S., and Merte, Jr. H., 1997, "Pool boiling curve in microgravity," *Journal of Thermophysics and Heat Transfer*, **11**(2), pp. 216-222.
5. Rohsenow, W. M., 1962, "A Method of Correlating Heat Transfer Data for Surface Boiling of Liquids," *ASME Journal of Heat Transfer*, **84**, pp. 969-976.
6. Cooper, M.G., 1984, "Heat flow rates in saturated nucleate pool boiling—a wide-ranging examination using reduced properties," *Advances in Heat Transfer*, Vol. 16, pp. 157-239, Academic Press, Orlando, FL.
7. Stephan, K., and Abdelsalam, M., 1980, "Heat Transfer Correlations for Natural Convection Boiling," *Internal Journal of Heat and Mass Transfer*, **23**, pp. 73-87.
8. Straub, J., 2001, "Boiling Heat Transfer and Bubble Dynamics in Microgravity," *Advances in Heat Transfer*, **35**, pp. 57-172.
9. Kannengieser, O., Colin, C., Bergez, W., and Lacapere, J., 2009, "Nucleate Pool Boiling on a Flat Plate Heater Under Microgravity Conditions: Results of Parabolic Flight, and Development of a Correlation Predicting Heat Flux Variation due to Gravity," *Proceeding of the 7th ECI International Conference on Boiling Heat Transfer*, Florianopolis, Brazil, May 3-7, 2009.
10. Zhang N., Chao D.F., 1999, "Models for enhanced boiling heat transfer by unusual Marangoni effects under microgravity conditions," *Int. Comm. Heat Mass Transfer*, **26**(8), pp. 1081-1090.
11. VDI Heat Atlas, ed. Verein Deutscher Ingenieure, (English version), VDI-Verlag, Dusseldorf, D, 1993.
12. Kutateladze, S. S., 1948, "On the Transition to Film Boiling Under Natural Convection," *Kotloturbostroenie*, No. 3, pp. 10-12.
13. Chang, Y. P., 1957, "A Theoretical Analysis of Heat Transfer in Natural Convection and in Boiling," *ASME Journal of Heat Transfer*, **79**, pp. 1501-1513.
14. Zuber, N., 1959, "Hydrodynamic Aspects of Boiling Heat Transfer," *AEC Rep.*, AECU-4439.
15. Kirishenko, Y. A., and Cherniakov, P. S., 1973, "Determination of the First Critical Thermal Flux on Flat Heaters," *J. Eng. Physics*, **20**, 699-702.
16. Kandilkar, S. G., 2001, "A Theoretical Model to Predict Pool Boiling CHF Incorporating Effects Contact Angle and Orientations," *ASME Journal of Heat Transfer*, **123**, pp. 1071-1079.
17. Siegel, R. and Keshock, E.G., 1964, "Effects of reduced gravity on nucleate boiling bubble dynamics in saturated water," *AICHE Journal*, **10** (4), pp. 509-517.
18. Zell, M., Straub, J., and Weinzierl, A., 1984, "Nucleate pool boiling in subcooled liquid under microgravity results of Texas experimental investigations," *5th European Symp. on Material Science under Microgravity*, Schloss Elmau, pp.327-333.
19. Straub, J., Zell, M., and Vogel, B., 1990, "Pool boiling in a reduced gravity field," *Proc. 9th Int. Heat Transfer Conference*, Jerusalem, Israel, pp. 91-112.
20. Steinbichler, M., Micko, S., and Straub, J., 1998, "Nucleate boiling heat transfer on a small hemispherical heater and a wire under microgravity," *Heat Transfer, Proc. of 11th Int. Heat Transfer Conference*, **2**, Seoul, Korea, pp539-544.
21. Ohta, H., Kawaji, M., Azuma, H., Kawasaki, K., Tamaoki, H., Ohta, K., Takada, T., Okada, S., Yoda, S. and Nakamura, T., 1997, "TR-1A Rocket Experiment on Nucleate Pool Boiling Heat

- Transfer Under Microgravity.” *Heat Transfer in Microgravity Systems*, ASME HDT-Vol.354, pp. 249-256.
22. Lee, H. S., and Merte, H., 1998, “Pool boiling phenomena in microgravity,” *Heat Transfer, Proc. of 11th Int. Heat Transfer Conference*, pp.395-406.
 23. Son, G. and Dhir, V.K., 1998, “Numerical simulation of a single bubble during partial nucleate boiling on a horizontal surface,” *Proceedings of the 11th International Heat Transfer Conference*, Kyongju, Korea, 2, pp. 533-538.
 24. Xu, J.J. and Kawaji, M., 1998, “Study of liquid-solid contact in transition boiling regime under reduced and normal gravity conditions,” *Proceedings of the 11th International Heat Transfer Conference*, Kyongju, Korea, 2, pp. 419-424.
 25. Di Marco, P. and Grassi, W., 1999, “About the Scaling of Critical Heat Flux with Gravity Acceleration in Pool Boiling,” *XVII UIT National Heat Transfer Conference*, Ferrara, June 30-July 2.
 26. Di Marco, P., 2003, “Review of Reduced Gravity Boiling Heat Transfer: European Research,” *Jpn. Soc. Microgravity Appl. J.*, 20(4), pp. 252-263.
 27. Kim, J., 2003, “Review of Reduced Gravity Boiling Heat Transfer: US Research,” *Jpn. Soc. Microgravity Appl. J.*, 20 (4), pp. 264-271.
 28. Ohta, H., 2003, “Review of Reduced Gravity Boiling Heat Transfer: Japanese Research,” *Jpn. Soc. Microgravity Appl. J.*, 20 (4), pp. 272-285.
 29. Pletser, V., Pacros, A., and Minster, O., 2008, “International heat and mass transfer experiments on the 48th ESA parabolic flight campaign of March 2008,” *Microgravity Science and Technology*, 20, pp. 177-182.
 30. You, S. M., Simon, T. W., Bar-Cohen, A., Hong, Y. S., 1995, “Effects of dissolved gas on pool boiling of a highly wetting fluid,” *Journal of Heat Transfer*, 117, pp. 687-692.
 31. Rainey, K. N., You, S. M., and Lee, S., 2003, “Effect of pressure, subcooling, and dissolved gas on pool boiling heat transfer from microporous surfaces in FC-72,” *ASME Journal of Heat Transfer*, 125, pp. 75-83.
 32. Honda, H., Takamastu, H., and Wei, J. J., 2002, “Enhanced boiling of FC-72 on silicon chips with micro-pin-fins and submicron-scale roughness,” *ASME Journal of Heat Transfer*, 124(2). pp. 383-390.
 33. Henry, C. D., Kim, J., and McQuillen, J., 2006, “Dissolved gas effects on thermocapillary convection during subcooled boiling in reduced gravity environments,” *Heat and Mass Transfer*, 42, pp. 919-928.
 34. Raj, R., and Kim, J., 2009, “Thermocapillary convection during subcooled boiling in reduced gravity environments,” *Annals of the New York Academy of Sciences*, 1161, pp. 173-181.
 35. Yaddanapuddi, N., and Kim, J., 2000, “Single bubble heat transfer in saturated pool boiling of FC-72,” *Multiphase Science and Technology*, 12 (3-4), pp. 47-63.
 36. Di Marco, P. and Grassi, W., 2000, “Pool Boiling in Microgravity: Assessed Results and Open Issues,” *Third European Thermal-Sciences Conference*, September 10–13, 2000, ETS, Pisa, Italy.
 37. Lin, L., and Pisano, A., 1991, “Bubble forming on a microline heater,” *Proc. ASME Winter Annual Meeting, Dynamic Systems and Control Division*, 32, pp. 147–163.
 38. Iida, Y., Okuyama, K., and Sakurai, K., 1994, “Boiling nucleation on a very small film heater subjected to extremely rapid heating,” *Int. J. Heat Mass Transfer*, 37, pp. 2771–2780.
 39. Yin, Z., Prosperetti, A., and Kim, J., 2004, “Bubble growth on an impulsively powered microheater,” *Int. J. Heat Mass Transfer*, 47, pp. 1053–1067.
 40. Kim, J., Benton, J. F. and Wisniewski, D., 2002, “Pool boiling heat transfer on small heaters: effect of gravity and subcooling,” *International Journal of Heat and Mass Transfer*, 45 (9), pp. 3921-3934.
 41. Henry, C. D., and Kim, J., 2004, “A study of the effects of heater size, subcooling, and gravity level on pool boiling heat transfer,” *International Journal of Heat and Fluid Flow*, 25, pp. 262-273.
 42. Bakhru, N., and Lienhard, J. H., 1972, “Boiling from small cylinders,” *Int. J. Heat Mass Transfer*, 15, pp. 2011–2025.

43. Raj, R., and Kim, J., "Heater Size and Gravity Based Pool Boiling Regime Map: Transition Criteria between Buoyancy and Surface Tension Dominated Boiling," *ASME Journal of Heat Transfer*, 132(9), pp. 091503-1 – 091503-10.
44. Raj, R., Kim, J., and McQuillen, J., 2009, "Subcooled Pool Boiling in Variable Gravity Environments," *ASME Journal of Heat Transfer*, 131(9), pp. 091502-1 - 091502-10.
45. Lienhard, J. H., Dhir, V. K., 1973, "Hydrodynamic Predictions of Peak Pool-Boiling Heat Fluxes from Finite Bodies," *ASME Journal of Heat Transfer*, 95(2), pp. 152-158.
46. Oka, T., Abe, Y., Tanaka, K., Mori, Y. H., and Nagashima, A., 1992, "Observational Study of Pool Boiling under Microgravity," *JSME Int. J. Series II*, 35, pp. 280-286.
47. Oka, T., Abe, Y., Tanaka, K., Mori, Y. H., and Nagashima, A., 1995, "Pool Boiling of n-Pentane, CFC-113, and Water under Reduced Gravity: Parabolic Flight Experiments with a Transparent Heater," *ASME Journal of Heat Transfer*, 117, pp. 408-417.
48. Raj, R., Kim, J., and McQuillen, J., 2012, "On the Scaling of Pool Boiling Heat Flux with Gravity and Heater Size," *ASME Journal of Heat Transfer*, Vol. 134, 011502-1 to 011502-13.
49. Lee, H. S., 2002, "Mechanisms of Steady-State Nucleate Pool Boiling in Micro-gravity," *Ann. N.Y. Acad. Sci.*, 974, pp. 447–462.
50. Tortelli, V., Tonelli, C., 1993, "Thermal decomposition of branched-chain perfluoroalkanes," *Journal of Fluorine Chemistry*, 60, pp. 165–174.
51. Arnold, W.A., Hartman, T.G., and McQuillen, J., 2007, "Chemical Characterization and Thermal Stressing Studies of Perfluorohexane Fluids for Space-Based Applications," *Journal of Spacecraft and Rockets*, 44, pp. 94–101.
52. Henry, C.D., Kim, J., Chamberlain, B., and Hartman, T.G., 2005, "Heater Size and Heater Aspect Ratio Effects on Subcooled Pool Boiling Heat Transfer in Low-G," *Experimental Thermal and Fluid Science*, Vol. 29, pp. 773-782.
53. Henry, C. D., 2005, "Nucleate Pool Boiling Characteristics from a Horizontal Microheater Array," Doctoral Dissertation, University of Maryland, College Park.
54. Coleman, H. W., and Steele, W., 1999, "Experimentation and Uncertainty for Engineers," Wiley-Interscience, ISBN-10: 0471121460.
55. Dunalp, R. D. and Murphy, C. J. Jr, and Bedford, R. G, 1958, "Some Physical Properties of Perfluoro-n-hexane," *Journal of Chemical Engineering Data*, 80, pp. 83-85.
56. Lee, H. S., Merte, H., Jr., and Chiaramonte, F., 1997, "Pool Boiling Curve in Microgravity," *J. Thermophys. Heat Transfer*, 11(2), pp. 216–222.
57. Raj, R., Kim, J., and McQuillen, J., 2010, "Gravity Scaling Parameter for Pool Boiling Heat Transfer," *J Heat Trans-T ASME*, 132(9), pp. 091502-1 – 091502-9.
58. Lee. H. S., Merte, H. Jr., 1998, "The Origin of the Dynamic Growth of Vapor Bubbles Related to Vapor Explosion," *J Heat Trans- T ASME*, 120(1), pp. 174-182.
59. Lee. H. S., Merte, H. Jr., and Keller, R. B., 1998, "Dryout and Rewetting in the Pool Boiling Experiment Flown on STS-72 (PBE-IIB) and STS-77 (PBE-IIA)," NASA/CR-1998-207410.
60. Dhir, V. K., 2006, "Mechanistic Prediction of Nucleate Boiling Heat Transfer-Achievable or a Hopeless Task," *J HEAT TRANS- T ASME*, 128(1), pp. 1-12.
61. Qui, D. M., Dhir, V. K., Hasan, M. M., and Chao, D., 2000, "Single and Multiple Bubble Dynamics During Nucleate Boiling Under Low-Gravity Conditions," *Proceedings of the National Heat Transfer Conference*, Begel House, NY, pp. 62-71.
62. Oka, T., Abe, Y., Tanaka, K., Mori, Y. H., and Nagashima, A., 1996, "Pool Boiling Heat Transfer in Microgravity," *JSME International Journal*, 39(4), pp. 798-807.
63. Ded, J. S., and Lienhard, J. H., 1972, "The Peak Pool Boiling Heat Flux from Spheres," *AICHE Journal*, 18(2), pp. 337-342.
64. Steinbichler, M., 2000, "Experimentelle Untersuchung des gesättigten undunterkühlten Siedens an Miniaturheizflächen unter Mikrogravitation," Doctoral Dissertation, Technical University Muenchen, Muenchen.

65. Zell, M., Straub, J., and Vogel, B., 1989, "Pool Boiling Under Microgravity," *J. Physico-Hydrodynamics*, 11, pp. 812-823.
66. Sun, K. H., and Lienhard, J. H., 1970, "The Peak pool Boiling Heat Flux on Horizontal Cylinders," *Int. J. Heat Mass Transfer*, 13, pp. 1425-1439.
67. Bakhru, N., and Lienhard, J. H., 1972, "Boiling from Small Cylinders," *Int. J. Heat Mas Transfer*, 15, pp. 2011-2025.

